Fluid Inclusions as an Exploration Tool in the Yellowknife Gold Belt, Northwest Territories, Canada

by

Baykan Aksu

A thesis submitted in partial fulfillment of the requirements for the degree of

Master of Science

Department of Earth and Atmospheric Sciences
University of Alberta

ABSTRACT

The Archean Yellowknife greenstone belt hosts world-class orogenic gold deposits including Con and Giant along with active prospects extending several tens of kilometers along the belt. Some common challenges in exploration for orogenic gold deposit include the nugget effect, which can lead to assays not being representative of the gold grade in the samples analyzed. In contrast, fluid inclusions are homogeneously distributed throughout veins such that, if fluids that correlate systematically with gold can be identified, fluid inclusion characterization would effectively distinguish mineralized from barren samples. In this thesis, we evaluate whether a chemical signature of the fluid inclusions can be used to discriminate between auriferous and non-auriferous samples in different geological backgrounds. Crushing stage tests provide a fast and reliable first order estimate on whether high-pressure of volatiles is common in fluid inclusions within a given sample. We have performed crushing analyses in samples from underexplored claims as well as in mineralized samples from the historic mining sites. The majority of the gold-bearing quartz veins from the Quyta-Bell property have been identified by their high-pressure volatile contents. In the Giant gold mine, our results show that high-pressure volatiles can be used as a proxy to the gold-rich zones within 5 meters.

The presence/absence of high-pressure volatiles as evaluated through crushing tests correlates with dominance of specific fluid inclusion types. Type I aqueous inclusions are abundant in the barren samples. The main component of these inclusions is relatively low-pressure H_2O and CO_2 below the limit of detection. Type II carbonic (CO_2 ± CH_4) inclusions correlate with gold-bearing samples. Mineralizing fluids at both the Quyta-Bell property and the Giant mine are

CO_2-CH_4 rich and H_2O poor to absent (below detection). Application of crushing stage on the field can easily recognize these volatiles and help narrow potential auriferous veins.

In addition to CO_2 and CH_4, gold-bearing samples from the Quyta-Bell property are characterized by the presence of graphite. Graphite was observed as a solid opaque phase hosted in fluid inclusions and as a hydrothermal product overgrowing and forming in veins with iron sulfides. Graphite overgrowing and in veins crosscutting pyrrhotite indicates that graphite postdates sulfide precipitation. The temperatures calculated from the graphite thermometer vary between 400 to 480 °C for the graphite inclusions and 530 to 610 °C for the graphite in veins. The cooler temperature recorded in the inclusions is probably an artifact of post-entrapment graphite precipitation within the inclusion at lower temperatures as the closed system cooled down. The higher temperatures indicate lower amphibolite facies and are in agreement with the peak metamorphism in the area. The systematic correlation between gold and graphite occurrences in the Quyta-Bell property suggest a genetic relationship between them. Gold precipitation is most likely associated with high-temperature fluids trapped during peak metamorphism. Some possible precipitation mechanisms for graphite include mixing different C-bearing fluids and the reduction of hydrothermal fluid. These mechanisms can be geochemically linked to gold precipitation. Both high-pressure volatiles and graphite in these quartz veins could be used as a vector for gold occurrences in the Quyta-Bell property.

ACKNOWLEDGEMENTS

The successful completion of this thesis belongs to many people whose contributions are priceless. First and foremost, I am grateful to my supervisor Prof. Pilar Lecumberri-Sanchez for she was the one who invited me to study in Canada and guide me through this great experience. I also would like to express my gratitude to Prof. Matthew Steele-MacInnis for his valuable contributions and his support during lab work.

I would like to thank my beautiful country for trusting and funding me through my study. I hope one day I can repay this generosity. I have great pleasure in acknowledging my gratitude to all of my colleagues at the University of Alberta. My very special thanks go to Ph.D. (c) Sarah Elizabeth McAdam Milne for being a great friend and a roommate that listened through all of my presentations. The project would not have been possible without the support of colleagues at the Gold Terra Resource Corp. I am grateful for the hospitality and contributions of Hendrik Falck.

I dedicate this work to my parents and all of my friends for their unconditional support. Especially, I thank my mother with all my heart. Without her endless support, patience, and love this work would not be possible.

TABLE OF CONTENTS

CHAPTER 1

CHAPTER 2

CHAPTER 3

CHAPTER 4

CHAPTER 5

LIST OF TABLES

LIST OF FIGURES

CHAPTER 1

INTRODUCTION

Orogenic gold deposits have provided the majority of the mined gold worldwide and become the largest single deposit class (Phillips, 2013; Gaboury, 2019). These deposits were formed in metamorphosed terranes preferentially distributed in Archean-Early Proterozoic greenstone belts and Phanerozoic slate belts (Goldfarb et al., 2001). Characteristically gold is associated with sulfides hosted in structurally controlled quartz and carbonate lodes. Usually, there is a variety in the host rock lithologies but often they are metamorphosed to greenschist-amphibolite grade (Groves et al., 1998). Although it is still debated, the source of fluids and metals are considered to be the devolatilized crustal rocks during orogenic activity (Goldfarb and Groves, 2015). These fluids are often classified as low salinity, H_2O-CO_2 with minor CH_4 and N_2 (Ridley and Diamond, 2000; Bodnar et al., 2013). Gold precipitation in these systems has been generally attributed to wallrock sulfidation by Fe-rich lithologies and fluid immiscibility (Phillips and Powell, 2010). Current exploration targets are major fault zones and iron-rich host rocks.

The Yellowknife greenstone belt, located in the Northwest Territories, Canada, is an Archean tectonic province that hosts numerous gold occurrences including the world-class Giant and Con orogenic gold deposits. Gold mineralization is hosted in diverse lithologies within the belt including massive and pillowed basalts, turbiditic sequences, and magmatic intrusions (van Hees et al., 1999; van Hees et al., 2006a; Ootes et al., 2006; Siddorn et al., 2006). The style of mineralization is distinct between deposits with gold occurring as free gold or hosted in sulfides, disseminated or focused in veins, and associated with diverse alteration styles (Shelton et al., 2004). The diversity in mineralization styles and host rock lithologies has presented a major challenge in exploration. Previous fluid inclusion studies in the area have indicated the likely depositional mechanisms in the Yellowknife greenstone belt. This thesis aims to expand that understanding and evaluate whether a chemical signature of the fluid inclusions can be used to discriminate between auriferous and non-auriferous samples in different geological backgrounds. The Yellowknife greenstone belt is the ideal location for this type of analysis due to its historic validation as a large gold district as well as the new potential shown by recently expanded claims.

The main body of the thesis is arranged in two studies (chapters 3 & 4). Each study has its introduction, methods, results, discussions, and conclusion section. The first study evaluates the application of the crushing stage test and fluid inclusion analysis as an exploration method for orogenic gold deposits. This study was performed on the Giant mine and the Quyta-Bell property. The second study focuses on the spatial relation between gold and graphite observed in the Quyta-Bell property. We discussed possible depositional mechanisms for gold and whether we can use graphite as a proximity indicator for mineralization.

CHAPTER 2

REGIONAL GEOLOGY

The Archean Slave Craton, in the Northwest Territories and Nunavut, forms the northwestern part of the Canadian Shield. The Craton consists of an old Mesoarchean gneissic basement complex and a younger Neoarchean supracrustal rock assemblage referred to as the Yellowknife Supergroup (Henderson, 1970). The Yellowknife Supergroup formed during distinct tectonic stages. Rifting and mafic volcanism between 2.73 and 2.70 Ga formed the greenstone belt and followed by arc-like volcanism between 2.69 and 2.67 Ga (Isachsen et al., 1991; van Breemen et al., 1992; Pehrsson and Villeneuve, 1999; Cousens, 2000; Cousens et al., 2006; Bleeker and Hall, 2007; Ootes et al., 2011). Erosion of dominantly older volcanic rocks and minor Mesoarchean gneissic basement formed the 2.66 Ga greywacke-mudstone turbidites (Yamashita and Creaser, 1999; Ferguson et al., 2005; Ootes et al., 2009). Arc plutonism and volcanism at 2.63 Ga led to the second package of turbidite deposition in a back-arc basin setting (Davis et al., 2003; Ootes et al., 2009; Ootes et al., 2011).

The Yellowknife greenstone belt is the southwesternmost of several Archean greenstone belts in the Slave Craton. This approximately N-S stretching belt is confined in the west by the Western Plutonic Complex, which is a part of the Defeat Plutonic Suite, and metasedimentary rocks in the east (Fig. 1). The Yellowknife greenstone belt mostly consists of mafic tholeiitic volcanic rocks of the 2.73-2.70 Ga Kam Group and overlying calc-alkaline volcanic rocks of the 2.69-2.66 Ga Banting Group (Helmstaedt and Padgham, 1986; Isachsen et al., 1991; Isachsen and Bowring, 1997; Cousens et al., 2002). The 2.67-2.65 Ga Duncan Lake Group, consists of the sedimentary rocks of the Yellowknife Supergroup covering the older volcanic sequences (Henderson, 1970; Helmstaedt and Padgham, 1986). The Duncan Lake Group is further divided into Walsh, Burwash, and Jackson Lake formations (Davis and Bleeker, 1999; Thompson, 2006). Thick sequences of graphitic mudstone-sandstone turbidites of Walsh Formation and greywacke-mudstone turbidites of Burwash Formation are mostly derived from the weathering of the volcanic rocks of Kam and Banting Groups (Helmstaedt and Padgham, 1986; Ootes et al., 2009). The Yellowknife Supergroup has undergone long-lasting regional metamorphism and short periods of local contact metamorphisms mainly resulting from the intrusions of the Defeat Plutonic Suite and Prosperous plutons (Helmstaedt and Padgham, 1986; Davis and Bleeker, 1999; Thompson, 2006). Regional deformation occurred in two phases (Davis and Bleeker, 1999; Ootes et al., 2011). Stage 1 deformation triggered by accretion and collisions led to pre-peak, low grade, greenschist facies, regional type metamorphism (Davis and Bleeker, 1999; Thompson, 2006). Emplacement of the calc-alkaline Defeat Plutonic Suite, located to the west of the Yellowknife greenstone belt, occurred between 2.63 to 2.62 Ga and predate stage 1 deformation (Davis and Bleeker, 1999; Thompson, 2006). Among the turbiditic deposits of the Burwash Formation, high-grade amphibolite facies contact metamorphism was assumed to be associated with the Defeat Plutonic Suite and S-type plutons including the 2592 Ma Prosperous plutons (Davis and Bleeker, 1999; van Hees et al., 2006a; Thompson, 2006; Ootes et al., 2011). Ongoing convergence in the Yellowknife Domain resulted in crustal thickening followed by melting and emplacement of S-type late synorogenic granitoids between 2.6 to 2.58 Ga (Davis and Bleeker, 1999; Ootes et al., 2011). A major plutonic event in the Slave Craton referred to as “granite bloom” is concurrent with the second stage of peak regional deformation and metamorphism (Davis and Bleeker, 1999; Ootes et al., 2011).

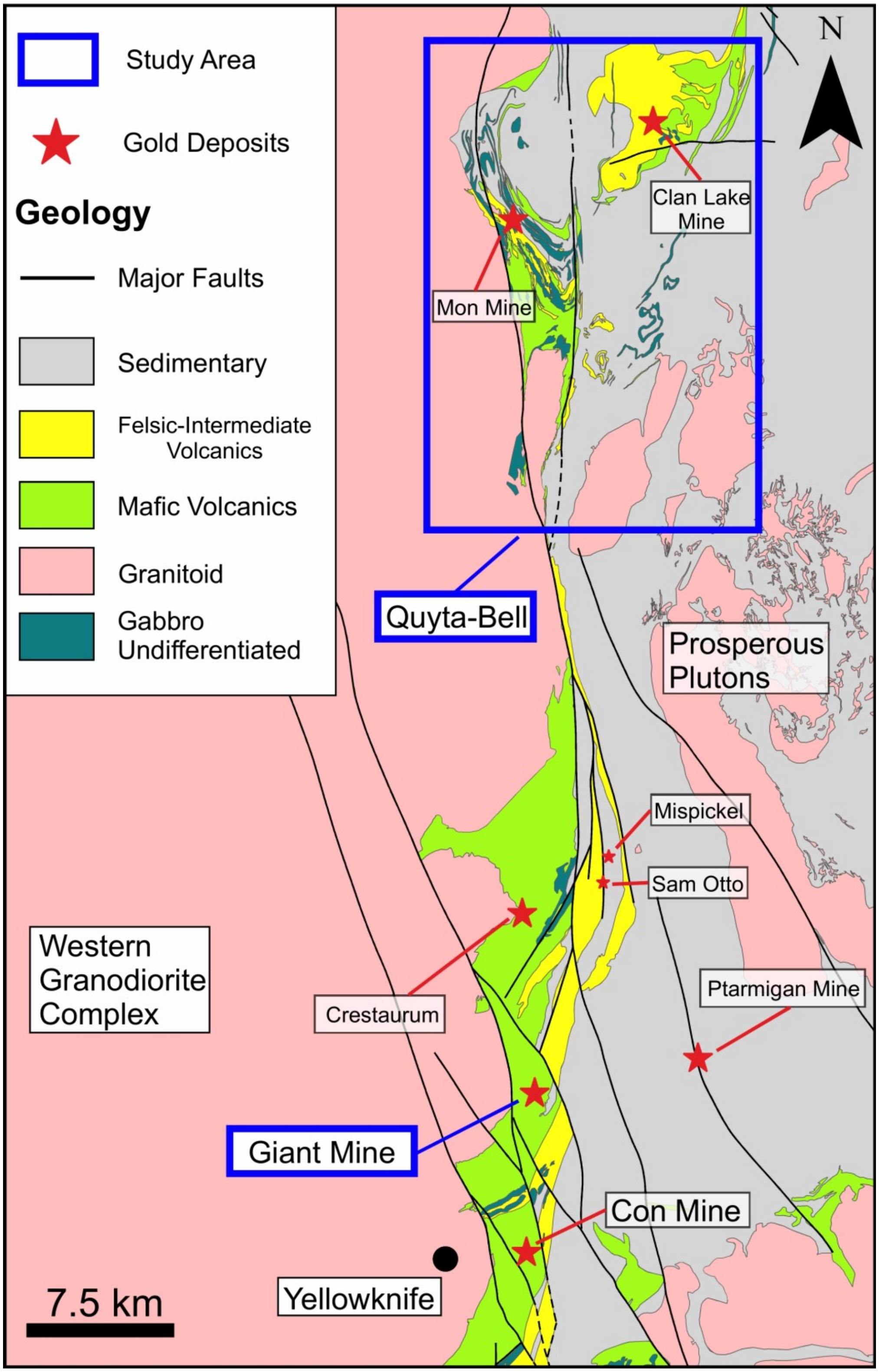

Figure 1. Simplified geological map of the Yellowknife greenstone belt, showing the location of gold prospects, past-producing mines, and study area (Modified after Stubley and Irwin, 2019). NAD 83 UTM:11N

Gold mineralization in the Yellowknife greenstone belt is mainly shear-hosted quartz-carbonate lode deposits and shares very similar characteristics to other orogenic gold deposits (Siddorn et al., 2006; Ootes et al., 2011). The absolute timing of the mineralization was documented as 2591 ± 37 Ma from the Re-Os geochronometer (Ootes et al., 2011). This age is concurrent with stage 2 deformation and "granite bloom" representing peak metamorphic and magmatic conditions in the Yellowknife greenstone belt (Davis and Bleeker, 1999; Ootes et al., 2011). The Prosperous Granite located to the east of the belt with crystallization ages of 2596 Ma was formed as a result of this final Archean plutonism (Davis and Bleeker, 1999). This high-temperature metamorphism formed the auriferous hydrothermal fluids that eventually lead to the mineralization (van Hees et al., 2006a; Ootes et al., 2011). Gold occurrences in the belt have been documented in most of the lithologies including massive and pillowed basalts of the Kam Group (i.e., Con, Giant, and Crestaurum) and turbiditic sequences of Walsh and Burwash Formations (i.e., Ptarmigan, Discovery, Mispickel) (van Hees et al., 1999; Hauser et al., 2006; van Hees et al., 2006a; Ootes et al., 2006). Elevated levels of gold and molybdenite had been also recognized in the 2671 Ma Ryan Lake pluton located 15 km north of Yellowknife (Ootes et al., 2006; Ootes et al., 2007). This suggests gold and other precious metals were introduced to the belt before the associated orogeny and metamorphism. Additionally, 2658 – 2678 Ma quartz-feldspar porphyry dikes, possibly radiating from the Ryan Lake pluton, contain >1 ppm gold (Boyle, 1961; Isachsen et al., 1991). These earlier intrusions have been suggested to play a crucial part in fertilizing the belt with metals and induce a favorable setting for orogenic gold mineralization (Ootes et al., 2007).

Giant Mine

Giant gold mine is a world-class gold deposit and the largest producer in the Slave Craton. Two styles of mineralization and associated deposition have been recognized: (1) Dominant refractory gold, deposited as wallrock hosted ore by the interaction between Ti-rich wallrock and the mineralizing fluid; (2) Lesser visible gold, hosted in quartz-carbonate veins deposited by H_2S loss into vapor phase triggered by fluid unmixing (van Hees et al., 1999; Shelton et al., 2004; Canam, 2006). Ore zones in the Giant mine primarily consist of bands of quartz and sulfide within sericite-carbonate to chlorite-carbonate altered schist and the largest refractory ore bodies are generally associated with strong sericite alteration (Coleman, 1957). Sulfide minerals typically found in the ore zones are pyrite, arsenopyrite, sphalerite, chalcopyrite, stibnite, and pyrrhotite with arsenopyrite and pyrite being closely associated with gold (Coleman, 1957; Shelton et al., 2004). The majority of gold mineralization in the mine is in refractory form and hosted within the Ti-rich metabasalts of the Kam Group Formation (van Hees et al., 1999; Shelton et al., 2004; Canam, 2006). It has been suggested that hydrothermal alteration of the ilmenite in the metabasalts liberated Fe^{2+} which in return reacted with the ore-bearing fluid and form sulfide-hosted refractory gold (van Hees et al., 1999). Two distinct types of fluid related to the gold mineralization have been reported in the Giant mine (Shelton et al., 2004): (1) CO_2-rich inclusions mostly found in gold-bearing quartz veins; and (2) H_2O-CO_2 inclusions that are rarely observed with visible gold mineralization. Leakage, a type of post-entrapment modification, and unmixing of an H_2O-CO_2-NaCl parent fluid have been argued to be the origin of the almost carbonic fluids (Shelton et al., 2004). Based on lithogeochemical and isotopic evidence from the Giant mine, the metasedimentary rocks bordering the deposit to the east are a possible source for the metals and fluids (van Hees et al., 1999; van Hees et al., 2006b). An east-dipping alteration zone acted as a pathway for the ore-bearing fluids. Fluids derived from the metasedimentary rocks removed As and Sb from the surrounding rocks and caused the high concentration of these minerals in the refractory ores of the Giant mine (van Hees et al., 1999; van Hees et al., 2006b).

Quyta-Bell Property

Compared to the Giant mine this area is under-explored and gold production was limited to approximately 100 kg in the nearby MON and Clan Lake mines (Fig. 1) (Silke, 2009). Style of mineralization is visible gold hosted in quartz veins and sulfidized wall rocks (Hansen, 2013). Gold occurrences in the Clan Lake area are known to be hosted in intermediate-felsic host rocks (Hansen, 2013). This area is characterized by intense alteration (sulfidation, sericitization, and silicification) and metamorphic grade reached lower amphibolite grade (Pratico, 2009; Hansen, 2013). Unlike mineralization styles in the Giant mine, gold is often associated with pyrrhotite (less frequently chalcopyrite, galena, sphalerite) (Hansen, 2013). An early pre-gold generation of pyrrhotite and arsenopyrite was also reported (Hansen, 2013). Precipitation of gold was achieved by liberation of Fe^{+2} from the hydrothermal alteration of ilmenite ($FeTiO_3$) to titanite ($CaTiSiO_5$) followed by the formation of pyrrhotite with sulfidation of the liberated iron (Hansen, 2013).

CHAPTER 3

APPLICATION OF FLUID INCLUSION CRUSHING TEST AS A POTENTIAL EXPLORATION METHOD FOR OROGENIC GOLD DEPOSITS

3.1 Introduction

Approximately 14 million ounces of gold have been historically produced in the Yellowknife greenstone belt (Bullen and Robb, 2006). The extent of the gold camps and the magnitude of the resources has kept increasing over the years with ongoing exploration stretching tens of kilometers north and south of the historic mining sites (Armitage, 2019). One of the major challenges of exploration in the Yellowknife greenstone belt is the gold nugget effect. This sampling error can cause mineralization to go undetected or overestimated, especially within lode-gold deposits (Dominy et al., 2001). Indirect vectors such as systematic changes in mineral chemistry or the presence of alteration haloes provide valuable assets in the field because they are more homogeneously distributed and therefore unaffected by the nugget effect. While geochemical vectors provide valuable indirect proxies, they can be strongly affected by lithologic diversity (Bove et al., 2007). Mineralization in the Yellowknife greenstone belt is highly diverse in terms of host lithologies, deposition textures with associated alteration assemblages, and gold occurrence either as native gold in veins or hosted in disseminated sulfides (Shelton et al., 2004). In contrast, if a single type of fluid is responsible for mineralization in all lithologies or if fluid-fluid processes (such as boiling) are responsible for mineralization, the properties of fluid inclusions in mineralized samples should be comparable and distinct from samples that have not interacted with the mineralizing fluid. This chapter evaluates the value of fluid inclusion tests as geochemical vectors in two main claims within the Yellowknife greenstone belt.

Physicochemical properties of ore-related fluid inclusions are diagnostic of deposit types based on the presence/absence of specific fluid inclusion types (Bodnar et al., 2013; Lecumberri-Sanchez et al., 2021). Fluids in hydrothermal deposits related to metamorphism (including orogenic type gold deposits) are typically volatile-rich with components including CO_2, CH_4, and N_2 (Ridley and Diamond, 2000; Bodnar et al., 2013). The presence of volatile-rich inclusions can therefore be used to distinguish orogenic gold deposits from other gold mineralization styles (Lecumberri-Sanchez et al., 2021). Furthermore, prior studies have suggested that volatile-rich fluids are commonly spatially related to mineralization in orogenic gold deposits (Diamond and Marshall, 1990), while fluids in distal and non-mineralized samples are typically volatile-poor. Volatile-rich inclusions are therefore a potential indicator of gold fertility. In this chapter, we evaluate whether the properties of fluid inclusions in orogenic gold deposits can be used (1) to discriminate between auriferous and non-auriferous samples in different geological backgrounds and (2) as potential vector tools towards mineralization. Fluid inclusion studies range from simple petrography performed with a standard microscope to complex methods such as microthermometry and Raman spectroscopy. Microthermometry and Raman spectroscopy can provide quantitative compositional results but are comparatively expensive in terms of time and analytical access. Additionally, thermometry and Raman Spectroscopy are in-situ analyses performed at micron-scale and therefore typically focus on a few inclusions in a small number of samples. In contrast, large numbers of samples are needed to be analyzed in exploration. The crushing stage offers a method to qualitatively assess the volatile content of fluid inclusions and allow processing large numbers of samples in a short time without access to expensive analytical equipment (Roedder, 1970). In this study, we have performed fluid inclusion crushing analyses on samples from underexplored claims as well as on mineralized samples from the historic mining sites in the Yellowknife greenstone belt. Raman spectroscopy has been used to determine the chemical components in the dominant fluid inclusion types associated with mineralized and unmineralized samples. Both tests indicate that volatile-rich fluids occur preferentially associated with gold mineralization. The results from crushing tests and Raman analyses in mineralized samples are consistent and, for the most part, distinct from those in unmineralized samples indicating the potential value of the crushing test as an exploration tool.

3.2 Methods

Thirty-two widely-spaced auriferous and barren quartz vein samples (Fig. 1 and 2) were collected from the Quyta-Bell property and their assay values (Appendix A) were obtained from Gold Terra Resource Corp. The majority of the vein samples studied were hosted either in the Kam group (8 samples with 6 of them assayed) or Burwash group (21 samples with 17 of them assayed), while only two samples (with one of them assayed) hosted in Banting formation were studied. Forty-two samples of quartz and carbonate veins from underground mine sections and surface exposures of the Giant mine were obtained from Kevin L. Shelton and Ed van Hees. In this study, we considered a sample auriferous if it contains > 0.2 ppm Au or if it was collected from a known ore-zone. Double-polished thick sections suitable for fluid inclusion work were prepared and fluid inclusion petrography was made in BX53 Olympus petrographic microscope at the University of Alberta.

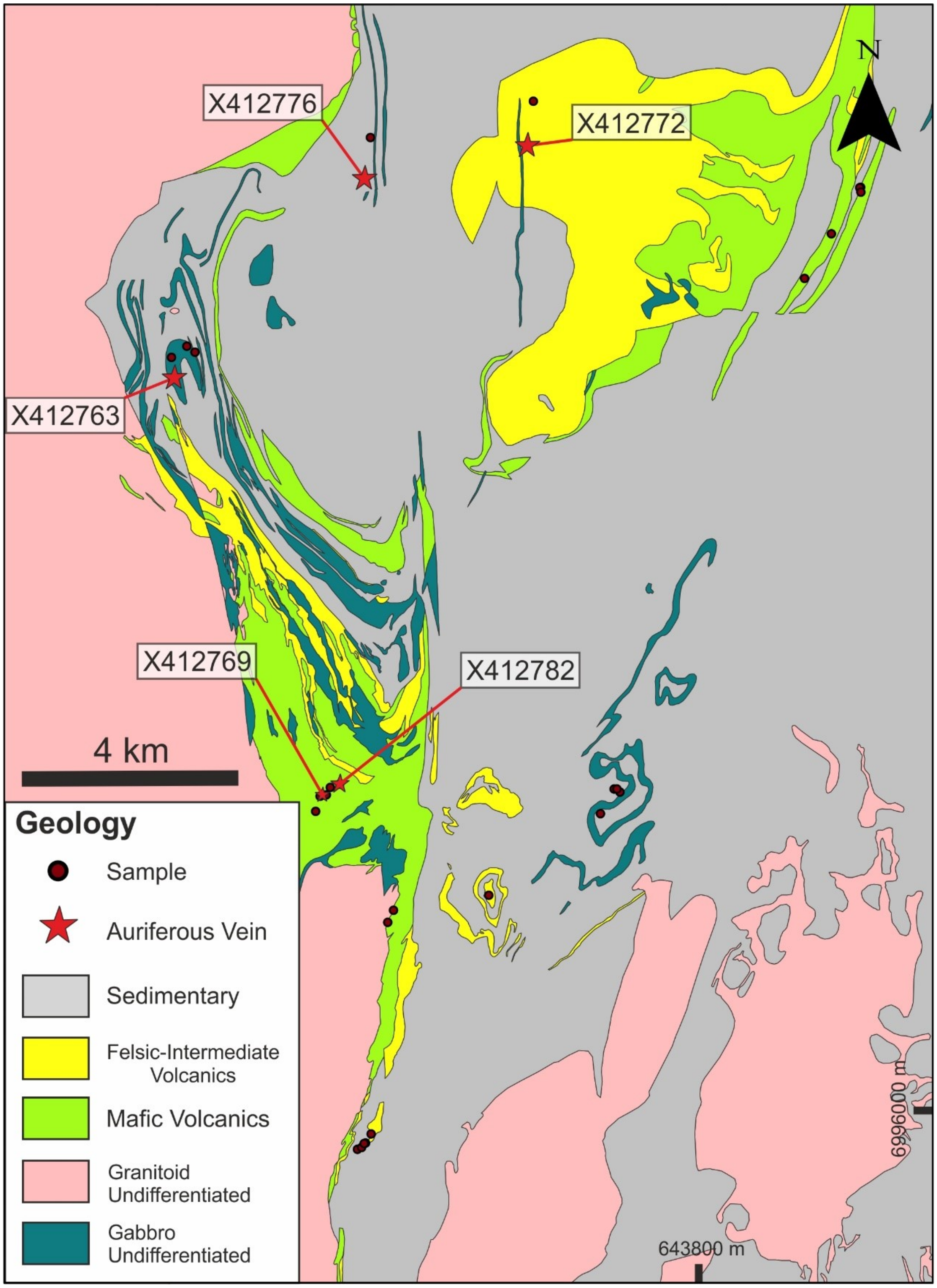

Figure 2. Simplified geological map of the Quyta-Bell property with the location of collected vein samples (Modified after Stubley and Irwin, 2019). Auriferous veins were labeled. Coordinates of the samples can be found in Appendix A. NAD83 UTM:11N

Fluid Inclusion Crushing-Stage Test

After the introduction of the crushing-stage test (Deischa, 1950) several fluid inclusion studies have been performed to evaluate the applicability of crushing tests to characterize fluids (Roedder, 1970; Roedder, 1984; Diamond and Marshall, 1990). This test is performed with a crushing stage (Fig. 3) assembled following the specifications described by (Diamond and Marshall, 1990). The test is carried out by submerging fluid inclusion-bearing quartz grains smaller than 1 mm in an oil in which volatiles are insoluble between two microscope glass slides. In our study, we used a general-purpose immersion oil as a medium where CO_2 is mostly insoluble. Progressively pressing the glass slides together with the screw causes the mineral grains to yield and break. Crushed grains are observed with the help of a microscope or a hand lens through the viewing window located at the top and bottom of the crushing stage. Volatiles within the fluid inclusions (e.g., CO_2, CH_4, N_2) can be highly pressured relative to the atmospheric pressure. When the grain is crushed and exposed to the atmospheric pressure volatiles will expand (Fig. 3). The increase in volume indicates high volatile pressure and constitute a positive crushing test. This test is therefore based on observing and qualitatively assessing the change in volume of the volatiles that are released from the crushed grains. In this study, we follow a similar approach to (Diamond and Marshall, 1990) and give a value to each test; a sample is considered to have no high-pressure volatiles (score of 1) when no bubbles are produced from a grain upon crushing. Samples between 1 and 5 bubbles per grain are considered to have intermediate volatile contents (score of 2) and samples that produce over 5 bubbles per grain are considered rich in high-pressure volatiles (score of 3). We crushed both carbonate and quartz samples. Crushing a mineral that has no potential to carry fluid inclusions will result in a negative test. Since the distribution of fluid inclusions is not necessarily homogeneous and several generations of quartz/carbonate can occur within a sample, 10 grains with approximately similar sizes were crushed for each sample to determine the most common score as representative.

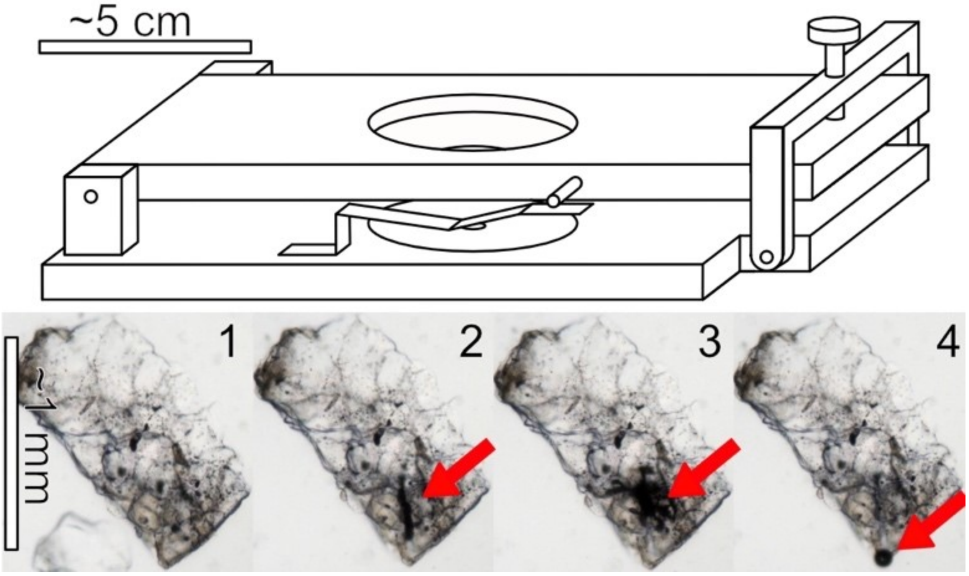

Figure 3. Sketch of a fluid inclusion crushing stage and sequence of pictures of a sample with high-pressure volatiles (Lecumberri-Sanchez et al., 2021). Picture 1 represents quartz grain before crushing. Pictures 2 and 3 show the volatiles being liberated and migrating as the grain is crushed. Picture 4 shows the volatiles liberated from the grain and expanded into a bubble (indicated with red arrow).

Raman Spectroscopy

Raman spectroscopy was used to investigate the chemical composition of the fluid inclusions from the Quyta-Bell property and Giant mine. Spectra were recorded at the University of Alberta using a HORIBA LabRAM HR Evolution confocal spectrometer. The instrument is equipped with a 532 nm excitation laser beam and 600 grooves/mm grating was used to identify volatiles whereas 1800 grooves/mm grating was chosen for obtaining quantitative spectra. Measurements were made with a 50 µm diameter confocal hole size, 30 s acquisition time, and an accumulation of five. To detect CO_2, CH_4, and other minor components wavelengths between 1200-1500 cm^{-1}

and 2000-3700 cm^{-1} were scanned. Gathered data were analyzed with HORIBA Scientific's LabSpec 6 software.

3.3 Results

Crushing-Stage Test at the Quyta-Bell Property

Eighty percent (four out of five) of the auriferous samples from the Quyta-Bell property have a crushing test score of 3, indicating samples are rich in fluid inclusions with high-pressure volatiles (Fig. 4). Additionally, 80% of the barren samples were detected by their low scores (1 and 2) indicating samples are poor and lacking fluid inclusions with high-pressure volatiles. One sample with gold above 0.2 ppm did get a score below 3 and four samples without significant gold (lower than 0.2 ppm) did get an average score of 3. Since the objective of this study is to evaluate the crushing test as a gold indicator, we will refer to samples that have a score of 3 and gold lower than 0.2 ppm as false positives. We will also refer to the sample that has a score of 1 but gold concentrations above 0.2 ppm as false negative. The false negative sample is distinct from all other studied samples both texturally, with open-space filling texture and intense hematite staining, and in terms of the geochemical composition, with copper concentrations orders of magnitude higher than any other of the samples analyzed (Fig. 5 for the texture, Appendix A for the metal content).

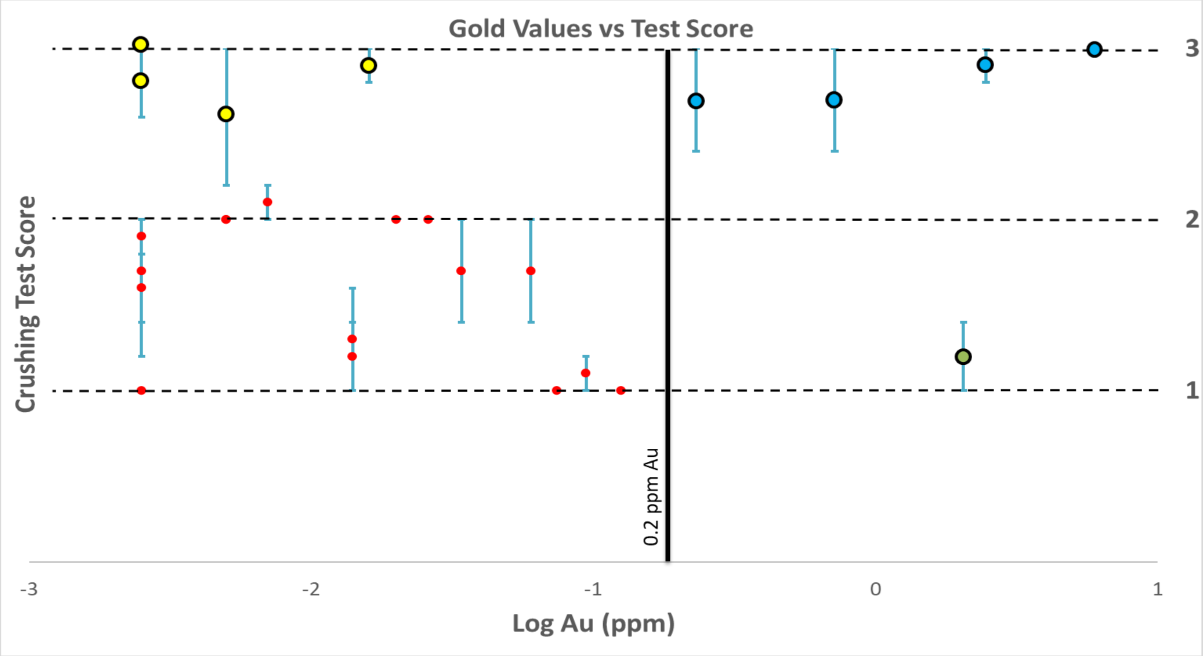

Figure 4. Correlation of crushing stage test results with gold grades for the Quyta-Bell samples. The test score is reported as an average value of 10 tests with a standard deviation. Yellow-colored labels indicate four false positive samples, the blue-colored labels are auriferous samples with a high amount of high-pressure volatiles, the green-colored label is the false negative sample. A score of 1: No high-pressure volatile; 2: Intermediate amounts of high-pressure volatile; 3: Rich in high-pressure volatiles.

Figure 5. Comparison between sample X412763 on right with sample X412780 on left (which is a representation of other Quyta-Bell samples, in terms of texture).

Fluid Inclusion Crushing-Stage Test of the Giant Mine

The distribution of mineralized structures at the Giant mine, unlike Quyta-Bell property, is fairly well known. Therefore, the crushing results of samples from the Giant mine have been evaluated in terms of their distance to mineralized zones instead of their absolute concentration of gold from assay. Samples with high-pressure volatiles are most commonly identified in proximity to known ore zones with a distance of approximately 5 meters (Fig. 6). Contrastingly, samples proximal to barren shear zones do not show high-pressure volatiles. The results listed above belong to crushing tests performed in quartz. Carbonate grains were also crushed but systematically yielded negative results (no high-pressure volatiles identified) independently of whether they were related to mineralized or unmineralized samples. In a few samples from the Giant mine, the test scores were highly variable. In these samples, the majority of the grains are poor in volatiles but in 1 or 2 out of 10 tests very high-pressure volatiles (score of 3) were identified. Apart from these samples, in both Quyta Bell property and Giant mine the crushing test results have relatively low variability, with most grains analyzed in a sample leading to similar consecutive results.

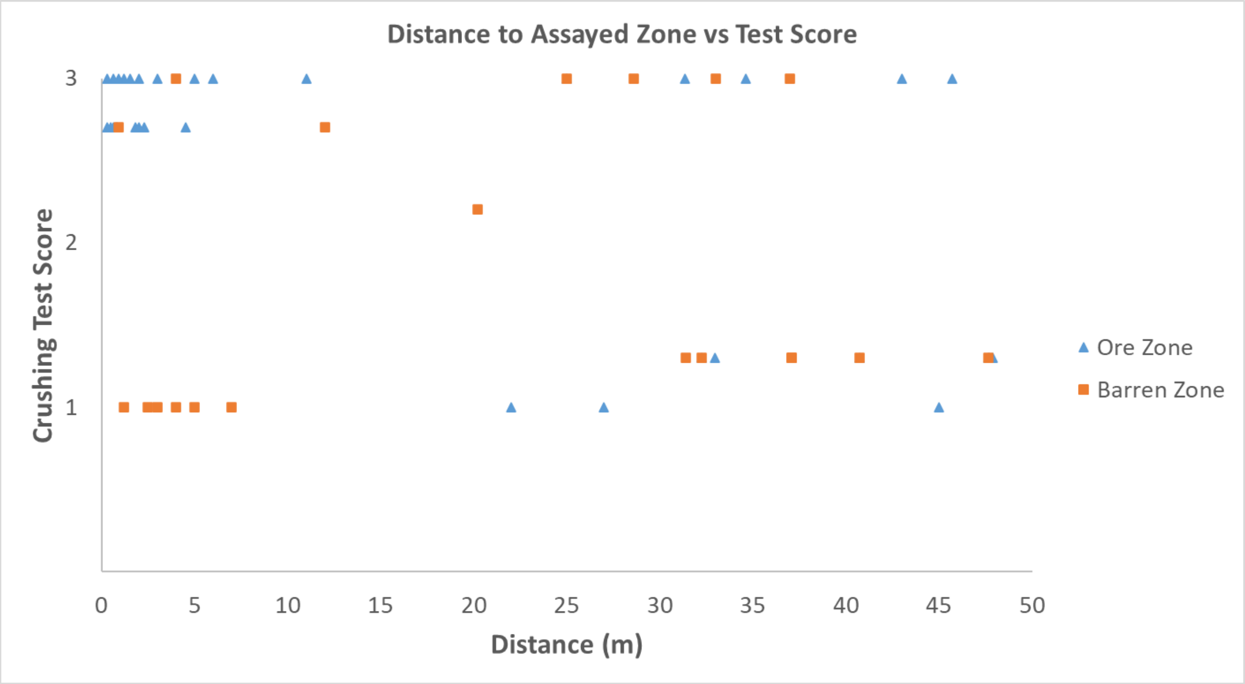

Figure 6. Crushing stage test results of the Giant mine showing the distance of a sample to known barren or gold zones. The majority of the test score 3 samples fall within a distance of 5 meters to the ore zones.

Fluid Inclusion Studies

Thirty-two quartz thick sections from the Quyta-Bell property and 42 quartz-carbonate thick sections from the Giant mine were evaluated under petrographic microscope. Of these samples, some were discarded because of having fluid inclusions that were too small to analyze, poor optics, and/or scarcity of fluid inclusions. Twenty thick sections from the Quyta- Bell property and twenty-nine samples from the Giant mine had fluid inclusions appropriate for Raman Spectroscopy analysis. The size of the fluid inclusions for both sample sets is generally < 25 µm with most inclusions ranging between 1 to 10 µm. Primary and secondary fluid inclusion assemblages in quartz were identified (Fig. 7B and 7D). Where the genetic relationship between fluid inclusions was ambiguous, the group of fluid inclusions was classified as undetermined. The distribution of fluid inclusions in quartz is not homogeneous. Some zones show high density of fluid inclusions while other zones are fluid inclusion absent (Fig. 7F). In general, fluid inclusions are hosted in relatively larger quartz grains, while they are scarce and decrepitated along smaller grains. Post-entrapment modification including decrepitation and necking are common among most of the samples.

Paragenetic relationships between fluid inclusion assemblages and gold mineralization are very scarce in orogenic gold deposits and have not been identified in our samples. In this study, we focus on the spatial relationship between fluid inclusion types and barren vs gold mineralization. In terms of the phase ratios at room temperature and Raman spectroscopic features, seven distinct fluid inclusion subtypes were recognized (Fig. 7). Type I fluid inclusions encompass aqueous fluid inclusions and include two distinct subtypes. Type II inclusions confine carbonic (CO_2-CH_4 dominated) inclusions and include three distinct subtypes. Type III are polyphase brine inclusions and type IV are aqueous-carbonic inclusions.

Two-phase (L_{aq}+V_{aq}) aqueous-dominated, low salinity inclusions with a vapor phase volume between 15-20% are referred to as Type Ia (Fig. 7A). These inclusions are present in most of the samples with varying abundance and occur both as primary and secondary. They are most common in samples with negative crushing test scores and barren samples from both areas. Fluid inclusions in the carbonates analyzed in the Giant mine are dominated by these inclusions.

Two-phase (L_{aq}+V_{aq}) aqueous, low salinity inclusions with a vapor phase volume between 60-70% are referred to as Type Ib (Fig. 7B and C, Fig. 8). These inclusions are restricted only in the false negative sample found in the Quyta-Bell property. Fluid inclusions in this sample are dominantly primary and rarely pseudosecondary (Fig. 7B).

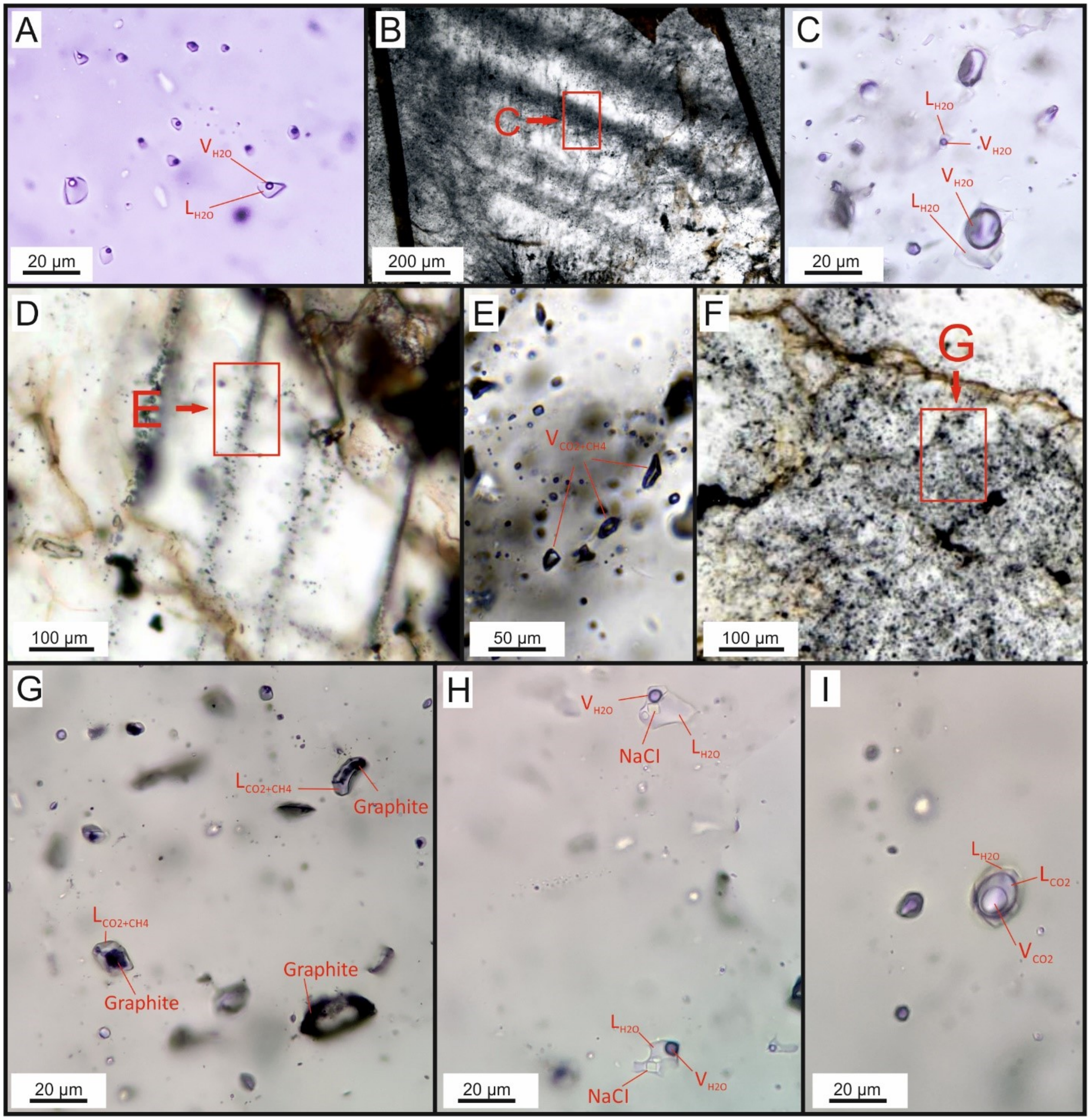

Figure 7. Photomicrographs of fluid inclusion types in quartz samples from the Quyta-Bell property and the Giant mine. (a) Two-phase, type IA aqueous inclusions. (b) Primary, type IB aqueous inclusions located in growth zones. (c) Magnified image of type IB aqueous inclusions. (d) Secondary, type IIa carbonic inclusions. (e) Magnified image of type IIa inclusions. (f) A cluster of polyphase, type IIb graphite-bearing inclusions. (g) Magnified image of type IIb graphite-bearing inclusions. (h) Polyphase, high salinity, type III H_2O-NaCl±$CaCO_3$ inclusions. (i) Three-phase, type IV aqueous-carbonic inclusions.

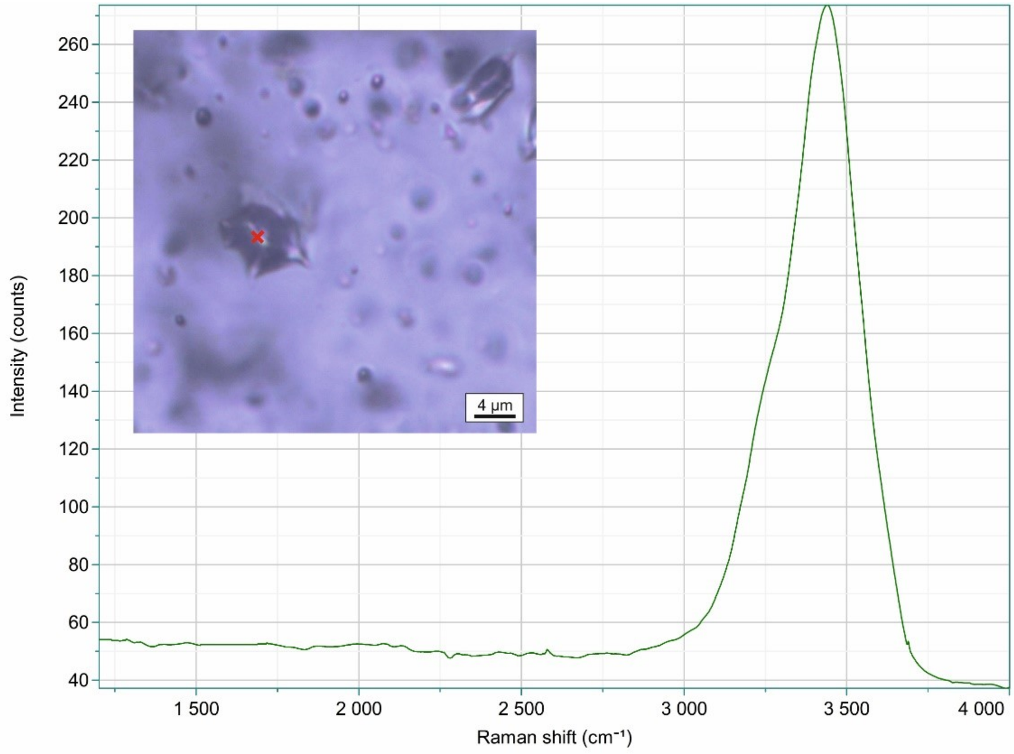

Figure 8. Typical Raman spectra of type IB inclusion from sample X412763. The shoulder on the Raman spectrum is the characteristic OH^- stretching vibration of H_2O.

Two-phase ($L_{carbonic}$+$V_{carbonic}$) or single vapor phase ($CO_2 \pm CH_4$), low salinity, high relief, dark-colored carbonic inclusions are referred to as Type IIa. Type IIa fluid inclusions are most common in samples with positive crushing test scores and gold-bearing samples in both areas. The two-phase variant is more common in the auriferous Quyta-Bell samples, while single-phase Type IIa inclusions are more frequent in the Giant mine (Fig. 9). The presence of CO_2 was recognized by the Fermi doublet between 1280-1282 cm^{-1} and 1385-1387 cm^{-1} (Rosso and Bodnar, 1995). Methane was identified by the v_1 symmetric stretching mode of CH_4 between 2911-2915 cm^{-1} (Brunsgaard-Hansen et al., 2002). Intensity (counts) of the Raman scattering is controlled by the light source, concentration of the sample, and scattering properties of the sample (Roberts and Beattie, 1995). Even with same amounts, CH_4 will have more intensity relative to CO_2 because of its scattering properties (Burke, 2001). The ratio of CO_2 to CH_4 intensity varies dramatically from inclusion to inclusion in the Quyta-Bell property (Fig. 10). In general, samples from the Giant mine are richer in CH_4 compared to the Quyta-Bell property.

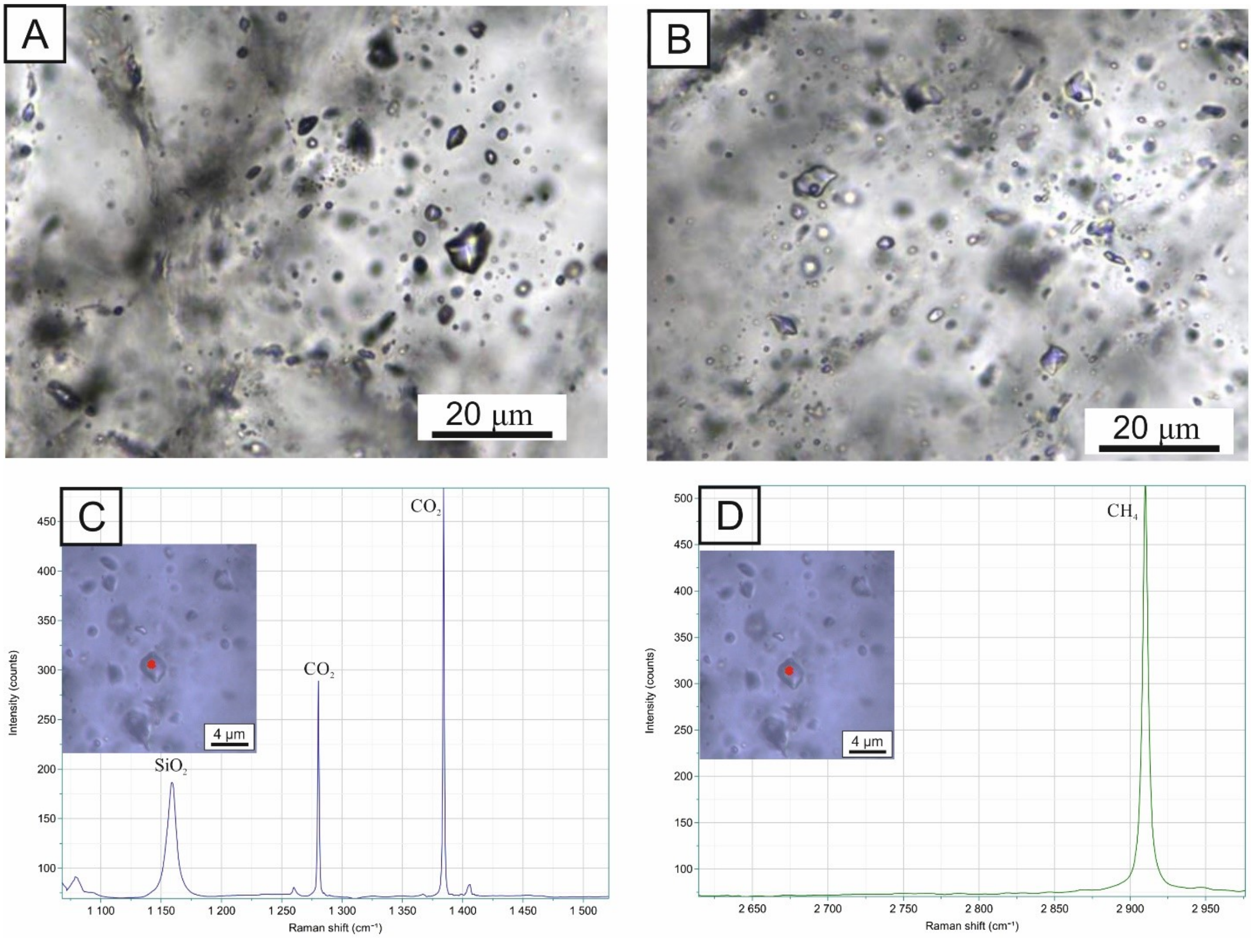

Figure 9. Fluid inclusions observed in the Giant mine. (a) Type IIa carbonic inclusions from the Giant mine are often found in auriferous veins. (b) Rare type Ia aqueous inclusions from the Giant mine are dominant in the barren veins. (c) Raman spectra of Type IIa carbonic inclusions in 1050 to 1550 cm^{-1} band showing the peaks of SiO_2 and CO_2. (d) Raman spectra of Type IIa carbonic inclusions in 2600 to 3000 cm^{-1} band showing the peak of CH_4. Both of the spectra were gathered from a single inclusion (Sample 11895 from the Giant mine).

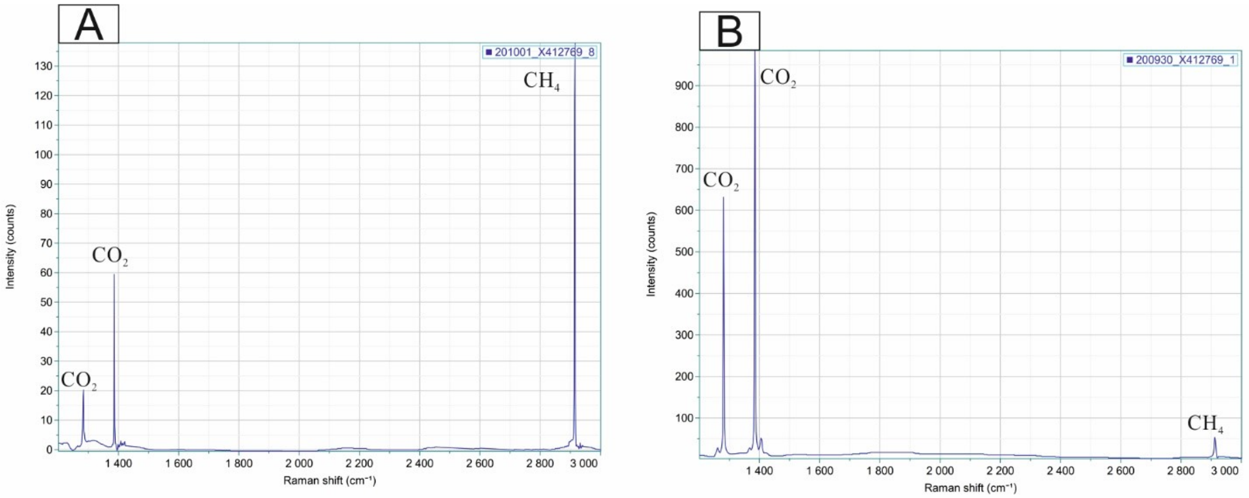

Figure 10. Raman spectrum of different type IIa carbonic inclusions from the Quyta-Bell property. Both of the spectra were taken from auriferous sample X412769. Notice the variation in the CO_2/CH_4 ratios between a and b.

Graphite-bearing carbonic inclusions include poly-phase ($L_{carbonic}+V_{carbonic}$+Graphite) and two-phase ($V_{carbonic}$+ Graphite) low salinity, dark-colored, high relief inclusions and are referred to as Type IIb (Fig. 7F and G). Type IIb inclusions are dominant in samples with positive crushing test scores and gold-bearing samples from the Quyta-Bell property. This inclusion type is rarely encountered in the Giant mine. In the Quyta-Bell property, the presence of graphite is observed as a small opaque solid (< 5 μm) or black-colored stain in fluid inclusions. In the Giant mine, the graphite phase is less abundant. Petrographically, graphite-bearing inclusions from the Giant mine can be occasionally observed as thin films on the inclusion walls or recognized through the Raman spectra (Fig. 11A). Graphite is most commonly associated with fluid inclusions that have varying amounts of CO_2, CH_4, and very rare amounts of N_2 (Fig. 11B). The Raman spectra of graphite in the Quyta-Bell has narrower peaks with higher intensities compared to the graphite from the Giant mine which indicates a higher structural order, in terms of crystallinity (Beyssac et al., 2002) (Fig. 11).

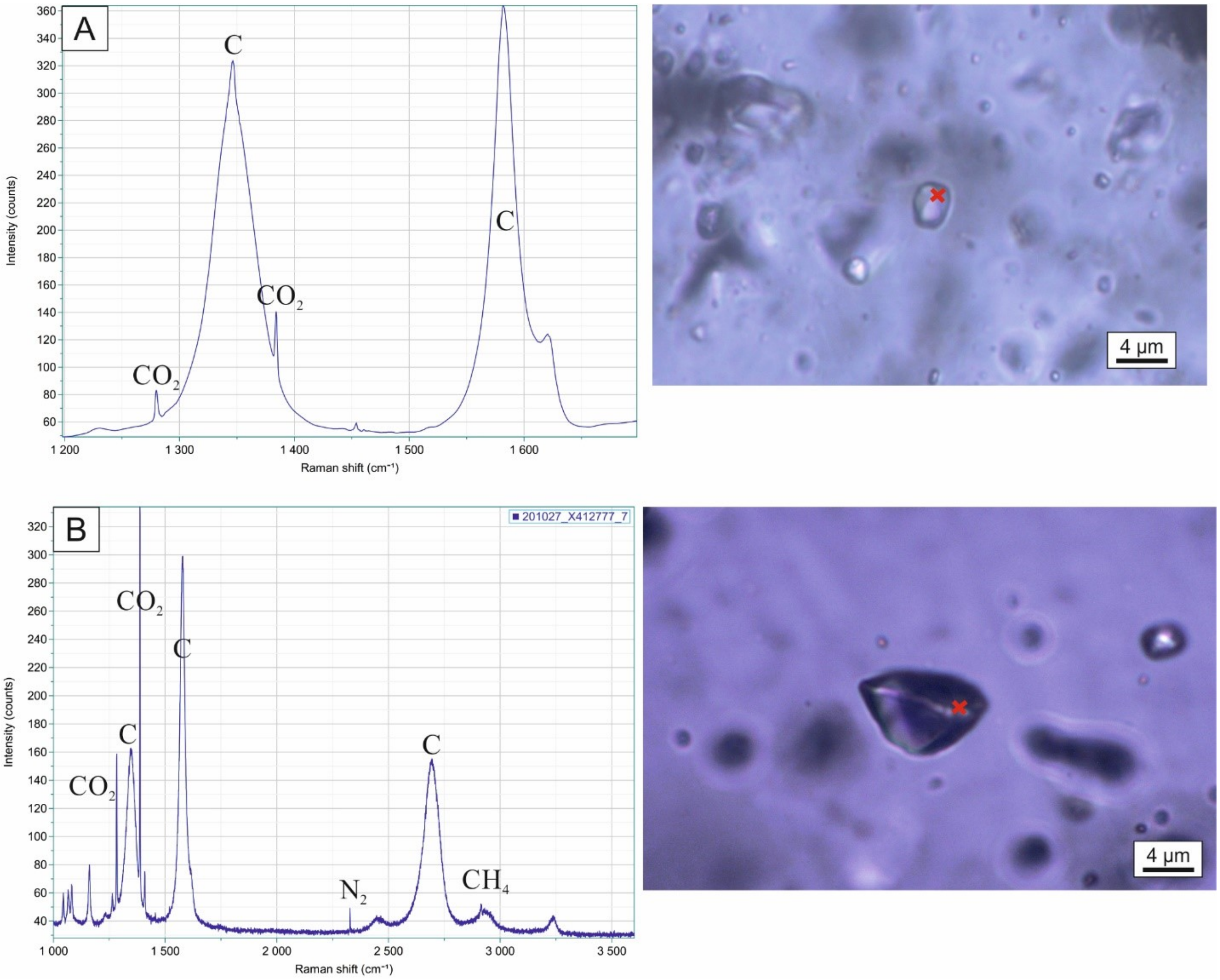

Figure 11. Raman spectrum of type IIb graphite-bearing fluid inclusions. (a) Raman spectrum of type IIb inclusion from the Giant mine (sample 11900). Graphite is concentrated around the walls of the fluid inclusion and the center portion is liquid CO_2. The shape of the spectra shows poor structural order compared to the Quyta-Bell graphite. (b) Raman spectrum of type IIb inclusion from the Quyta-Bell property. Graphite can be recognized as a black-colored opaque solid. The liquid portion of the inclusion consists of mainly CO_2 with minor amounts of CH_4 and N_2. The shape of the spectra shows higher structural order compared to the Giant mine graphite.

Single-phase, low salinity, dark-colored pure CH_4 inclusions are referred to as Type IIc. These fluid inclusions are rare and usually found in secondary fluid inclusion assemblages. Characteristically, they have very strong Raman peaks due to the high Raman activity of methane. In the Giant Mine, pure CH_4 fluid inclusions are present in a few auriferous samples as the only volatile-bearing inclusions.

Type III high salinity, poly-phase inclusions with visible solid phases are occasionally present in samples from the Quyta-Bell property (Fig. 7H). In contrast, they are rarely observed in the Giant mine. Necking is widespread among these inclusions and on occasion, more than one daughter mineral is present at room temperature. Raman spectra showed that the dominant solid phases in these inclusions are ionic solids (e.g., halite) and less frequently calcite.

Type IV inclusions are three-phase, aqueous-carbonic ($H_2O+CO_2 \pm CH_4$), low salinity inclusions. They represent the rarest fluid inclusion type and they are present both in the Quyta-Bell property and Giant mine (Fig. 7I).

Fluid inclusions in auriferous samples from both Quyta-Bell and Giant mine are very rich in carbonic inclusions (type IIa and IIb). In this study carbonic stands for CO_2-CH_4 components and does not preclude trace amounts of N_2. Raman spectroscopy did not identify the characteristic H_2O peak in these inclusions. Percentages of these inclusions in the auriferous samples range between 70-90%. In contrast, type Ia aqueous inclusions are dominant in most of the barren samples and they can reach up to almost 80%. The correlation of type III and type IV inclusions with gold is not clear and we couldn't find a systematic distribution. There is also no systematic correlation between the orientation of the veins and gold content.

The tabulated results of the fluid inclusion study can be found in Appendix B.

3.4 Discussions

Relationship between gold mineralization and crushing test results: implications for exploration

Blind positive crushing results in the Quyta-Bell property identified 80% of the mineralized samples and discarded 80% of the barren samples. As such, crushing test results are considered good preliminary field indicators of auriferous veins. Gold-rich samples are recognized by their abundant high-pressure volatiles and positive crushing test results, whereas barren or regional metamorphic veins have relatively little to no fluid inclusions with high-pressure volatiles which was also proposed by (Diamond and Marshall, 1990) for the Wabigoon and Uchi Archean belts of Canada.

One of the issues for exploration in orogenic gold belts is the nugget effect, which is the result of the inhomogeneous distribution of gold. The nugget effect is a geostatistical artifact associated with sampling that occurs when the majority of metal is concentrated in small particles irregularly distributed throughout the rock. The nugget effect is particularly common for precious metals. As a result of the nugget effect, precious metal concentrations obtained from assays in vein-type gold deposits can lead to overestimation of the average grade if some of those particles are included in the assayed sample. Similarly, assays in vein-type gold deposits can underestimate the average grade of a vein if none of those particles are included in the assayed sample. In contrast, the nature of the fluid composition along a vein is generally homogenous over wide ranges (Mavrogenes et al., 1995). Positive crushing tests in the Giant mine were dominant at distances up to 5 meters from mineralized structures and are not associated with barren structures (Fig. 6). Crushing test results can therefore identify mineralized structures within a 5-meter distance and are unaffected by the nugget effect, providing a reliable indicator of gold mineralization that is relatively independent of sampling procedures. Crushing tests work on a range of scales, from centimeter-scale veins to km-scale regions (Fig. 12). In samples where several generations of quartz are present, the crushing test can compare fluid properties and discard possibly barren veins with no volatile inclusions (Fig. 12B). However, we believe that crushing tests are posed to be most beneficial during the early exploration stage of a project to help narrow down the number of samples and identify structures most likely to be gold-bearing. The Quyta-Bell property is a vast underexplored region in the belt and this method could be used to point potential gold prospects within it (Fig. 12A).

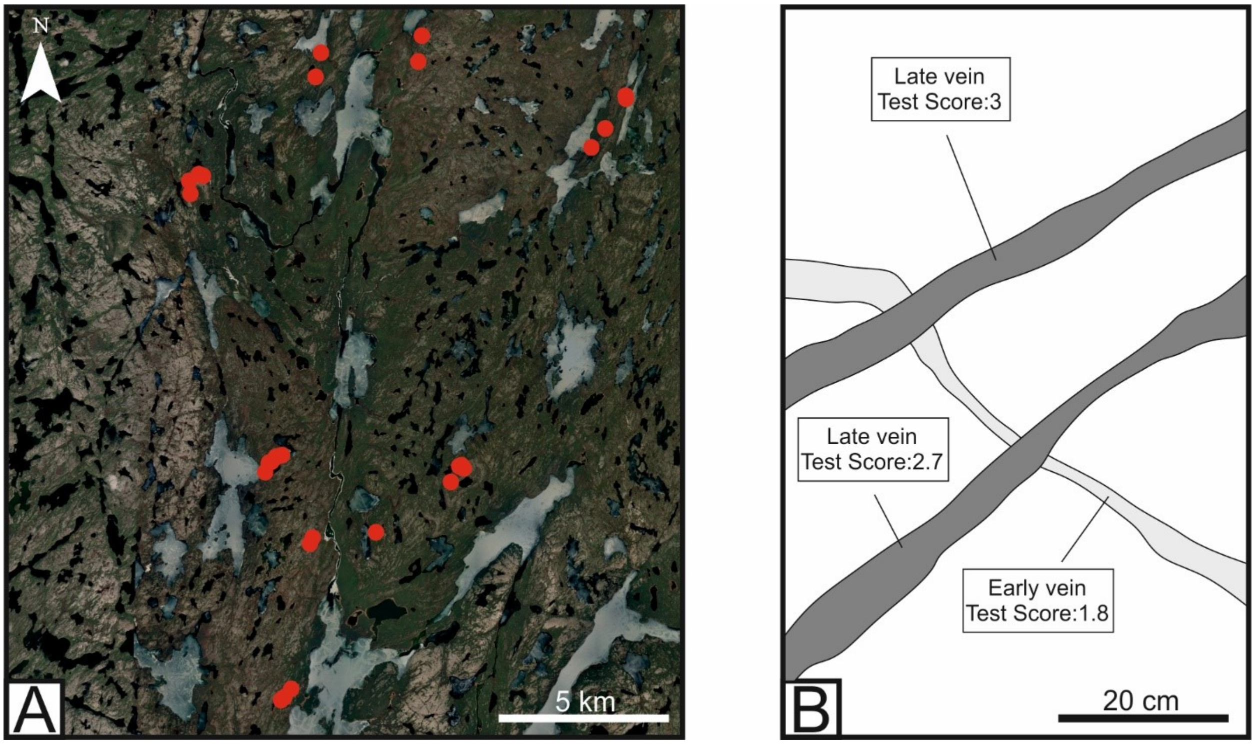

Figure 12. Application of crushing stage test on a different range of scales. (a) Satellite image of the Quyta-Bell property and location of the samples. The crushing test identified the majority of the gold-bearing veins in a km-scale. (b) An illustration of a complex network of veins from the Giant mine. Early vein (possibly barren) with low test score cross-cut by late volatile-rich veins (possibly auriferous). It is possible to differentiate these two separate fluids with the crushing test.

The samples from Giant mine are systematically hosted in Kam group metavolcanics. In contrast, the Quyta-Bell property is broader and in terms of lithology more diverse with samples hosted in Banting, Kam, and Burwash groups. The results from the Quyta-Bell property have successfully identified mineralized samples hosted in each lithology suggesting that the potential of this tool to identify mineralization in the belt is independent of host lithology.

Another rapid test involves the application of heating a sample and observing pressure release due to decrepitation of fluid inclusions (Burlinson, 1988). The pressure-related explosion of fluid inclusions caused by the presence of high-pressure fluid inclusions are detected with a microphone. Being rapid, cheap and, easy this test is very similar to crushing test.

Crushing tests in exploration: potential pitfalls

Low standard deviations in the crushing score suggest similar fluid inclusions are present throughout the sample and high standard deviations indicate heterogeneous distribution of the inclusions. The existence of samples with high standard deviations implies that analysis of a single grain may not suffice to characterize the sample. In this study, we have concluded that 10 crushing analyses including all representative textural quartz are sufficient to provide a crushing score representative of a sample independently of the fluid inclusion distribution.

The structural history associated with orogenic gold often includes several deformation stages. As a result, systems can be extremely complex and it is typical to find barren veins in close association with auriferous veins either predating or postdating them. In samples where several generations of quartz are present, the crushing stage test results will differ depending on the generation of quartz analyzed (Fig. 12B). In a set of late veins crosscutting an early vein, we observed that possible barren veins are giving intermediate scores, while possible mineralized veins have high scores. Therefore, while positive crushing-test results are expected to be indicators of gold, negative crushing test results will only be indicators of a barren structure when all the representative quartz generations have been analyzed.

Four samples in the Quyta-Bell property produced positive crushing tests but had assays with gold concentrations below 0.2 ppm (false positive) (Fig. 4). The false-positive results could be caused by the nugget effect. Therefore, these structures might still be mineralized and further assaying along the structure is recommended.

One sample from the Quyta-Bell property showed negative crushing test results and had gold concentrations above 0.2 ppm (false negative). The most likely explanations for false negative results include decrepitation of the fluid inclusions during the history of the system, and/or differences in the nature of the mineralizing fluid. Multi-stage deformation is common in orogenic gold deposits. Shearing combined with decompression can cause decrepitation (release of fluids from the inclusions and reduction of the internal pressure) (Bodnar, 2003). If volatiles in a sample is lost by decrepitation, the internal pressure of the fluid inclusion may not be sufficient to cause observable bubble expansion during crushing tests. Alternatively, the nature of the fluids associated with mineralization in the false negative sample from the Quyta-Bell may be distinct from other samples. The false negative sample is texturally and compositionally different. Most samples in this study consist of veins or vein-bearing rocks with magnetite as the dominant oxide mineral, no open-space textures, and low concentrations of base metals. In contrast, the false negative sample has a vuggy vein texture suggestive of open-space growth and hematite staining (Fig. 5). Compositionally this sample also has a weight percent level of Cu compared to ppm level in most other samples (Appendix A). The textural, mineralogical, and compositional differences, combined with the differences in crushing test results suggest that the fluids associated with mineralization could be different in this sample. In the Yellowknife greenstone belt, there is evidence of different styles of mineralization, with orogenic gold mineralization being dominant but magmatic-related gold mineralization having been proposed (Ootes et al., 2007). Fluid compositions of porphyry-epithermal systems are noticeably different from orogenic fluids and generally, high-pressure volatiles is not a characteristic feature of them.

Even though the open-space texture is not a classic diagnostic feature of orogenic gold deposits, during the waning stage of mineralization they can be developed (Zoheir et al., 2019; Voisey et al., 2020). Regardless, this sample does not represent typical orogenic gold mineralization, and the volatile vs Au correlation is only valid for orogenic gold deposits.

Correlation between fluid inclusion types and crushing test results

Results of the crushing tests correlate with the presence of specific fluid inclusion types. Type I aqueous inclusions are abundant in the samples with negative crushing results. The main component of these inclusions is relatively low-pressure H_2O and CO_2 below the limit of detection. Type II carbonic (CO_2±CH_4) inclusions are associated with positive crushing tested samples. Bubbles produced after crushing the inclusions in these samples are predominantly high-pressure CO_2. The majority of fluids associated with gold mineralization at both the Quyta-Bell property and Giant mine are CO_2-rich and H_2O-poor fluid inclusions. Pure CO_2 fluid inclusions have been reported in other orogenic gold deposits including the Ashanti Belt Gold deposit (Klemd and Hirdes, 1997; Schmidt-Mumm et al., 1997), Campbell – Red Lake Gold deposit (Chi et al., 2006), Damang Gold deposit (White et al., 2013), Hamadi Gold (Cheng et al., 2017). However, the origin of pure CO_2 inclusions remains controversial. Phase separation of an original H_2O-CO_2 fluid was proposed as a valid mechanism for the entrapment of pure carbonic inclusions (Hollister, 1988; Garba and Akande, 1992). However, detailed thermodynamic studies showed that this cannot be achieved by fluid immiscibility (Li et al., 2020). Moreover, gold transportation and SiO_2 solubility in carbonic fluids are very limited (Klemd, 1998). Post-entrapment modifications, such as deformation/recrystallization (Craw and Norris, 1993; Johnson and Hollister, 1995; Klemd, 1998) could result in the removal of H_2O and favor CO_2

enrichment. In the Giant mine, the presence of pure CO_2 inclusions was attributed to both post-entrapment modification and fluid unmixing (Shelton et al., 2004). We also found pieces of evidence for both of the proposed mechanisms. Yet, they are not very common and we are not going to reach any conclusions with the amount of data we have.

Raman analysis of the inclusions in the false negative sample didn't recognize any CO_2 or CH_4. Type Ib inclusions are dominant in this sample and morphologically they resemble intermediate density fluids commonly encountered in the porphyry-epithermal systems (Landtwing et al., 2010). These types of inclusions were not recognized in any of the past studies done on gold deposits in the Yellowknife greenstone belt. However, it would be risky to assume these inclusions are intrusion-related just by looking at the morphological features. We would like to emphasize here that the fluid inclusions of the false negative sample are very different from the other samples.

In the Quyta-Bell property, gold-bearing samples also correlate with graphite-bearing inclusions. Their origin and relation to the gold occurrences will be discussed in the next chapter.

3.5 Conclusions

Crushing tests at the Quyta-Bell property and Giant mine have shown that high-pressure volatile-rich fluid inclusions identify gold mineralization and can be used as a proxy of 5 meters independently of the lithology they are hosted in. Raman spectroscopy revealed that the main components in fluids are $H_2O+CO_2\pm CH_4\pm C$ with trace amounts of N_2. High-pressure volatiles detected by the fluid inclusion crushing test are CO_2+CH_4 and provides a basis for revealing potential gold prospects whereas low volatile/H_2O ratios are typical in barren veins. The easiest method to recognize these volatile-rich fluids is the application of the fluid inclusion crushing stage test. This study displayed that this test is valid for a variety of host lithologies with different mineralization styles. It presents a reliable and rapid field-based test for the exploration of orogenic gold deposits in the Yellowknife greenstone belt and other goldfields with similar characteristics.

CHAPTER 4

GOLD DEPOSITION IN THE QUYTA-BELL PROPERTY BY HIGH-TEMPERATURE LATE GRAPHITIZING FLUIDS: EVIDENCE FROM RAMAN SPECTROSCOPY AND GRAPHITE THERMOMETER

4.1 Introduction

Gold showings in the Quyta-Bell property correlate with the amount of CO_2 ± CH_4 carbonic inclusions and graphite. Graphite was identified as a common phase hosted in fluid inclusions, as solid inclusions, and as a hydrothermal product overgrowing and forming with sulfides in quartz veins. Orogenic gold fluids are characteristically rich in volatiles; mainly CO_2, with minor amounts of CH_4 and N_2 (Ridley and Diamond, 2000; Bodnar et al., 2013). In contrast, graphite is not a typical feature of orogenic gold deposits and its origin is controversial. C-O-H fluids have the potential to deposit hydrothermal graphite through mixing of different C-bearing fluids (Craw, 2002), fluid cooling (Cesare, 1995; Huizenga, 2001; Huizenga, 2011), change in the ambient oxidation fugacity (Santosh and Wada, 1993), and hydration reactions (Luque et al., 1998). The following reactions have been proposed for graphite precipitation (Ohmoto and Kerrick, 1977; Frost, 1979):

$$CO_2 + CH_4 = 2C + 2H_2O \qquad (1)$$

$$CO_2 = C + O_2 \qquad (2)$$

$$CH_4 + O_2 = C + H_2O \qquad (3)$$

In this chapter, we investigate the graphite occurrences and their relation to gold mineralization in the Quyta-Bell property. We further evaluate the potential mechanisms of graphite precipitation and evaluate its role in gold mineralization. Furthermore, we present the graphite geothermometer based on Raman spectroscopy of carbonaceous matter. Graphite formation is irreversible and the structure of carbonaceous matter is mainly controlled by crystallization temperature (Beyssac et al., 2002). Therefore, Raman analysis of graphite is a useful tool that can provide information on the physical conditions during formation.

4.2 Methods

Petrographic observation under transmitted and reflected light microscopy has been used to identify the genetic associations of graphite.

The Raman spectrum of graphite has been previously used as a quantitative geothermometer (Beyssac et al., 2002; Rahl et al., 2005; Lahfid et al., 2010). In the first-order region (1100-1800 cm^{-1}), the Raman spectrum of graphite is characterized by the G peak at ~1580 cm^{-1}, D1 peak at ~1350 cm^{-1}, D2 peak at 1620 cm^{-1}, and D3 peak at 1510 cm^{-1} (Beyssac et al., 2002; Rahl et al., 2005; Beyssac and Lazzeri, 2012). The shape and intensity of these bands (Fig. 13) are influenced by the degree of crystallinity, which is mostly controlled by the formation temperature of the graphite (Beyssac et al., 2002). Perfect crystalline graphite is characterized by the absence of an observable D2 peak, and higher intensity of the G band compared to the D1 band. As the crystal becomes less ordered, the area of the D1 peak increases and D2 appears as a shoulder near the G peak (Beyssac et al., 2002).

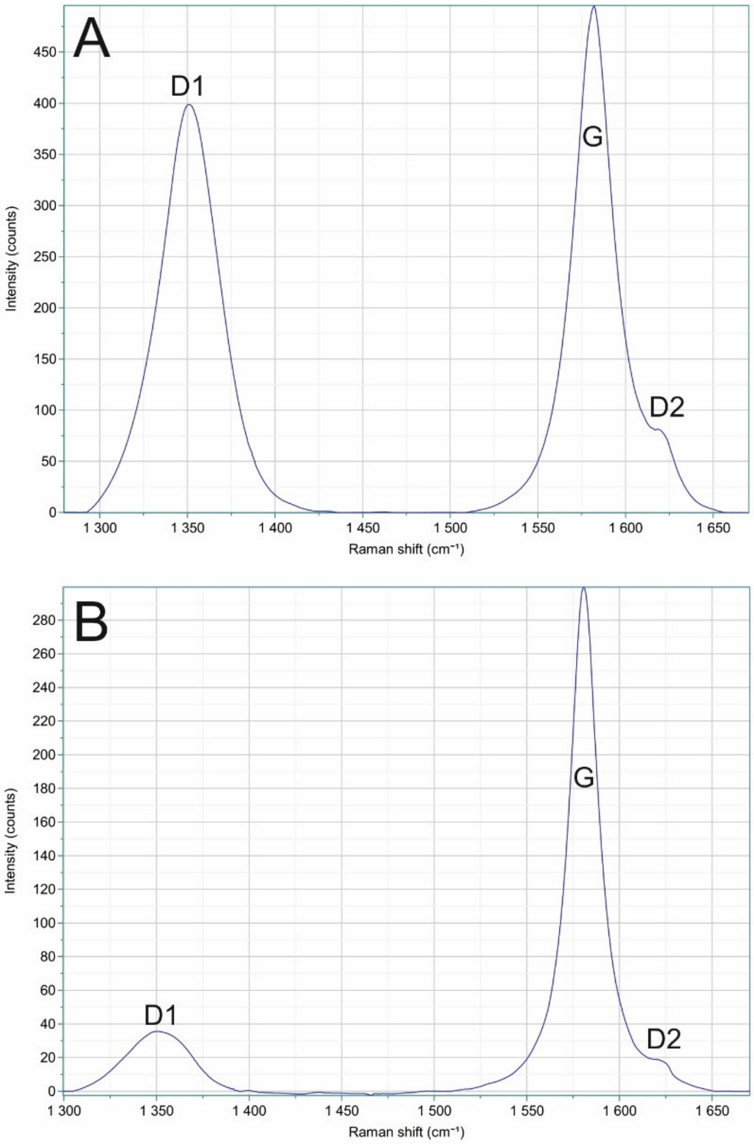

Figure 13. Raman spectra of graphite with characteristic G, D1 and, D2 peaks. (a) Raman spectra of relatively disordered low-temperature graphite analyzed from a fluid inclusion. (b) Raman spectra of high-temperature ordered graphite obtained from a graphite flake.

Raman spectra of graphite in the 1000-1800 cm^{-1} band were recorded at the University of Alberta using a HORIBA LabRAM HR Evolution confocal spectrometer. The instrument is equipped with a 532 nm excitation laser beam and 1800 grooves/mm grating was used during data acquisition. Laser strength was set to 5 Mw to avoid sample heating. Measurements were made with a 100x objective, 50 µm diameter confocal hole size, with 30 s acquisition time, and averaging over 5 accumulations. Baseline correction was made to the gathered spectra with the LabSpec 6 Spectroscopy Suite Software. The majority of the graphite spectra were gathered from gold-bearing sample x412776 but several spectra were also acquired from samples X412753, X412758, X412769, X412772, X412775 and, X412777. We analyzed a total of 50 graphite crystals for thermometric calculations; 14 are inclusion-type graphite, and the rest 36 are crystalline-type graphite. Among the crystalline-type graphite 7 of them are located along the rims of pyrrhotite and 5 of them are spatially associated with magnetite. Each graphite sample was analyzed 5 times from different but proximal locations and the least noisy spectra were used for the temperature calculation. Analyses gathered from each graphite crystal are generally consistent. Obtaining several spectra from single graphite was not possible for the inclusion-type due to their size. To minimize artifacts derived from thin section preparation, when possible graphite spectra were acquired beneath the surface of quartz. An Iceland spar calcite crystal was used for calibration. (Beyssac et al., 2002) introduced two parameters to represent the degree of crystallinity of graphite:

$$R1 = \left(\frac{D1}{G}\right)H$$

and

$$R2 = \left(\frac{D1}{G + D1 + D2}\right)A$$

The application of the Raman Spectroscopy to the graphite geothermometer is based on peak areas and peak heights indicated in the formulas as A and H. Peak fitting and peak parameters including intensity and area calculations were done with the OriginPro 2019 and LabSpec 6

Spectroscopy Suite software using a Lorentzian function (Fig. 14). The specifications described by (Beyssac and Lazzeri, 2012) were used during peak area calculations.

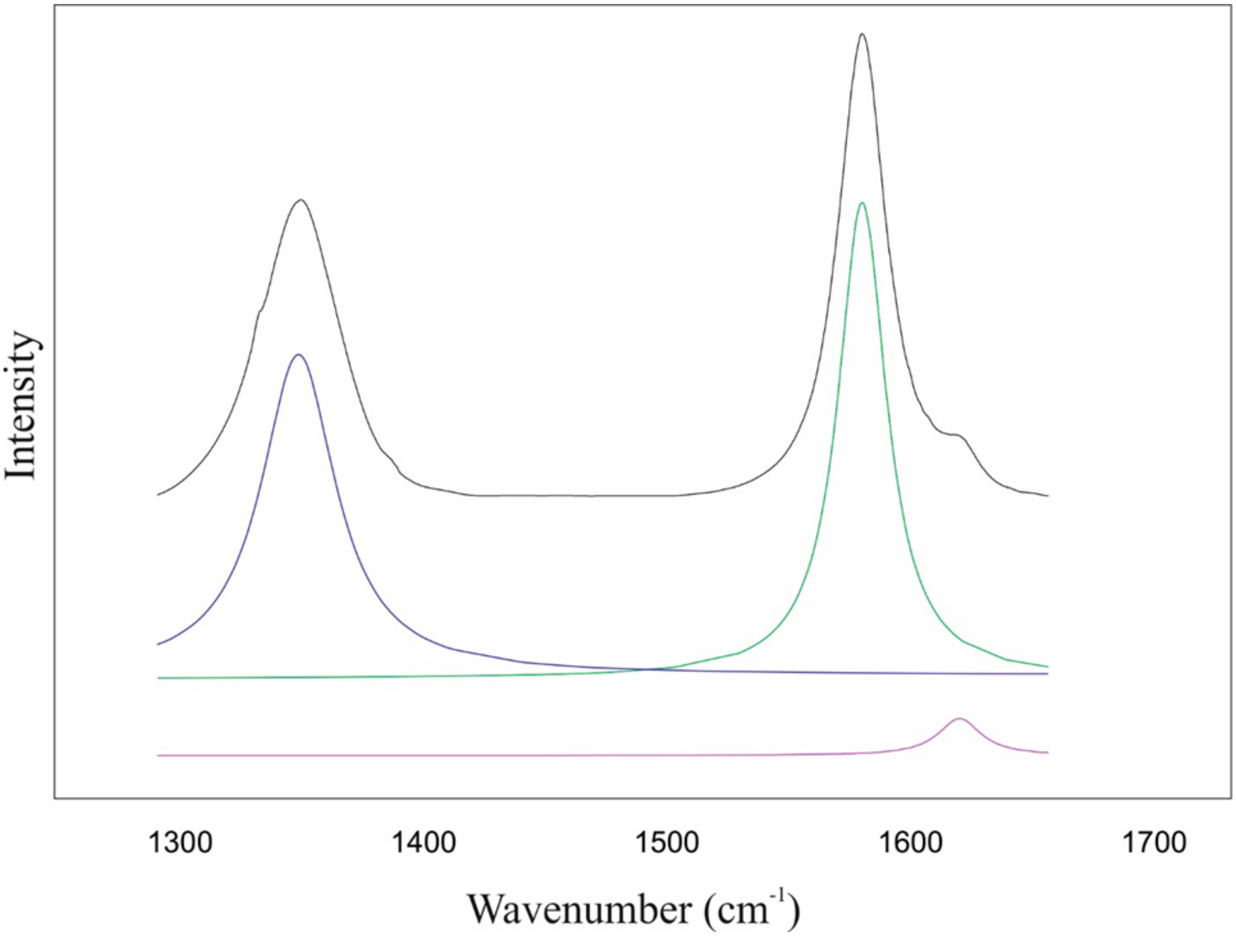

Figure 14. Deconvolution of inclusion-type graphite. The magenta color shows the D2 peak, the green color for the G peak, and the D1 peak is the blue color. The black color is the actual collected spectra.

Temperature calculations were made with equation (4) obtained from the modified graphite thermometer of (Shelton et al., 2016). This thermometer was chosen because of its range of temperatures between 100-700 °C.

$$T(°C) = 737.3 + 320.9R1 - 106R2 - 80.3638R1^2 \tag{4}$$

with the fit parameter of R2 = 0.94

4.3 Results

4.3.1 Petrographic Relationships of Graphite in the Quyta-Bell Property

Two types of graphite were identified during the microscopy study: (1) inclusion-type graphite occurring as inclusions within quartz; (2) hydrothermal graphite usually overgrowing or crosscutting iron sulfides. In this thesis, the latter is named “crystalline-type graphite” because of its relatively higher structural order.

Inclusion-type Graphite

This type of graphite is found inside fluid inclusions as black colored opaque solids with or without a varying amount of liquid and vapor phases (Fig. 15E, F, G, H). In the previous chapter, these inclusions were classified as type IIb. The liquid/vapor phase in these inclusions consists of CO_2 and CH_4. Graphite in these inclusions varies between 2 to 10 µm and it occurs as crystals in the middle of the inclusions or forming a thin rim within the inclusions. In a few gold-bearing samples, graphite inclusions are hosted in late pseudosecondary quartz domains as clusters (Fig. 15A, B, C, D). It is common to observe crystalline-type graphite deposition on the edges of these secondary quartz generations (Fig. 15B, D), which suggests that the pseudosecondary inclusions in the cores of quartz are representative of a graphite saturated fluid that also precipitated primary graphite inclusions.

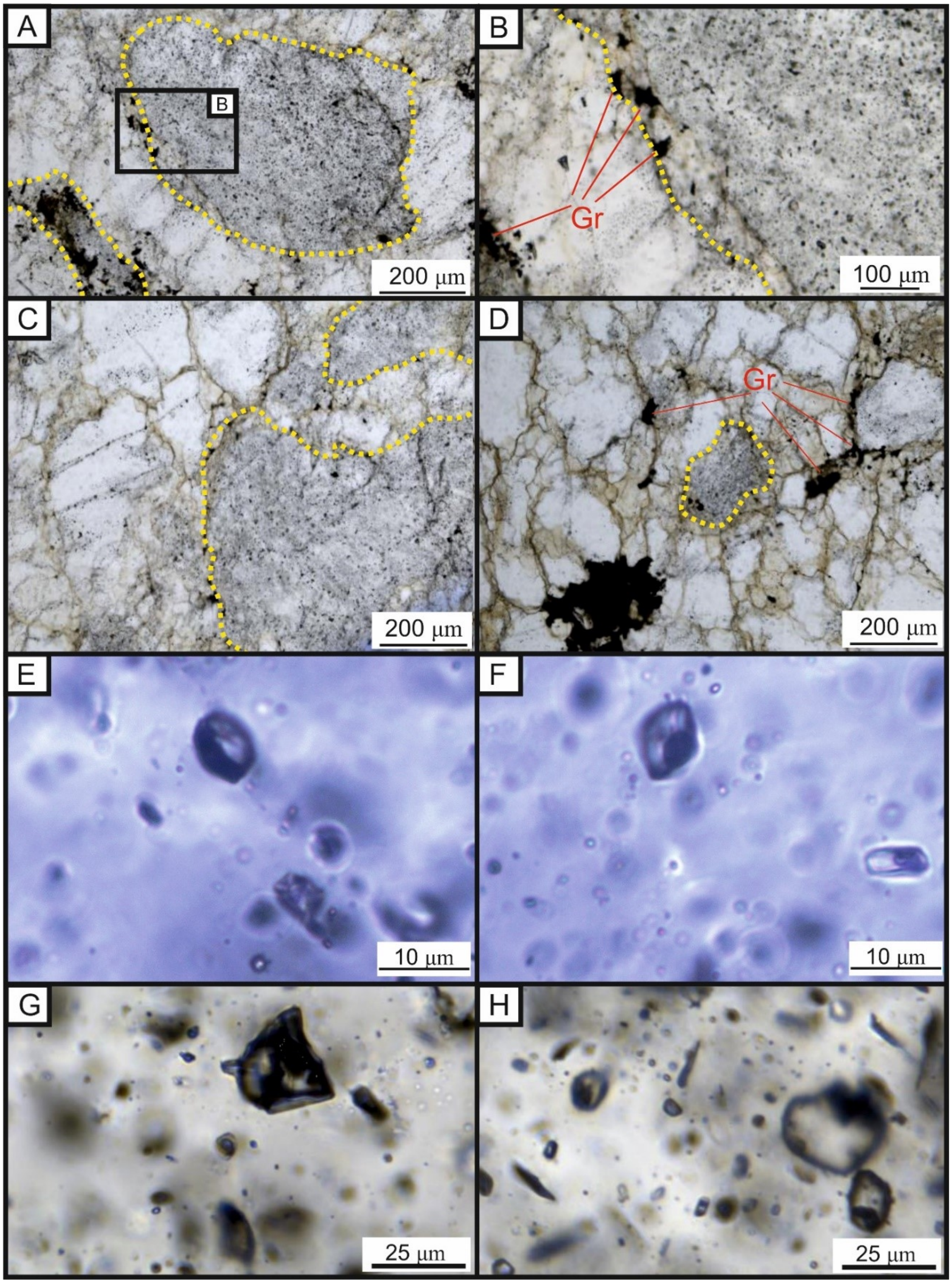

Figure 15. Photomicrographs of inclusion-type graphite. (a), (c), (d) Secondary quartz domains filled with graphite-bearing inclusions. (b) Magnified image from a. Showing the crystalline graphite deposition along the edges of quartz filled with inclusion-type graphite. (e), (f), (g), (h) Graphite-bearing inclusions.

Crystalline-type Graphite

This type of graphite has a flaky texture and is generally observed in fractures and veinlets. The size of this graphite ranges from a few microns to mm scale (Fig. 16). In the veinlets, graphite particles are often found together with pyrrhotite and magnetite (Fig. 17). Graphite systematically overgrowing pyrrhotite indicates a genetic relationship between these two minerals (Fig. 17C, D, E). Both graphite overgrowths on pyrrhotite and graphite vein crosscutting pyrrhotite indicate that graphite postdates pyrrhotite deposition (Fig. 17A, D). Graphite also occurs as small (~5 μm), disseminated, and isolated crystals spatially associated with veinlets and sulfides (Fig. 17B). Less frequently, late pyrite overgrowth on pyrrhotite was observed (Fig. 17E).

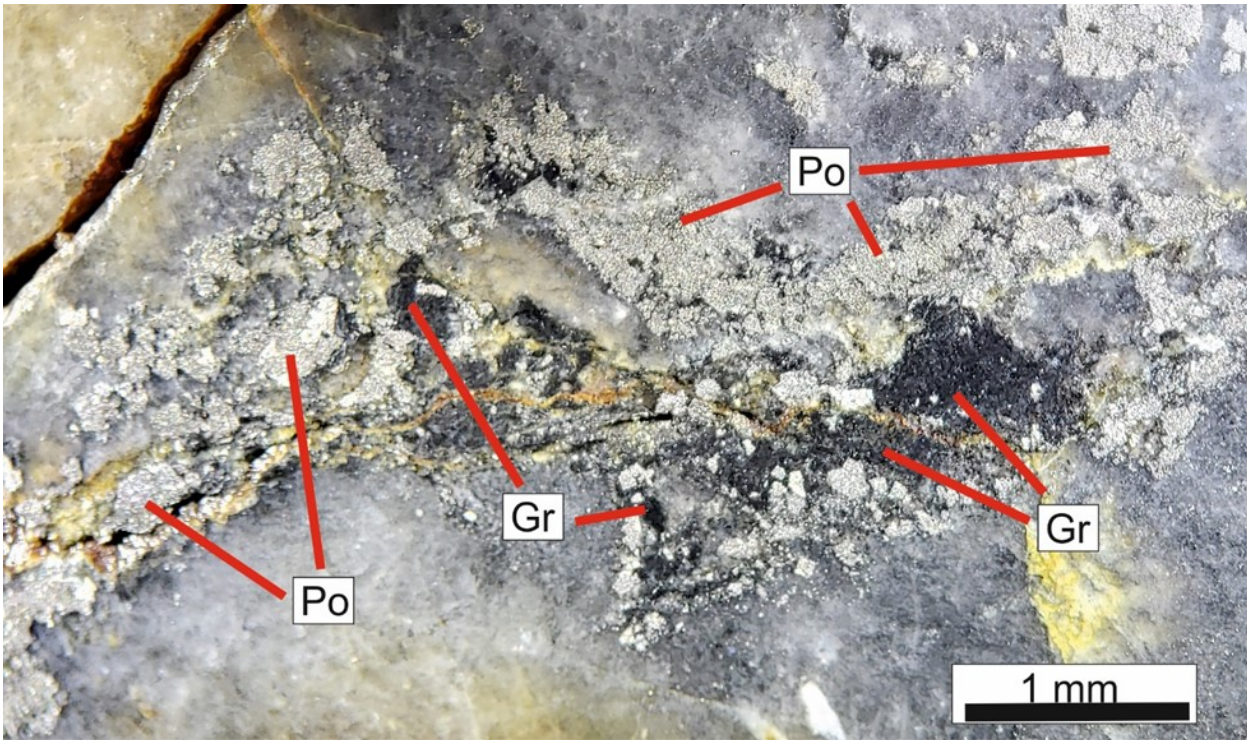

Figure 16. Macrophotograph of quartz vein with graphite and pyrrhotite. (Gold-bearing sample X412776)

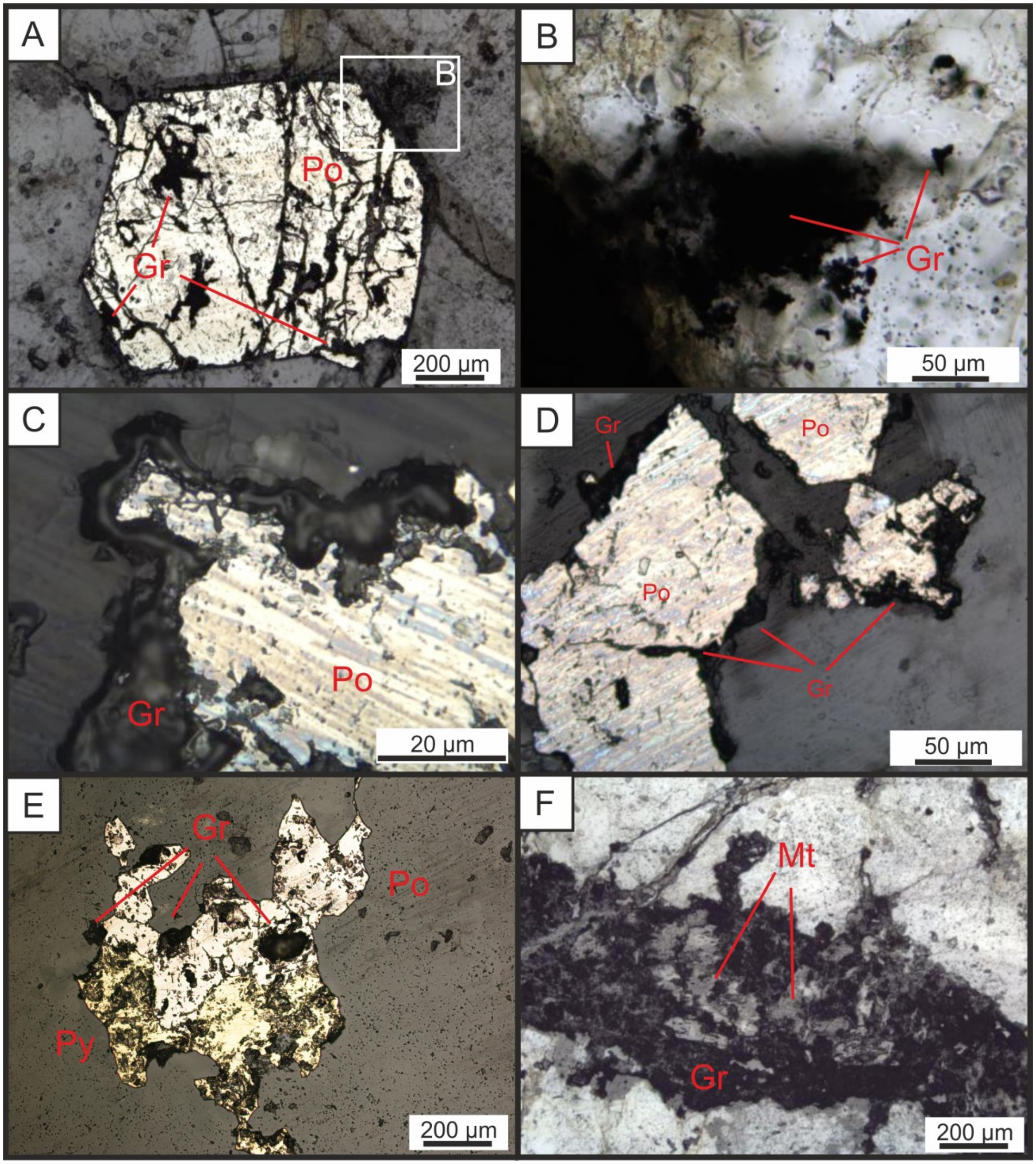

Figure 17. Photomicrographs of crystalline-type graphite under reflected light. (a) Fractured pyrrhotite with secondary intergrowth of graphite. (Bb Magnified image from a (Transmitted Light). (c) Flakes of graphite surrounding the pyrrhotite. (d) Crystalline graphite formed at the edges of pyrrhotite. (e) Early pyrrhotite overgrown by graphite and pyrite. (f) Graphite and magnetite were observed together along a vein. Po: Pyrrhotite; Py: Pyrite; Gr: Graphite; Mt: Magnetite.

4.3.2 Raman Spectroscopy and Graphite Thermometry

The list of samples, areas, and heights of each peak, R1 and R2 ratios, and calculated temperatures are documented in table 1. Raman spectra used for the graphite thermometer can be found in appendix C. Crystalline-type graphite and graphite related with magnetite-pyrrhotite show a relatively higher degree of structural ordering and formation temperatures (Fig. 18). Inclusion-type graphite has a slightly cooler temperature between 404 – 481 °C with a median of 440 °C. Measurements made on crystalline-type graphite documented a temperature between 513 – 572 °C with a 544 °C median. Graphite related with pyrrhotite and magnetite documented slightly higher temperature values between 528 to 609 °C with a median of 568 °C. Temperature calculations on a single sample demonstrate more consistent results with a narrower range of values. For example, calculations for the inclusion-type graphite from sample X412776 resulted in a smaller temperature variation between 437 to 481 °C. Calculations done with the modified graphite thermometer of Rahl et al. (2005) presented reasonable values. The range of calculated temperatures for the crystalline-type graphite indicates lower amphibolite facies conditions.

Table 1. Table 1. Parameters obtained from the Raman spectra peak fitting; temperatures calculated from the graphite thermometer of Rahl et al. (2005).

Sample No	Sample Type	Area			Height		R1	R2	Temperature (°C)
		D1	D2	G	D1	G			
X412776-1	Fluid Inclusion	13253.60	1793.22	18528.57	281.37	463.76	0.61	0.39	481.12
X412776-5	Fluid Inclusion	9290.29	792.69	15256.10	172.39	369.64	0.47	0.37	478.22
X412776-7	Fluid Inclusion	13556.54	1040.00	17032.32	271.65	423.42	0.64	0.43	452.65
X412776-8	Fluid Inclusion	12547.86	807.22	14303.13	247.08	355.32	0.70	0.45	437.38
X412776-16	Fluid Inclusion	4000.13	265.08	7505.80	82.83	263.24	0.31	0.34	467.70
X412776-18	Fluid Inclusion	23309.58	2035.27	29267.50	443.70	652.14	0.68	0.43	462.89
X412776-19	Fluid Inclusion	10190.40	2124.46	13124.53	235.19	411.87	0.57	0.40	466.84
X412776-20	Fluid Inclusion	4886.22	402.21	8690.69	81.40	245.52	0.33	0.35	461.87
X412776-21	Fluid Inclusion	11474.45	1027.33	11544.96	267.28	320.27	0.83	0.48	439.80
X412776-26	Fluid Inclusion	11557.96	1198.03	13109.53	212.97	322.77	0.66	0.45	437.14
X412776-27	Fluid Inclusion	7702.85	560.06	12239.01	154.05	435.01	0.35	0.38	439.94
X412753-1	Fluid Inclusion	14479.00	456.15	15759.50	313.67	474.77	0.66	0.47	410.80
X412753-2	Fluid Inclusion	13099.90	397.62	15229.20	282.59	394.40	0.72	0.46	439.26
X412753-3	Fluid Inclusion	17225.60	784.41	15284.40	401.29	412.19	0.97	0.52	421.25
X412753-4	Fluid Inclusion	33060.37	1769.75	39175.68	611.32	812.25	0.75	0.45	456.48
X412775-2	Fluid Inclusion	8764.49	329.07	8036.22	187.19	223.19	0.84	0.51	403.79
X412775-3	Fluid Inclusion	17648.40	284.51	22162.90	349.56	676.98	0.52	0.44	411.85
X412777-1	Fluid Inclusion	4813.15	149.40	8577.08	99.72	239.48	0.42	0.36	477.63
X412777-2	Fluid Inclusion	6291.76	362.30	7674.49	130.79	209.74	0.62	0.44	437.53
X412776-3	Crystalline	2252.34	147.24	10291.67	36.28	317.43	0.11	0.18	583.56
X412776-4	Crystalline	2723.41	36.21	10712.10	52.52	338.48	0.16	0.20	569.45
X412776-6	Crystalline	2406.86	296.19	7104.32	53.48	230.97	0.23	0.25	545.42
X412776-14	Crystalline	1446.48	63.70	4688.49	25.00	182.78	0.14	0.23	530.70
X412776-15	Crystalline	2888.27	181.57	8437.47	54.92	272.78	0.20	0.25	530.83
X412776-11	Crystalline	4059.60	190.98	12096.06	74.37	445.36	0.17	0.25	523.65
X412776-12	Crystalline	4358.63	64.74	11804.00	92.12	433.49	0.21	0.27	515.26
X412776-22	Crystalline	2630.56	50.25	7347.03	58.30	264.77	0.22	0.26	524.14
X412776-23	Crystalline	530.82	5.97	2087.08	11.02	78.99	0.14	0.20	564.63
X412776-31	Crystalline	1688.47	69.21	4428.44	37.06	166.48	0.22	0.27	513.51
X412776-33	Crystalline	1634.08	93.64	5601.47	28.49	197.28	0.14	0.22	544.06
X412776-34	Crystalline	1431.93	114.74	4943.13	32.10	182.79	0.18	0.22	555.75
X412776-35	Crystalline	1111.92	37.55	4071.11	21.85	156.71	0.14	0.21	553.22
X412776-9	Crystalline	1313.49	169.24	5231.54	21.22	169.60	0.13	0.20	567.45
X412776-10	Crystalline	1715.52	102.00	4306.67	38.35	135.11	0.28	0.28	523.00
X412776-17	Crystalline	1544.34	194.91	4712.84	37.01	184.83	0.20	0.24	542.93
X412776-13	Crystalline	1070.56	187.43	4741.46	19.41	195.67	0.10	0.18	571.80
X412775-1	Crystalline	3155.87	21.57	10066.41	50.88	340.53	0.15	0.24	529.19
X412769-1	Crystalline	7642.70	2369.74	16790.50	131.26	267.68	0.49	0.29	571.02
X412776-2	Near Pyrrhotite	4851.84	5782.60	17762.66	76.44	437.41	0.17	0.17	608.61
X412776-38	Near Pyrrhotite	1788.32	11.36	10271.66	27.37	357.17	0.08	0.15	603.34
X412776-39	Near Pyrrhotite	7324.82	6719.77	20258.98	148.98	493.41	0.30	0.21	599.01
X412776-40	Near Pyrrhotite	3272.79	14121.97	349.13	50.12	437.19	0.11	0.18	576.23
X412776-41	Near Pyrrhotite	1085.58	27.04	4102.06	19.27	125.41	0.15	0.21	562.59
X412776-42	Near Pyrrhotite	1112.51	54.12	3869.71	20.19	127.60	0.16	0.22	550.35
X412776-43	Near Pyrrhotite	1123.95	65.91	3339.94	25.13	133.16	0.19	0.25	530.25
X412758-1	Near Magnetite	1926.52	51.00	8036.84	40.23	302.91	0.13	0.19	573.23
X412758-2	Near Magnetite	4540.35	1935.70	13796.73	78.20	377.41	0.21	0.22	561.36
X412758-3	Near Magnetite	2716.97	26.95	8137.27	49.92	249.21	0.20	0.25	531.92
X412772-1	Near Magnetite	3752.09	2888.50	6182.03	105.90	166.74	0.64	0.29	596.36
X412772-2	Near Magnetite	2295.10	530.38	6106.81	45.28	211.33	0.21	0.26	528.20

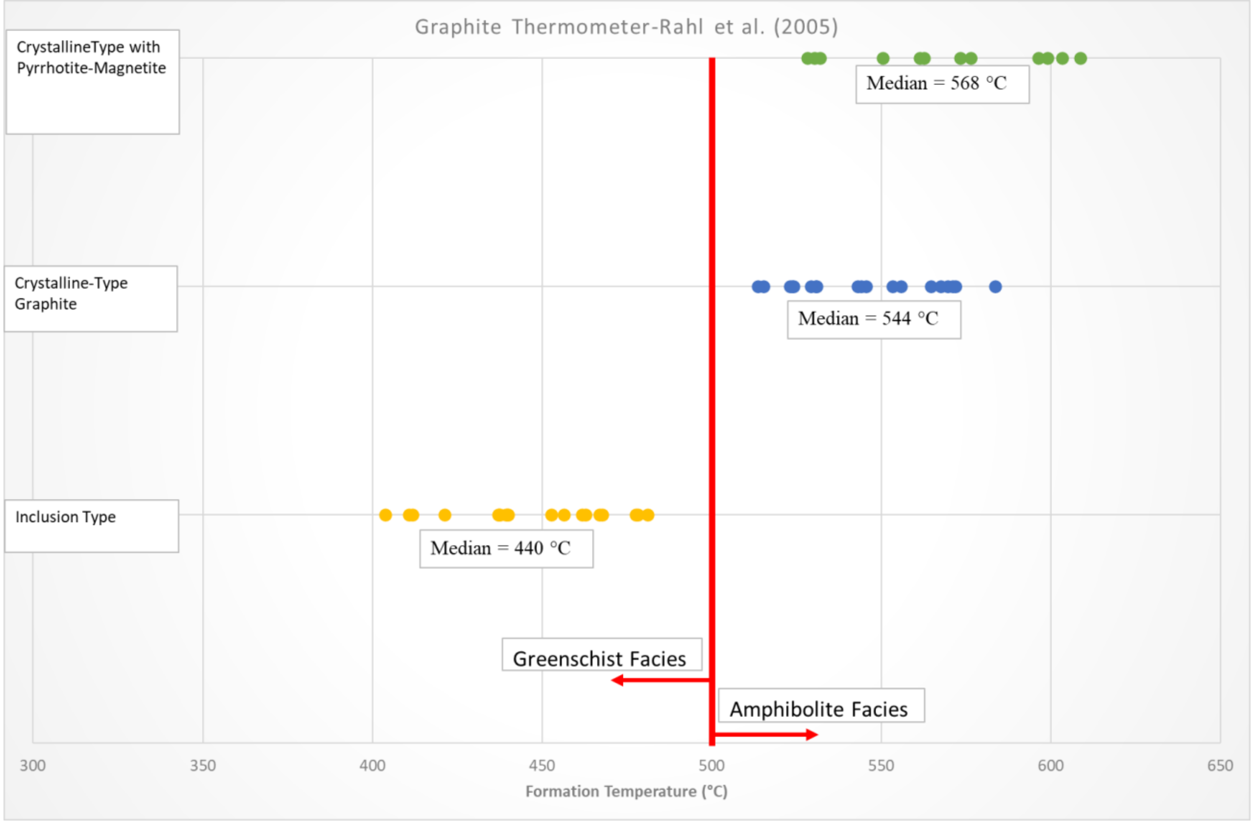

Figure 18. The temperature of formation calculated from Rahl et al. (2005) indicates lower amphibolite facies conditions. Compared to the rest, inclusion-type graphite has a lower formation temperature.

4.4 Discussions

4.4.1 Origin of the Inclusion-Type Graphite

Formation temperatures of inclusion-type graphite are 100 °C lower than the crystalline-type; suggesting a different precipitation mechanism. There are several possible explanations. Graphite-bearing fluid inclusions are dominantly found together with CO_2-CH_4 phases. If the graphite within the inclusions is a trapped phase, we would expect it to show the same thermometric results as the other types of graphite. The lower temperature of graphite within the inclusions suggests that the graphite analyzed is either a daughter mineral precipitated upon cooling of a CO_2-CH_4 mixture within the inclusion, or a layer of lower temperature graphite overgrowing a trapped graphite phase upon cooling. In either case, there is also the possibility that the graphite phase may not be in equilibrium; thus, graphite within fluid inclusions should not be used for the graphite thermometry. Graphite precipitation inside fluid inclusions is known to occur as a result of cooling CO_2-CH_4 fluids described by reaction (1) (Cesare, 1995; Huizenga, 2001; Huizenga, 2011). Possibly carbonic inclusions were trapped at temperatures above 500 °C without forming any graphite. As the temperatures drop, the reaction between CH_4 and CO_2 took place and graphite started to precipitate inside the inclusions. This formation mechanism might explain why the calculated temperature for the inclusion-type graphite is significantly lower.

4.4.2 Temperature Conditions During Graphite Precipitation

The formation temperature of the crystalline-type graphite is calculated between 500 – 600 °C. These temperatures are in agreement with metamorphic conditions of the area and indicate lower amphibolite facies. Garnets encountered in tuff and cordierite occurrences in the metaturbidites of the Burwash Formation showed that metamorphism in the area reached lower amphibolite grade (Pratico, 2009; Hansen, 2013). In the Yellowknife greenstone belt, the metamorphic grade is generally considered as greenschist facies but within proximity to intrusions local amphibolite contact metamorphic aureoles were documented (Davis and Bleeker, 1999; van Hees et al., 2006a; Thompson, 2006). Peak metamorphism in the belt was suggested to befall during “granite bloom”; an event that occurred between 2600-2580 Ma and was characterized by S-type pluton emplacements to the upper crust including the 2592 Ma Prosperous plutons (van Hees et al., 2006a; Ootes et al., 2011). The second stage of regional deformation is also proposed to be coeval with this high-temperature profound metamorphic event (Davis and Bleeker, 1999; Ootes et al., 2011). Similar igneous rocks are also present within the proximity of analyzed samples in the Quyta-Bell property. Emplacement of these intrusions probably led to the lower amphibolite facies conditions and formed the high-temperature graphite observed. Therefore, graphite has to either pre-date (peak metamorphism causing recrystallization of early graphite) or be coeval with peak metamorphism to record those temperatures. Similar temperatures have also been reported in the turbidite-hosted gold mineralization in the Ptarmigan mine. Fluid inclusion data, wallrock mineral assemblages, $\delta^{18}O$ values, and As content of arsenopyrite indicate a metamorphic mineralizing fluid with 550 to 600 ± 50°C temperature in the Ptarmigan mine (van Hees et al., 2006a). Similarly, this deposit is also located within proximity to the 2592 Ma Prosperous pluton which probably caused the local amphibolite facies metamorphism. Gold mineralization in the Ptarmigan mine is suggested to be coeval with peak metamorphism and peak deformation as a result of this intrusion (van Hees et al., 2006a).

4.4.3 Fluid Evolution in the Quyta-Bell Property

The systematic correlation between gold and graphite occurrences in the Quyta-Bell property suggests a genetic relationship. Gold precipitation is therefore likely associated with late-stage high-temperature graphite depositing fluids. In this section, we explore the potential causal relationships between graphite and gold precipitation. Graphite occurs as veinlets crosscutting both pyrrhotite and magnetite (Fig. 17). Graphite overgrowth on pyrrhotite crystals and graphite veinlets crosscutting pyrrhotite indicate that these two minerals are not coeval. Type IIb fluid inclusions (graphite-bearing) are often found in pseudosecondary assemblages in quartz cores surrounded by primary graphite crystals. We interpret that these inclusions and graphite associated with pyrrhotite represent a separate fluid formed after the deposition of pyrrhotite. Based on observed petrographic relations, temperature values calculated from the graphite thermometer, and available literature on the Yellowknife greenstone belt we propose the following mineralization history in the Quyta-Bell property:

The oldest recorded deformation in the Burwash metasedimentary rocks is the F1 folding that occurred between 2660 and 2630 Ma (Davis and Bleeker, 1999). Fluids produced during low-grade early metamorphism may have formed the quartz veins and precipitated the sulfides on these deformational structures. This early sulfide-stage probably occurred during F1 folding, likely associated with fluids generated during greenschist facies and before the peak metamorphism. Analogously, early arsenopyrite and pyrrhotite, pre-dating gold mineralization, have also been reported in the Clan Lake area by other authors (Hansen, 2013). The emplacement of S-type granites (i.e., 2592 Ma Prosperous pluton) to the upper crust initiated peak metamorphism conditions and a second regional deformation event (D2) (Davis and Bleeker, 1999; Ootes et al., 2011). Previous veins and associated sulfide minerals were deformed and fractured during this event. The temperature reached lower amphibolite conditions and high-temperature fluids were generated. Late-stage fluids precipitated the graphite along new fractures formed on early-stage sulfides and quartz. Most likely gold is also associated with these late-stage graphite depositing fluids. This is evidenced by the correlation between graphite and gold-bearing samples from the Quyta-Bell property. Similar, two-staged deposition mechanisms have been suggested in different deposits located in the Yellowknife greenstone belt by other authors (Shelton et al., 2004; van Hees et al., 2006a).

4.4.4 Hydrothermal Graphite Mineralization

Hydrothermal graphite deposition from C-O-H fluids can be achieved by (1) Mixing relatively oxidized CO_2-rich fluids with reduced-CH_4 rich fluids (Craw, 2002), (2) introducing an oxidized CO_2-rich fluid into a reduced environment (Santosh and Wada, 1993), (3) removal of H_2O with hydration reactions (Luque et al., 1998), (4) isobarically lowering the temperature or isothermally increasing the pressure (Cesare, 1995; Huizenga, 2001; Huizenga, 2011).

(1) Mixing Fluids

Fluid inclusion analysis from previous showed highly variable CO_2/CH_4 ratios in the mineralizing fluids. A fluid inclusion study conducted in Arseno and Greyling Lake, located 30 km north of the Yellowknife, also reported a large range of densities in CO_2 + CH_4 fluid inclusions (Shelton et al., 2016). The origin of these inclusions was proposed to be post-entrapment modification from early H_2O-CO_2 inclusions. In the same study, $\delta^{18}O$ values of quartz veins from the mineralized zones documented the influences of both metavolcanic and metasedimentary derived fluids (Shelton et al., 2016). Fluids generated from metavolcanic and metasedimentary reservoirs might form two distinct fluids with different ratios of CO_2 and CH_4. Most likely a fluid generated by the decarbonization of organic-rich sedimentary rocks will be relatively rich in CH_4. Both rocks are present in the Quyta-Bell property. CO_2 ± graphite, CH_4 ± graphite, and CO_2 ±CH_4 inclusions with varying amounts were observed together in most of the gold-bearing samples. Mixing of these relatively reduced and oxidized fluids with reaction (1) can be a probable mechanism for the deposition of graphite and gold. Graphitization of the host rocks will create a zone with higher reducing potential (Craw, 2002). As the gold-bearing fluids pass through this graphitized zone, they will be reduced and initiate gold precipitation (Connolly and Cesare, 1993; Phillips and Powell, 2010; Zhang and Zhu, 2019).

(2) Removal of H_2O

Several studies documented extensive sericite alteration and silicification of wallrocks in the Clan Lake area (Pratico, 2009; Hansen, 2013). This type of alteration can be simply shown by Orthoclase + $H_2O_{(fluid)}$ → Muscovite + Quartz. These reactions can efficiently remove H_2O from the fluid. Removal of H_2O from reaction (1) will shift it to the right side and lead to more graphite precipitation (Luque et al., 1998). This could be a likely scenario in the Quyta-Bell property. Still, it is controversial whether these reactions will take place in high temperatures (Newton, 1995; Luque et al., 2014).

(3) Reducing Environment

Relatively oxidized CO_2-rich fluids can be reduced by the wallrock as shown in reaction (2) (Santosh and Wada, 1993). Graphite and gold deposition in the Quyta-Bell property is observed in a variety of lithologies including mafic and intermediate volcanic flows, gabbroic intrusions, and mudstones. Given the diversity of rock types, chemical signatures, and fO_2 assemblages in different lithologies, a source of reducing power would be required in all of them. A study in the Clan Lake area showed that pyrrhotite is closely associated with gold and can be usually found along mineralized zones (Hansen, 2013). Our observations also showed a surplus of pyrrhotite in gold-bearing samples. Kirilova et al. (2017) suggested that pyrrhotite could act as a reducing agent for CO_2-rich fluids (5).

$$4FeS + 4H_2S + CO_2 = 4FeS_2 + 2H_2O + H_2 + Graphite \qquad (5)$$

This mechanism would lead to the alteration of pyrrhotite to pyrite and precipitation of graphite from a CO_2-rich fluid. Additionally, coeval gold deposition is triggered by the consumption of H_2S. This reaction can explain the pyrrhotite-graphite affinity and pyrite overgrowths on pyrrhotite (Fig. 17 A, C, D, and E). Even though we found evidence of pyrite overgrowths on pyrrhotite they are not very common.

(4) Cooling Fluids

In a C-O-H fluid, as the temperature decreases, the carbon solubility also decreases (Cesare, 1995). A cooling fluid has the potential to deposit graphite through this decline in carbon solubility. However, the temperature for graphite deposition was calculated between 500-600°C. Given the abundance of graphite, either a large fluid flow through the rock or a larger solubility change (range of temperatures) would be required. As suggested by (Luque et al., 2014), cooling fluids probably have a role in graphite precipitation but that role mostly enhances the main precipitation mechanism rather than leading it on its own.

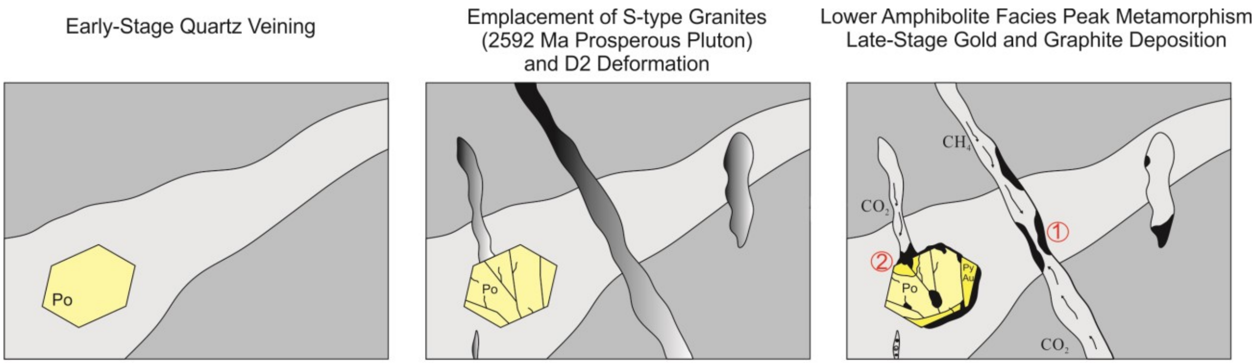

① $CO_2 + CH_4 = 2C + 2H_2O$

② $4FeS + 4H_2S + CO_2 = 4FeS_2 + 2H_2O + H_2 + \text{Graphite}$

Figure 19. Possible mineralization history of the Quyta-Bell property. Early-stage low-temperature fluids precipitated quartz and sulfides. Emplacement of S-type granites initiated the D2 deformation and fractured early veins. Peak metamorphic conditions were reached due to profound magmatism. High-temperature fluids deposited the gold and graphite on these new deformations. One possible mechanism to deposit graphite is through the mixture between CO_2- rich fluids with CH_4- rich fluids. Another depositional mechanism involves the reduction of the fluid by pyrrhotite. Both of these scenarios will lead to the gold formation.

4.5 Conclusions

Graphite is strongly correlated with gold in the Quyta-Bell property suggesting a genetic relationship between these two minerals. While the specific cause for graphite precipitation remains unclear, the interaction between a carbonic fluid and pre-existing pyrrhotite is the mechanism that shows a direct geochemical link between gold and graphite precipitation. This mechanism of precipitation is most consistent with two-stage mineralization where the sulfides predate both gold and graphite precipitation (Fig. 19). Independently of the genetic relationships between both, graphite seems to be a useful indicator mineral for gold deposits in the Quyta-Bell property. Additionally, granitoid intrusions seem to play a more active role in similar high-temperature deposits (i.e., Ptarmigan Mine). Emplacement of these igneous bodies leads to high-temperature contact metamorphism that generates gold-bearing fluids. Participation of these intrusions can help to develop large gold deposits in the area. They should not be considered as direct targets for gold but areas proximal to these plutons might have a higher potential to become major gold deposits.

CHAPTER 5

CONCLUSION

The key conclusions reached in this study can be listed as follows:

- The main Raman active components of the fluids in the Quyta-Bell property and Giant mine are $H_2O + CO_2 \pm CH_4 \pm C$ with trace amounts of N_2.
- The amount of carbonic fluids ($CO_2 + CH_4$) correlates with auriferous veins while aqueous dominated fluids are typical of barren veins.
- Crushing stage test provides a rapid field-based method to identify potential gold prospects by detecting high-pressure volatiles.
- This test can be used as a vector for gold mineralization within 5 meters.
- Graphite-bearing inclusions and hydrothermal graphite are characteristic of auriferous samples of the Quyta-Bell, a prospect hosted in amphibolite facies rocks.
- Graphite is also present in the Giant mine with limited amounts. However, compared to the graphite in the Quyta-Bell property they have poor structural order and lower formation temperature.
- A possible affinity of pyrrhotite and graphite with gold was observed, although petrographic relations indicate that pyrrhotite predates graphite.

- Graphite thermometer documented that the temperature of the graphite precipitating fluid is between 500-600°C. This value is consistent with lower amphibolite facies conditions.

- Metamorphic grade of the area agrees with the graphite thermometer. This suggests that graphite and possibly gold are prior to synchronous with peak metamorphic conditions.

- Possible geochemical processes leading to graphite precipitation linked to gold deposition are mixing of different C-bearing fluids and reduction of the fluid by pyrrhotite.

- Preliminary results indicate that graphite presence can be used as a vector for gold in the Quyta-Bell property.

REFERENCES

Armitage, A., 2019, RESOURCE ESTIMATES FOR THE CRESTAURUM BARNEY-SAM OTTO/MISPICKEL DEPOSITS, YELLOWKNIFE CITY GOLD PROJECT, YELLOWKNIFE, NORTHWEST TERRITORIES, CANADA.:

Beyssac, O., and Lazzeri, L., 2012, Application of Raman spectroscopy to the study of graphitic carbons in the Earth Sciences, in EMU Notes in Mineralogy:, p. Chapter 12, 415–454.

Beyssac, O., Goffé, B., Chopin, C., and Rouzaud, J. N., 2002, Raman spectra of carbonaceous material in metasediments: A new geothermometer: Journal of Metamorphic Geology, v. 20, p. 859–871.

Bleeker, W., and Hall, B., 2007, The Slave craton: geological and metallogenic evolution, in Goodfellow, W. D. ed., Mineral Deposits of Canada: A Synthesis of Major Deposit-types, District Metallogeny, the Evolution of Geological Provinces, and Exploration Methods: Geol. Soc. of Canada.

Bodnar, R. J., 2003, Reequilibration of fluid inclusions, in Fluid Inclusions: Analysis And Interpretation:, p. 213–230.

Bodnar, R. J., Lecumberri-Sanchez, P., Moncada, D., and Steele-MacInnis, M., 2013, Fluid Inclusions in Hydrothermal Ore Deposits: Elsevier Ltd., 119–142 p.

Bove, D. J., Mast, M. A., Dalton, J. B., Wright, W. G., and Yager, D. B., 2007, Major styles of mineralization and hydrothermal alteration and related solid- and aqueous-phase geochemical signatures: US Geological Survey Professional Paper 1651, v. 1.

Boyle, R. W., 1961, Geology, geochemistry, and origin of the gold deposits of the Yellowknife District, Northwest Territories.

van Breemen, O., Davis, W. J., and King, J. E., 1992, Temporal distribution of granitoid plutonic rocks in the Archean Slave province, northwestern Canadian Shield: Canadian Journal of Earth Sciences, v. 29, p. 2186–2199.

Brunsgaard-Hansen, S., Berg, R. W., and Stenby, E. H., 2002, How to determine the pressure of a methane-containing gas mixture by means of two weak Raman bands, v3 and 2v2: Journal of Raman Spectroscopy, v. 33, p. 160–164.

Bullen, W., and Robb, M., 2006, Economic contribution of gold mining in the Yellowknife Mining District, in Gold in the Yellowknife Greenstone Belt, Northwest Territories: Results of the EXTECH III Multidisciplinary Research Project: p. 38–39.

Burke, E.A.J., 2001. Raman microspectrometry of fluid inclusions. Lithos 55, 139–158.

Burlinson, K., 1988. An instrument for fluid inclusion decrepitometry and examples of its application, Bulletin de Mineralogie 111, 267-278.

Canam, T. W., 2006, Discovery, mine production, and geology of the Giant mine, in Gold in the Yellowknife Greenstone Belt, Northwest Territories: Results of the EXTECH III Multidisciplinary Research Project:, p. 188–196.

Cesare, B., 1995, Graphite precipitation in C-O-H fluid inclusions: Closed system compositional and density changes, and thermobarometric implications: Contributions to Mineralogy and Petrology, v. 122, p. 25–33.

Cheng, X. H., Xu, J. H., Wang, J. X., Xue, Q. P., and Zhang, H., 2017, Carbonic fluids in the hamadi gold deposit, Sudan: Origin and contribution to gold mineralization: Canadian Journal of Earth Sciences, v. 54, p. 494–511.

Chi, G., Dubé, B., Williamson, K., and Williams-Jones, A. E., 2006, Formation of the Campbell-Red Lake gold deposit by H2O-poor, CO2-dominated fluids: Mineralium Deposita, v. 40, p. 726–741.

Coleman, L. C., 1957, Mineralogy of the Giant Yellowknife Gold Mine, Yellowknife, NWT: Economic Geology, v. 52, p. 400–425.

Connolly, J. A. D., and Cesare, B., 1993, C-O-H-S fluid composition and oxygen fugacity in graphitic metapelites: Journal of Metamorphic Geology, v. 11, p. 379–388.

Cousens, B., Facey, K., and Falck, H., 2002, Geochemistry of the late Archean Banting Group, Yellowknife greenstone belt, Slave province, Canada: Simultaneous melting of the upper mantle and juvenile mafic crust: Canadian Journal of Earth Sciences, v. 39, p. 1635–1656.

Cousens, B. L., 2000, Geochemistry of the Archean Kam Group, Yellowknife greenstone belt, Slave Province, Canada: Journal of Geology, v. 108, p. 181–198.

Cousens, B. L., Falck, H., Ootes, L., Jackson, V. A., Mueller, W., Corcoran, P., Finnigan, C., van Hees, E. H., Facey, C., and Alcazar, A., 2006, Bedrock geochemistry of the Yellowknife greenstone belt and adjacent areas: Regional correlations, tectonic settings, and stratigraphic solutions: Geological Association of Canada Mineral Deposits Division, Special Publication, v. 3, p. 70–94.

Craw, D., 2002, Geochemistry of late metamorphic hydrothermal alteration and graphitisation of host rock, Macraes gold mine, Otago Schist, New Zealand: Chemical Geology, v. 191, p. 257–275.

Craw, D., and Norris, R. J., 1993, Grain boundary migration of water and carbon dioxide during uplift of granet-zone Alpine schist, New Zealand: Journal of Metamorphic Geology, v. 11, p. 371–378.

Davis, W. J., and Bleeker, W., 1999, Timing of plutonism, deformation, and metamorphism in the Yellowknife Domain, Slave Province, Canada: Canadian Journal of Earth Sciences, v. 36, p. 1169–1187.

Davis, W. J., Jones, A. G., Bleeker, W., and Grütter, H., 2003, Lithosphere development in the Slave craton: A linked crustal and mantle perspective: Lithos, v. 71, p. 575–589.

Deischa, G., 1950, Essais par écrasement de fragments minéraux pour la mise en évidence dinclusions de gaz sous pression: Bulletin De La Société Française De Minéralogie Et De Cristallographie, v. 73, p. 439–445.

Diamond, L. W., and Marshall, D. D., 1990, Evaluation of the fluid-inclusion crushing-stage as an aid in exploration for mesothermal gold-quartz deposits: Journal of Geochemical Exploration, v. 38, p. 285–297.

Dominy, S. C., Johansen, G. F., and Annels, A. E., 2001, Bulk sampling as a tool for the grade evaluation of gold–quartz reefs: Applied Earth Science IMM Transactions section B, v. 110, p. B176–B191.

Ferguson, M. E., Waldron, J. W. F., and Bleeker, W., 2005, The Archean deepmarine environment: Turbidite architecture of the Burwash Formation Slave Province, Northwest Territories: Canadian Journal of Earth Sciences, v. 42, p. 935–954.

Frost, B. R., 1979, Mineral equilibria involving mixed-volatiles in a C–O–H fluid phase: the stabilities of graphite and siderite: American Journal of Science, v. 279, p. 1033–1059.

Gaboury, D., 2019, Parameters for the formation of orogenic gold deposits: Applied Earth Science, v. 128, p. 124–133.

Garba, I., and Akande, S. O., 1992, The origin and significance of non-aqueous CO2 fluid inclusions in the auriferous veins of Bin Yauri, northwestern Nigeria: Mineralium Deposita, v. 27, p. 249–255.

Goldfarb, R. J., and Groves, D. I., 2015, Orogenic gold: Common or evolving fluid and metal sources through time: Lithos, v. 233, p. 2–26.

Goldfarb, R. J., Groves, D. I., and Gardoll, S., 2001, Orogenic gold and geologic time: a global synthesis: Ore Geology Reviews, v. 18, p. 1–75.

Groves, D. I., Goldfarb, R. J., Gebre-Mariam, M., Hagemann, S. G., and Robert, F., 1998, Orogenic gold deposits: A proposed classification in the context of their crustal distribution and relationship to other gold deposit types D.I.: Ore Geology Reviews, v. 13, p. 7–27.

Hansen, G. E., 2013,Geochemical Studies of Gold Mineralizing Events In the Discovery-Ormsby and Clan Lake Areas of the Yellowknife Greenstone Belt, Northwest Territories, Canada.

Hauser, R. L., Mcdonald, D. W., and Siddorn, J. P., 2006, Geology of the Miramar Con Mine, in Gold in the Yellowknife Greenstone Belt, Northwest Territories: Results of the EXTECH III Multidisciplinary Research Project:, p. 173–187.

van Hees, E. H., Shelton, K. L., McMenamy, T. A., Ross, L. M., Cousens, B., Falck, H., Robb, M. E., and Canam, T. W., 1999, Metasedimentary influence on metavolcanic-rock-hosted greenstone gold deposits: Geochemistry of the Giant mine, Yellowknife, Northwest Territories, Canada: Geology, v. 27, p. 71–74.

van Hees, E. H., Sirbescu, M. C., Washington, G. D., and Benda, K. J., 2006a, Genesis of the Ptarmigan gold deposit: Is it of magmatic affinity?, in Gold in the Yellowknife Greenstone Belt, Northwest Territories: Results of the EXTECH III Multidisciplinary Research Project.:

van Hees, E. H., Kirkham, G., Sirbescu, M.-L., Shelton, K. L., Hauser, R. L., and Falck, H., 2006b, Large Lithogeochemical Alteration Halos Around Yellowknife Gold Deposits and Implications for Fluid Pathways; Chapter 19, in Gold in the Yellowknife Greenstone Belt, Northwest Territories: Results of the EXTECH III Multidisciplinary Research Project.:

Helmstaedt, H., and Padgham, W. A., 1986, A new look at the stratigraphy of the Yellowknife supergroup at Yellowknife, N.W.T. - implications for the age of gold-bearing shear zones and Archean basin evolution.: Canadian Journal of Earth Sciences, v. 23, p. 454–475.

Henderson, J. B., 1970, Stratigraphy of the Archean Yellowknife Supergroup, Yellowknife Bay - Prosperous Lake Area, District of Mackenzie: GSC Paper 70-26, p. 70–26.

Hollister, L. S., 1988, On the origin of CO2-rich fluid inclusions in migmatites: Journal of Metamorphic Geology, v. 6, p. 467–474.

Huizenga, J., 2001, Thermodynamic modelling of C – O – H fluids: Lithos, v. 55, p. 101–114.

Huizenga, J. M., 2011, Thermodynamic modelling of a cooling C-O-H fluid-graphite system: Implications for hydrothermal graphite precipitation: Mineralium Deposita, v. 46, p. 23–33.

Isachsen, C. E., and Bowring, S. A., 1997, The Bell Lake group and Anton Complex: a basement – cover sequence beneath the Archean Yellowknife greenstone belt revealed and implicated in greenstone belt formation: Canadian Journal of Earth Sciences, v. 34, p. 169–189.

Isachsen, C. E., Bowring, S. A., and Padgham, W. A., 1991, U-Pb zircon geochronology of the Yellowknife volcanic belt, NWT, Canada: New constraints on the timing and duration of greenstone belt magmatism: Journal of Geology, v. 99, p. 55–69.

Johnson, E. L., and Hollister, L. S., 1995, Syndeformational fluid trapping in quartz: determining the pressure-temperature conditions of deformation from fluid inclusions and the formation of pure CO2 fluid inclusions during grain-boundary migration: Journal of Metamorphic Geology, v. 13, p. 239–249.

Kirilova, M., Toy, V.G., Timms, N., Halfpenny, A., Menzies, C., Craw, D., Beyssac, O., Sutherland, R., Townend, J., Boulton, C., Carpenter, B.M., Cooper, A., Grieve, J., Little, T., Morales, L., Morgan, C., Mori, H., Sauer, K.M., Schleicher, A.M., Williams, J., Craw, L., 2017. Textural change of graphitic carbon by tectonic and hydrothermal processes in an active plate boundary fault zone, Alpine Fault, New Zealand. In: Gessner, K., Blenkinsop, T.G., Sorjonen-Ward, P. (Eds.), Characterization of OreForming Systems from Geological. Geochemical and Geophysical Studies 453 Geol. Soc., London, Spec. Publ.

Klemd, R., 1998, Comment on the paper by Schmidt Mumm et al. High CO 2 content of fluid inclusions in gold mineralisations in the Ashanti Belt, Ghana: a new category of ore forming fluids? (Mineralium Deposita 32: 107-118, 1997): Mineralium Deposita, v. 33, p. 317–319.

Klemd, R., and Hirdes, W., 1997, Origin of an unusual fluid composition in early proterozoic palaeoplacer and lodegold deposits in birimian greenstone terranes of West Africa: South African Journal of Geology, v. 100, p. 405–414.

Lahfid, A., Beyssac, O., Deville, E., Negro, F., Chopin, C., and Goffé, B., 2010, Evolution of the Raman spectrum of carbonaceous material in low-grade metasediments of the Glarus Alps (Switzerland): Terra Nova, v. 22, p. 354–360.

Landtwing, M. R., Furrer, C., Redmond, P. B., Pettke, T., Guillong, M., and Heinrich, C. A., 2010, The Bingham Canyon porphyry Cu-Mo-Au deposit. III. Zoned copper-gold ore deposition by magmatic vapor expansion: Economic Geology, v. 105, p. 91–118.

Lecumberri-Sanchez, P., Steele-MacInnis, M., and Kontak, D. J., 2021, Fluid and Melt Inclusions: Applications to Geologic Processes, in GAC-MAC meeting.:

Li, X. H., Klyukin, Y. I., Steele-MacInnis, M., Fan, H. R., Yang, K. F., and Zoheir, B., 2020, Phase equilibria, thermodynamic properties, and solubility of quartz in saline-aqueous-carbonic fluids: Application to orogenic and intrusion-related gold deposits: Geochimica et Cosmochimica Acta, v. 283, p. 201–221.

Luque, F. J., Pasteris, J. D., Wopenka, B., Rodas, M., and Barrenecha, J. F., 1998, Natural fluid-deposited graphite: mineralogical characteristics and mechanisms of formation: American Journal of Science, v. 298, p. 471–498.

Luque, F. J., Huizenga, J. M., Crespo-Feo, E., Wada, H., Ortega, L., and Barrenechea, J. F., 2014, Vein graphite deposits: Geological settings, origin, and economic significance: Mineralium Deposita, v. 49, p. 261–277.

Mavrogenes, J. A., Bodnar, R. J., Graney, J. R., McQueen, K. G., and Burlinson, K., 1995, Comparison of decrepitation, microthermometric and compositional characteristics of fluid inclusions in barren and auriferous mesothermal quartz veins of the Cowra Creek Gold District, New South Wales, Australia: Journal of Geochemical Exploration, v. 54, p. 167–175.

Newton, R. C., 1995, Simple-system mineral reactions and high-grade metamorphic fluids: European Journal of Mineral, v. 7, p. 861–881.

Ohmoto, H., and Kerrick, D., 1977, Devolatilization equilibria in graphitic systems. Am. J. Sci. 277, 1031–1044.: American Journal of Science, v. 277, p. 1031–1044.

Ootes, L., Lentz, D. R., Cabri, L. J., and Hall, D. C., 2006, Geology and gold mineralization in the Crestaurum Mine Area , northern Yellowknife greenstone belt, NWT, in Gold in the Yellowknife Greenstone Belt, Northwest Territories: Results of the EXTECH III Multidisciplinary Research Project:, p. 249–269.

Ootes, L., Lentz, D. R., Creaser, R. A., Ketchum, J. W. F., and Falck, H., 2007, Re-Os Molybdenite Ages From the Archean Yellowknife Greenstone Belt: Comparison to U-Pb Ages and Evidence for Metal Introduction at ~2675 Ma: Economic Geology, v. 102, p. 511–518.

Ootes, L., Davis, W. J., Bleeker, W., and Jackson, V. A., 2009, Two distinct ages of neoarchean turbidites in the Western Slave craton: Further evidence and implications for a possible back-arc model: Journal of Geology, v. 117, p. 15–36.

Ootes, L., Morelli, R. M., Lentz, D. R., Falck, H., Creaser, R. A., and Davis, W. J., 2011, The timing of Yellowknife gold mineralization: A temporal relationship with crustal anatexis? Economic Geology, v. 106, p. 713–720.

Pehrsson, S. J., and Villeneuve, M. E., 1999, Deposition and imbrication of a 2670–2629 Ma supracrustal sequence in the Indin Lake area, southwestern Slave province, Canada: Canadian Journal of Earth Sciences, v. 36, p. 1149–1168.

Phillips, G. N., 2013, Australian and global setting for gold in 2013, in Proceedings world gold 2013, Brisbane, Australia, 26–29 September, 2013:, p. 15–21.

Phillips, G. N., and Powell, R., 2010, Formation of gold deposits-a metamorphic devolatilization model: Journal of Metamorphic Geology, v. 28, p. 689–718.

Pratico, V., 2009, Report on the Resource Estimate of the Yellowknife Gold Project. Report Filing: NTS 85P/4 & 85P/5.:

Rahl, J. M., Anderson, K. M., Brandon, M. T., and Fassoulas, C., 2005, Raman spectroscopic carbonaceous material thermometry of low-grade metamorphic rocks: Calibration and application to tectonic exhumation in Crete, Greece: Earth and Planetary Science Letters, v. 240, p. 339–354.

Ridley, J. W., and Diamond, L. W., 2000, Fluid Chemistry of Orogenic Lode Gold Deposits and Implications for Genetic Models: Reviews in Economic Geology, v. 13, p. 141–162.

Roberts, S., Beattie, I., 1995. Micro-Raman spectroscopy in the earth sciences. In: Microprobe Techniques in the Earth Sciences. Chapman & Hall, London, pp. 387–408.

Roedder, E., 1970, Application of an improved crushing microscope stage to studies of the gases in fluid inclusions.pdf: Schweizerische Mineralogische und Petrographische Mitteilungen, v. 50/1, p. 41–58.

Roedder, E., 1984, Fluid inclusions: Roedder, E., v. 12, p. 644.

Rosso, K. M., and Bodnar, R. J., 1995, Microthermometric and Raman spectroscopic detection limits of C02 in fluid inclusions and the Raman spectroscopic characterization of C02: Geochimica et Cosmochimica Acta, v. 59, p. 3961–3975.

Santosh, M., and Wada, H., 1993, A carbon isotope study of graphites from the Kerela Khondalite Belt, Southern India: Evidence for CO2 infiltration in granulites: Journal of Geology, v. 101, p. 643–651.

Schmidt-Mumm, A., Oberthur, T., Vetter, U., and Blenkinsop, T. G., 1997, High CO2 content of fluid inclusions in gold mineralizations in the Ashanti belt, Ghana: a new category of ore forming fluids: Mineralium Deposita, v. 32, p. 107–118.

Shelton, K. L., McMenamy, T. A., van Hees, E. H., and Falck, H., 2004, Deciphering the complex fluid history of a greenstone-hosted gold deposit: Fluid inclusion and stable isotope studies of the Giant mine, Yellowknife, Northwest Territories, Canada: Economic Geology, v. 99, p. 1643–1663.

Shelton, K. L., Smith, A. D., Hill, L., and Falck, H., 2016, Ore petrography, fluid inclusion and stable isotope studies of gold and basemetal sulphide mineralization in a northern portion of the Yellowknife greenstone belt: Northwest Territories Geological Survey NWT Open File 2016-02, p. 38.

Siddorn, J. P., Cruden, A. R., Hauser, R. L., Armstrong, J. P., and Kirkham, G., 2006, The Giant-Con gold deposits: Preliminary integrated structural and mineralization history, in Gold in the Yellowknife Greenstone Belt, Northwest Territories: Results of the EXTECH III Multidisciplinary Research Project:, p. 213–231.

Silke, R., 2009, The Operational History of Mines in the Northwest Territories, Canada

Stubley, M.P. and Irwin, D., 2019. Bedrock Geology of the Slave Craton, Northwest Territories and Nunavut; Northwest Territories Geological Survey, NWT Open File 2019-01, ESRI® and Adobe® digital files.

Thompson, P. H., 2006, Metamorphic constraints on the geological setting, thermal regime, and timing of alteration and gold mineralization in the Yellowknife greenstone belt, NWT, Canada, in Gold in the Yellowknife Greenstone Belt, Northwest Territories: Results of the EXTECH III Multidisciplinary Research Project:, p. 142–172.

Voisey, C. R., Tomkins, A. G., and Xing, Y., 2020, Analysis of a Telescoped Orogenic Gold System: Insights from the Fosterville Deposit: Economic Geology, v. 115, p. 1645–1664.

White, A. J. R., Waters, D. J., and Robb, L. J., 2013, The application of P–T–X(CO2) modelling in constrainingmetamorphism and hydrothermal alteration at the Damang gold deposit, Ghana: Journal of Metamorphic Geology, v. 31, p. 937–961.

Yamashita, K., and Creaser, R. A., 1999, Geochemical and Nd isotopic constraints for the origin of Late Archean turbidites from the Yellowknife area, Northwest Territories, Canada: Geochimica et Cosmochimica Acta, v. 63, p. 2579–2598.

Zhang, H., and Zhu, Y., 2019, Mechanism of gold precipitation in the Gezigou gold deposit, Xinjiang, NW China: Evidence from fluid inclusions and thermodynamic modeling: Journal of Geochemical Exploration, v. 199, p. 60–74.

Zoheir, B., Steele-MacInnis, M., and Garbe-Schönberg, D., 2019, Orogenic gold formation in an evolving, decompressing hydrothermal system: Genesis of the Samut gold deposit, Eastern Desert, Egypt: Ore Geology Reviews, v. 105, p. 236–257.

APPENDIX A

Location, metal content, and host lithology of the collected vein samples from the Quyta-Bell property.

Sample No	Easting (m)	Northing (m)	Host Formation/Group	Host Lithology	Strike	Dip	Au (ppm)	Ag (ppm)	Cu (ppm)	Pb (ppm)	Zn (ppm)	As (ppm)	Bi (ppm)	Sb (ppm)	W (ppm)	Zn (ppm)
X412751	645833.00	6981586.00	Burwash	Greywacke	244	39	-	-	-	-	-	-	-	-	-	-
X412752	646233.00	6982200.00	Burwash	Mafic Volcanic Flow	16	85	-	-	-	-	-	-	-	-	-	-
X412753	640683.00	6984824.00	Banting	Intermediate Volcanic Flow	267	76	-	-	-	-	-	-	-	-	-	-
X412754	638096.00	6969789.00	Kam	Mafic Volcanic Flow	90	90	-	-	-	-	-	-	-	-	-	-
X412755	638027.00	6969630.00	Kam	Ankerite Vein			-	-	-	-	-	-	-	-	-	-
X412756	634369.00	6980228.00	Burwash	Greywacke	92	45	-	-	-	-	-	-	-	-	-	-
X412757	634360.00	6980232.00	Burwash	Greywacke	120	48	-	-	-	-	-	-	-	-	-	-
X412758	637683.00	6984157.00	Burwash	Quartz Vein	170		0.026	0.25	18	18	50	54	-2	7	-10	50
X412759	642342.00	6971952.00	Burwash	Quartz Vein	35	88	0.005	0.25	29	6	91	9	-2	-5	-10	91
X412760	642234.00	6972005.00	Burwash	Quartz Vein	15		0.005	0.25	29	4	64	13	-2	-5	-10	64
X412761	641979.00	6971549.00	Burwash	Quartz Vein	175	57	0.0025	0.25	4	1	7	2.5	-2	-5	-10	7
X412762	633965.67	6980055.78	Burwash	Quartz Vein	315	75	0.125	0.25	18	1	80	5510	3	-5	-10	80
X412763	634021.73	6979677.08	Burwash	Quartz Vein	323	73	2.05	0.7	9220	1	4	18	11	-5	-10	4
X412764	634252.31	6980263.97	Burwash	Quartz Vein			0.034	0.25	55	17	57	222	-2	-5	-10	57
X412765	637439.66	6965286.34	Burwash	Quartz Vein			0.074	0.25	5	9	6	91	5	-5	-10	6
X412766	637590.03	6965402.95	Burwash	Intermediate Volcaniclastic Rock	35	86	0.014	0.25	43	4	97	130	-2	-5	-10	97
X412767	636660.18	6971590.63	Kam	Quartz Vein	338	82	0.0025	0.25	43	1	18	2.5	-2	-5	-10	18
X412768	636744.06	6971872.98	Kam	Mafic Volcanic Flow	176	85	0.0025	0.25	48	48	194	2.5	-2	-5	-10	194
X412769	636795.72	6971894.32	Kam	Quartz Vein	168	84	0.717	9.7	1540	41	235	12	55	-5	10	235
X412770	636860.39	6971899.36	Kam	Quartz Vein	162	75	0.0025	0.25	98	11	59	2.5	-2	-5	-10	59
X412771	636933.96	6972037.51	Kam	Quartz Vein			0.007	0.25	13	1	2	2.5	-2	-5	-10	2
X412772	640615.00	6984008.00	Banting	Quartz Vein	50		2.46	0.5	47	15	87	2.5	-2	-5	10	87
X412773	646840.00	6983229.00	Burwash	Mudstone	27	68	0.005	0.25	130	7	76	6	-2	-5	-10	76
X412774	646822.00	6983221.00	Burwash	Mudstone	35	73	0.094	0.25	41	2	47	25	-2	-5	10	47
X412775	646843.00	6983138.00	Burwash	Mafic Volcanic Flow			0.0025	0.25	89	6	78	2.5	-2	-5	-10	78
X412776	637554.48	6983402.94	Burwash	Mudstone			6.07	20.2	19	1015	353	98200	14	89	-10	353
X412777	642287.51	6972006.66	Burwash	Sandstone	30	64	0.016	0.25	41	8	42	12	-2	5	100	42
X412778	639893.10	6970025.24	Burwash	Sandstone	4	72	0.0025	0.25	12	6	59	34	-2	-5	-10	59
X412779	637516.25	6965324.04	Burwash	Intermediate Volcaniclastic Rock	65		0.06	0.25	485	8	16	70	-2	-5	-10	16
X412780	637566.63	6965393.97	Burwash	Intermediate Volcaniclastic Rock	240		0.02	0.25	178	4	43	223	-2	-5	-10	43
X412781	637696.00	6965572.00	Burwash	Intermediate Volcaniclastic Rock	19		0.014	0.25	51	8	25	185	-2	-5	-10	25
X412782	637111.07	6972101.39	Kam	Gabbro	279		0.231	1.8	116	469	244	25	-2	-5	-10	244

APPENDIX B

Fluid inclusion petrography – Giant Mine

Sample No:	Type 1 (aqueous)		Type 2 (carbonic)		Type 3 (Saline)	Type 4 (aqueous-carbonic)	Size	Abundancy	Distribution
3A							Not visible		
7A	Common	Mostly two phased (<20% V)	Rare	Mostly single phased			Small (<5 µm)	Abundant	
10B	Scarce	Mostly two phased	Common	Mostly single phased			Small (<5 µm)	Abundant	Primary
10C			Common	Mostly single phased			Small (<5 µm)	Abundant	
12B	Very few quartz						Small (<5 µm)	Very few	
13A			Common	Mostly single phased			Small (<5 µm)	Few	
13E							Small (<5 µm)	Few	
14E			Common	Mostly single phased			Medium (5-10 µm)	Abundant	
15A			Common	Mostly single phased			Small (<5 µm)	Medium	
18A	Common	Mostly two phased (<30% V)	Common	Mostly single phased	Rare		Medium (5-10 µm)	Abundant	Mostly secondary
18B	Common	Mostly two phased (<30% V)	Common	Both single and two phased			Medium (5-10 µm)	Abundant	Mostly secondary
19A	Common	Mostly two phased (<40% V)	Common	Both single and two phased	Rare	Rare	Medium (5-10 µm)	Abundant	Mostly secondary
20A	Common	Mostly two phased (<20% V)	Common	Both single and two phased	Scarce	Rare	Good (5-15 µm)	Abundant	Both primary and
21A	Common	Mostly two phased (<40% V)	Common	Mostly single phased			Medium (5-10 µm)	Abundant	
7005	Very few quartz						Not visible		
7006A	Very few quartz		Common	Mostly single phased			Small (<5 µm)	Few	
7018B			Common	Mostly single phased			Small (<5 µm)	Abundant	
11889B	Very few quartz		Common	Mostly single phased			Small (<5 µm)	Few	Mostly primary
11892			Common	Mostly single phased			Medium (5-10 µm)	Abundant	Mostly primary
11893			Common	Mostly single phased			Small (<5 µm)	Abundant	Mostly primary
11894A			Common	Mostly single phased			Medium (5-10 µm)	Medium	
11895	Very few quartz		Common	Mostly single phased			Small (<5 µm)	Few	
11897	Common	Mostly two phased (<20% V)	Scarce	Mostly single phased			Medium (5-10 µm)	Medium	
11900			Common	Mostly single phased	Rare		Medium (5-10 µm)	Medium	
61014			Common	Mostly single phased			Medium (5-10 µm)	Abundant	Both primary and
61014-2			Common	Mostly single phased			Small (<5 µm)	Abundant	
K-1	Rare		Common	Mostly single phased			Medium (5-10 µm)	Abundant	
KS96-1	Common	Mostly two phased (<30% V)	Common	Mostly single phased			Good (5-15 µm)	Abundant	Mostly secondary
KS96-3	Common	Mostly two phased (<20% V)	Scarce	Mostly single phased			Good (5-15 µm)	Abundant	
KS96-4	Common	Mostly two phased (<30% V)	Common	Mostly single phased			Medium (5-10 µm)	Abundant	
KS96-5A			Common	Mostly single phased			Small (<5 µm)	Medium	
KS96-5B	Scarce	Mostly two phased (<20% V)	Common	Mostly single phased			Small (<5 µm)	Abundant	
KS96-6-1	Common	Mostly two phased (<30% V)	Common	Mostly single phased		Rare	Medium (5-10 µm)	Abundant	
KS96-6-2	Common	Mostly two phased (<30% V)	Common	Mostly single phased			Medium (5-10 µm)	Abundant	
KS96-8 Early	Common	Mostly two phased (<20% V)	Common	Mostly single phased			Small (<5 µm)	Abundant	Both primary and
KS96-8A	Common	Mostly two phased (<30% V)	Common	Mostly single phased			Small (<5 µm)	Abundant	Both primary and
KS96-8B	Common	Mostly two phased (<20% V)	Common	Mostly single phased			Small (<5 µm)	Abundant	
KS96-11	Very few quartz								
KS96-14B	Very few quartz								
STN5	Common	Mostly two phased (<20% V)	Scarce	Mostly single phased	Very Rare		Medium (5-10 µm)	Abundant	
Brock Vein			Common	Mostly single phased			Not visible		
Horseshoe Vein							Not visible		

Fluid inclusion components based on Raman spectroscopy – Giant Mine

Sample No	Crushing Score	Undetermined	H2O+NaCl	H2O	H2O+CO2	CO2	CH4	CO2+CH4	CO2+CH4+C
7A	1.7	10		90					
10B	2.7			10		90			
10C	2.2			10		90			
14E	2.7					100			
15A	3					100			
18A	2.3			60		10		30	
18B	2.6			40		10		50	
19A	2			70				30	
20A	3		10	10			40	20	20
21A	2.7			20				80	
7018B	2.7							90	10
11889B	1							90	10
11892								100	
11893	2.3							100	
11894A	3							100	
11895	3							70	30
11897	2.7	15		70			15		
11900	3							440	60
61014	3							60	40
K-1	3			5	15	80			
KS96-1	1.3	15		70			15		
KS96-3	1.2	10		90					
KS96-4	3			60	20	10	10		
KS96-5A	2.7			20		75	5		
KS96-6	2.8			50		50			
KS96-8A	2.7					100			
KS96-8B	3			20		80			
KS96-8 EARLY	1.7			60		30	10		
STN5	1			100					

Fluid inclusion petrography – Quyta-Bell Property

Sample No:	Type 1 (liquid dominated)		Type 2 (vapor dominated)		Type 3 (Saline)		Type 4 (aqueous-carbonic)	Size	Abundancy	Distribution
X412751	Scarce	Mostly single phased	Very Rare	Variable	Not found		Not found	Small (<5 µm)	Very Few	
X412752	Common	Mostly two phased (10-30% V)	Scarce		Common	Necking	Not found	Good (5-15 µm)	Abundant	Secondary
X412753	Common	Mostly two phased (~40% V)	Common	Mostly two phased(60-80% V)	Scarce		Scarce	Good (5-15 µm)	Abundant	Randomly distributed
X412754	Scarce	Mostly two phased (~40% V)	Common	Mostly two phased(65-80% V)	Very Rare		Not found	Small (<5 µm)	Abundant	Secondary
X412756	Common	Mostly two phased (~25% V)	Rare	Single phased	Rare		Not found	Good (5-15 µm)	Abundant	Secondary
X412757	Common	Mostly two phased (<20% V)	Rare		Rare		Rare	Good (5-15 µm)	Abundant	Secondary
X412758	Scarce	Mostly two phased (<15% V)	Common	Mostly single phased	Very Rare		Not found	Medium (5-10 µm)	Medium	
X412759	Common	Mostly two phased (<20% V)	Common	Both two phased(>75% V) and single phased	Rare		Scarce	Good (5-15 µm)	Medium	Secondary and random
X412760	Common	Two phased (<15% V)	Rare	Two phased (~70% V)	Common		Scarce	Good (5-15 µm)	Abundant	
X412761	Common	Mostly two phased (<15% V)	Common	Both two phased(70-80%V) and single phased	Very Rare	Two different solid	Very Rare	Good (5-15 µm)	Abundant	Secondary
X412762	Common	Mostly two phased (<15% V)	Scarce	Mostly two phased (> 80%V)	Not found		Not found	Good (5-15 µm)	Abundant	Secondary
X412763	Common	Mostly two phased (30-40% V)	Common	Mostly two phased (60-70% V)	Very Rare		Not found	Medium (5-10 µm)	Abundant	Primary and Pseudosecondary
X412764	Common	Mostly two phased (30-40% V)	Scarce	Mostly single phased	Rare		Rare	Good (5-15 µm)	Medium	Secondary
X412765					Not found			Not visible		
X412766	Common	Mostly two phased (<20% V)	Common	Both two phased (60-70% V) and single phased	Scarce		Not found	Medium (5-10 µm)	Medium	Randomly distributed
X412767	Rare	Mostly single phased	Rare	Mostly single phased	Not found		Not found	Small (<5 µm)	Very Few	Randomly distributed
X412768	Rare	Mostly two phased (20% V)	Common	Both two phased (<65% V) and single phased	Common	Two different solid	Scarce	Good (5-15 µm)	Medium	
X412769	Rare	Variable	Common	Both two phased (60-70%V) and single phased	Not found		Not found	Small (<5 µm)	Medium	Secondary
X412770	Scarce	Variable	Common	Mostly single phased	Rare		Not found	Good (5-15 µm)	Medium	Randomly distributed
X412771	Common	Variable	Common	Mostly single phased	Rare		Not found	Medium (5-10 µm)	Abundant	Secondary
X412772	Scarce	Mostly two phased (<20% V)	Common	Mostly single phased	Scarce		Rare	Good (5-15 µm)	Abundant	Secondary
X412773	Rare	Variable	Common	Mostly single phased	Rare		Not found	Good (5-15 µm)	Medium	Secondary
X412774	Not found		Scarce	Mostly single phased	Common		Not found	Medium (5-10 µm)	Scarce	Secondary
X412775	Rare	Mostly two phased (<15% V)	Common	Mostly single phased	Scarce		Rare	Good (5-15 µm)	Abundant	Secondary
X412776	Not found		Common	Mostly single phased	Rare		Rare	Good (5-15 µm)	Abundant	Secondary and random
X412777	Common	Mostly two phased (<15% V)	Common	Mostly two phased (>80% V)	Rare		Common	Good (5-15 µm)	Abundant	Secondary
X412778	Common	Mostly two phased (<15% V)	Common	Mostly two phased (>60% V)	Rare		Very Rare	Small (<5 µm)	Abundant	Secondary
X412779	Common	Mostly two phased (<15% V)	Scarce	Mostly single phased	Scarce		Not found	Small (<5 µm)	Abundant	Secondary
X412780	Common	Mostly two phased (<20% V)	Scarce	Mostly two phased (>60% V)	Very Rare		Not found	Small (<5 µm)	Abundant	
X412781	Common	Mostly two phased (<20% V)	Scarce	Mostly single phased	Common		Not found	Small (<5 µm)	Medium	
X412782	Scarce	Mostly two phased (<20% V)	Common	Mostly single phased	Scarce		Scarce	Medium (5-10 µm)	Medium	Secondary

Fluid inclusion components based on Raman spectroscopy – Quyta-Bell Property

Sample No:	Crushing Score	Undetermined	H_2O+NaCl	H_2O	CO_2+CH_4	C+CO_2+CH_4	H_2O+CO_2
X412753	3		20	5	40	30	5
X412757	1.7			80	10	5	5
X412758	2	10		15	60	15	
X412760	2		40	40	5		15
X412761	1.9		5	50	5		40
X412762	1	20		70	10		
X412763	1.2	15	5	80			
X412764	1.7	10		80	10		
X412768	1.6		40	10	25	10	15
X412769	2.7			5	95		
X412770	2.8		5	15	70	10	
X412771	2.1			60	30	10	
X412772	2.9		15	5	35	45	
X412773	2.3		10	10	55	20	5
X412775	3		15	5	55	25	
X412776	3		15	5	40	40	
X412777	2.9		20	10	30	30	10
X412778	1.7		35	25	40		
X412780	2	25	5	70			
X412782	2.7			10	40	20	30

APPENDIX C

Raman spectra used in graphite thermometer calculations

X412776-1

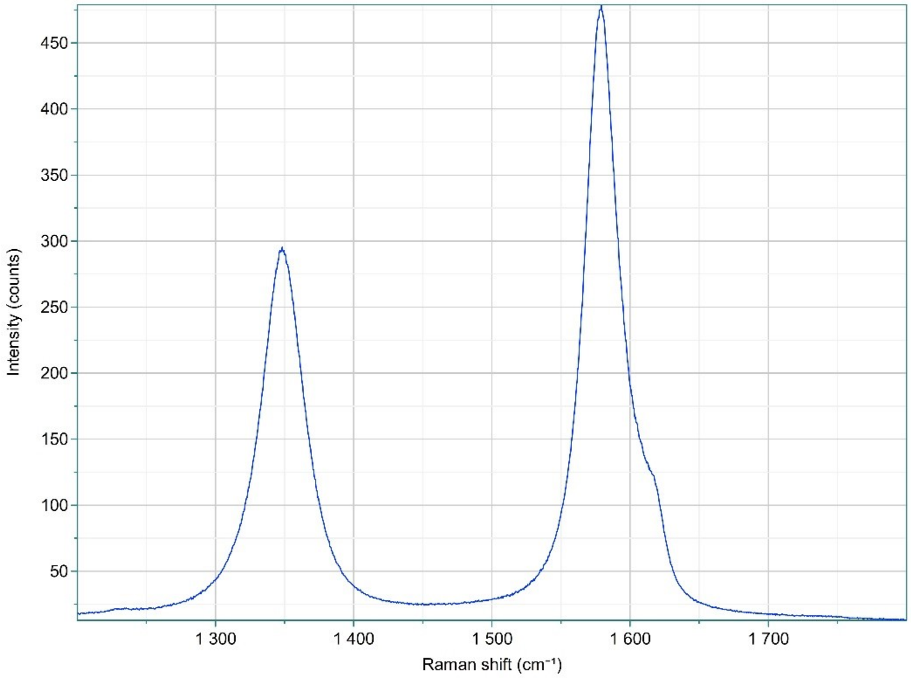

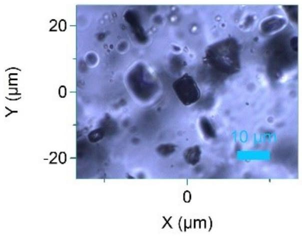

X412776-5

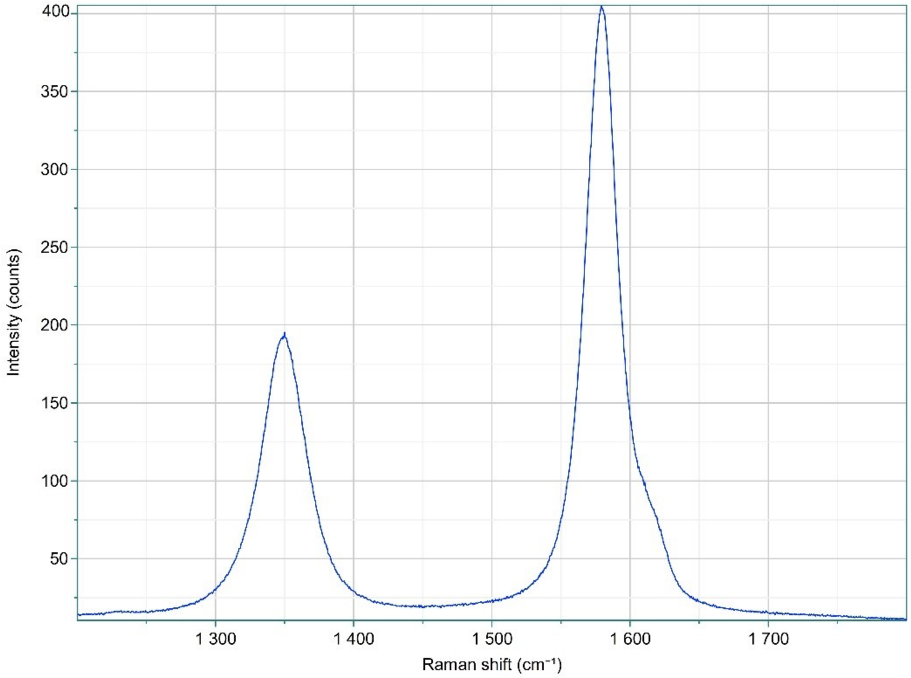

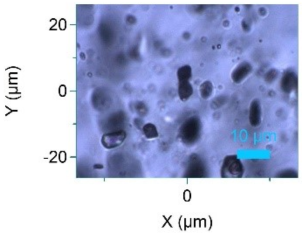

X412776-7

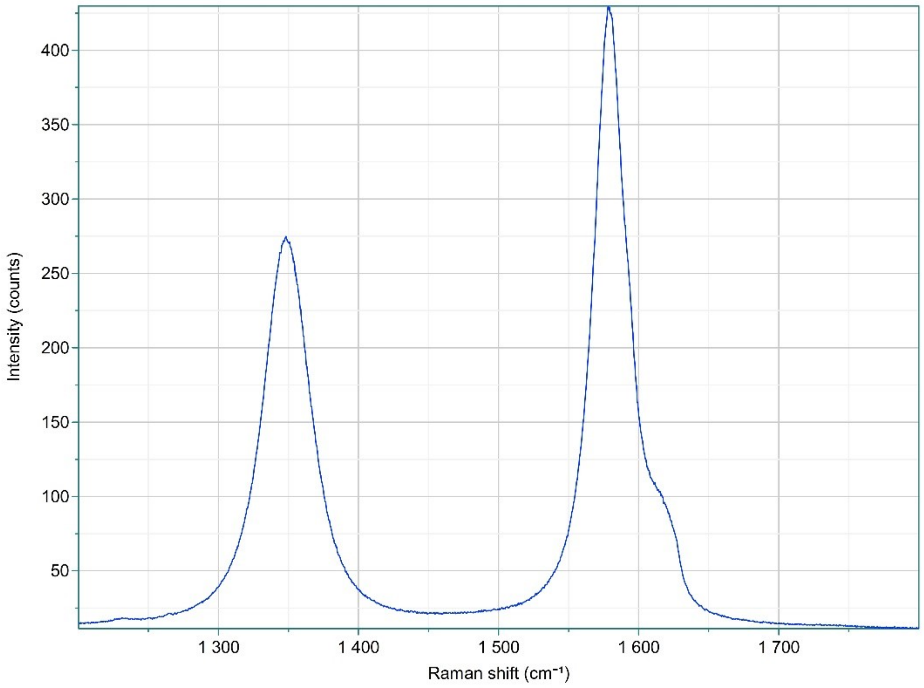

X412776-8

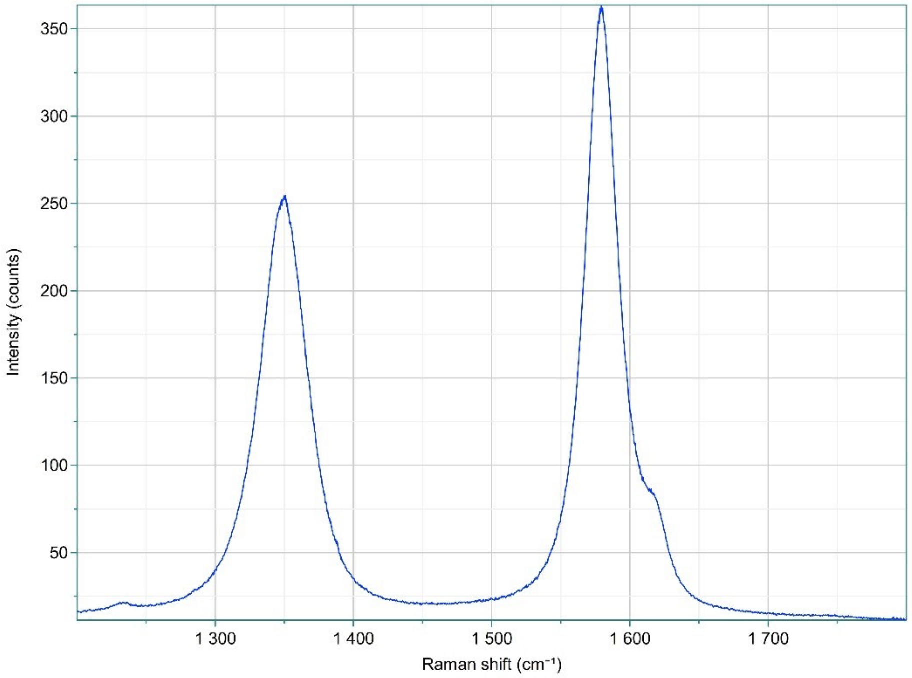

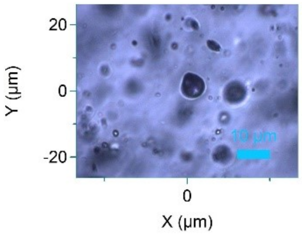

X412776-16

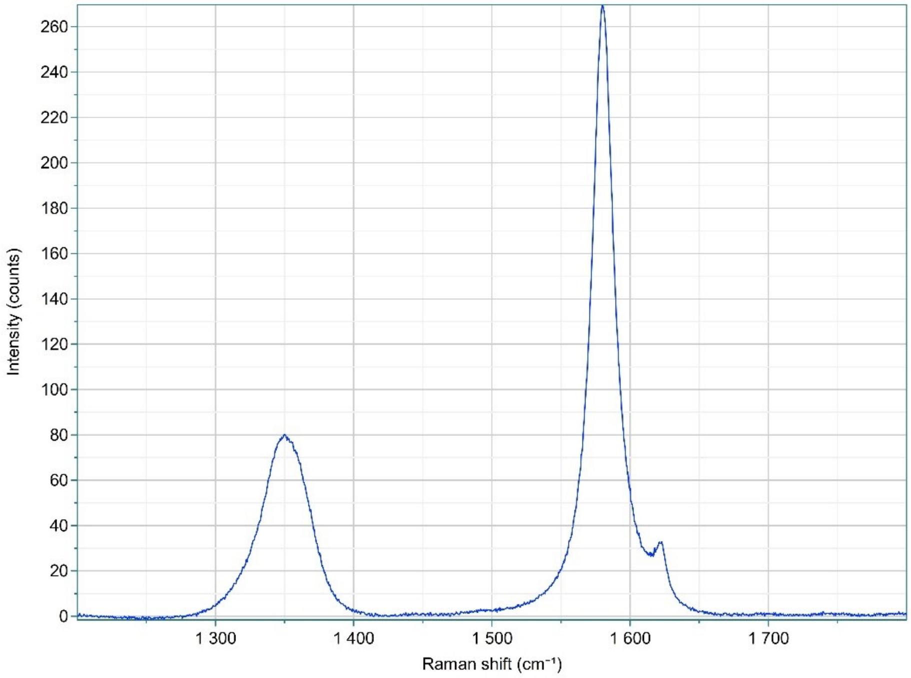

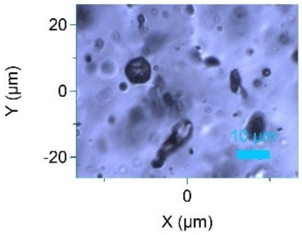

X412776-18

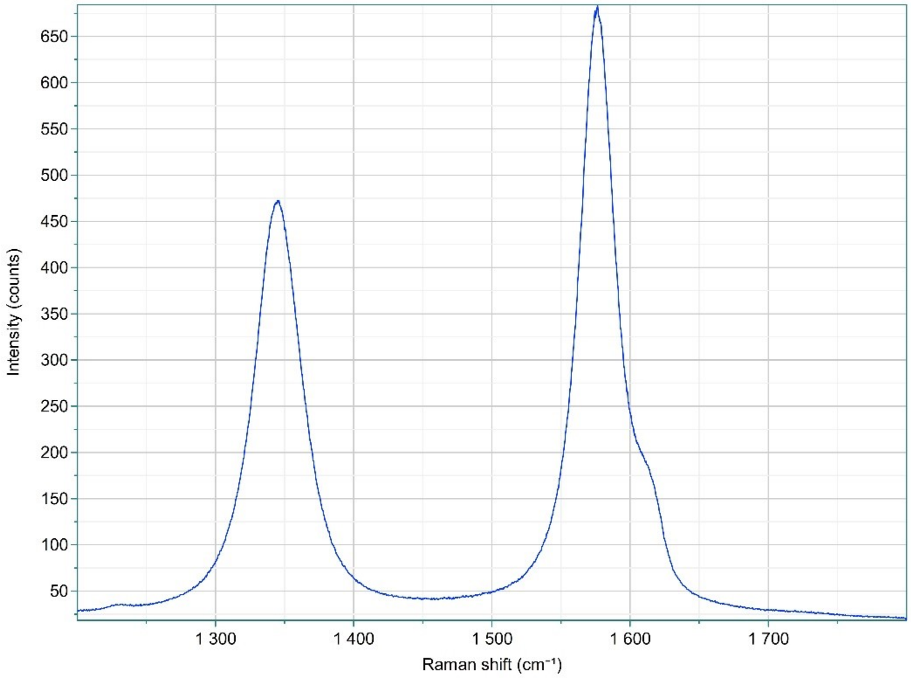

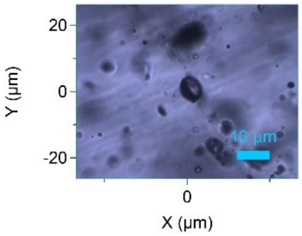

X412776-19

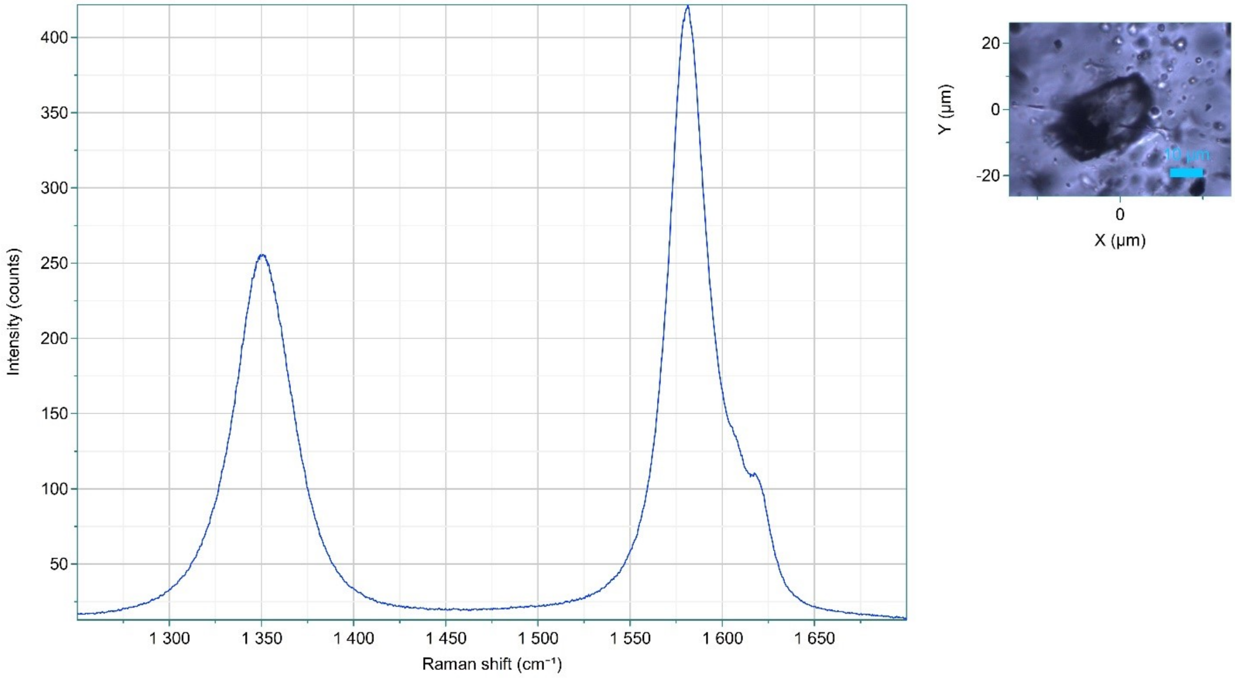

X412776-20

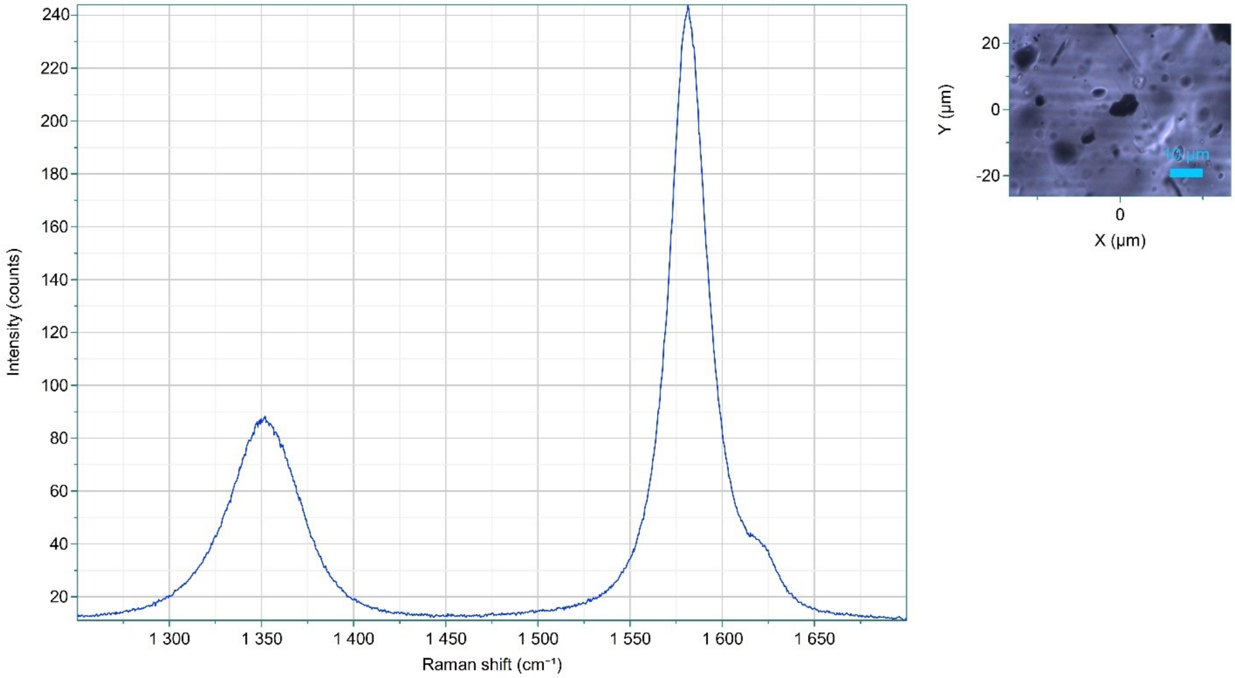

X412776-21

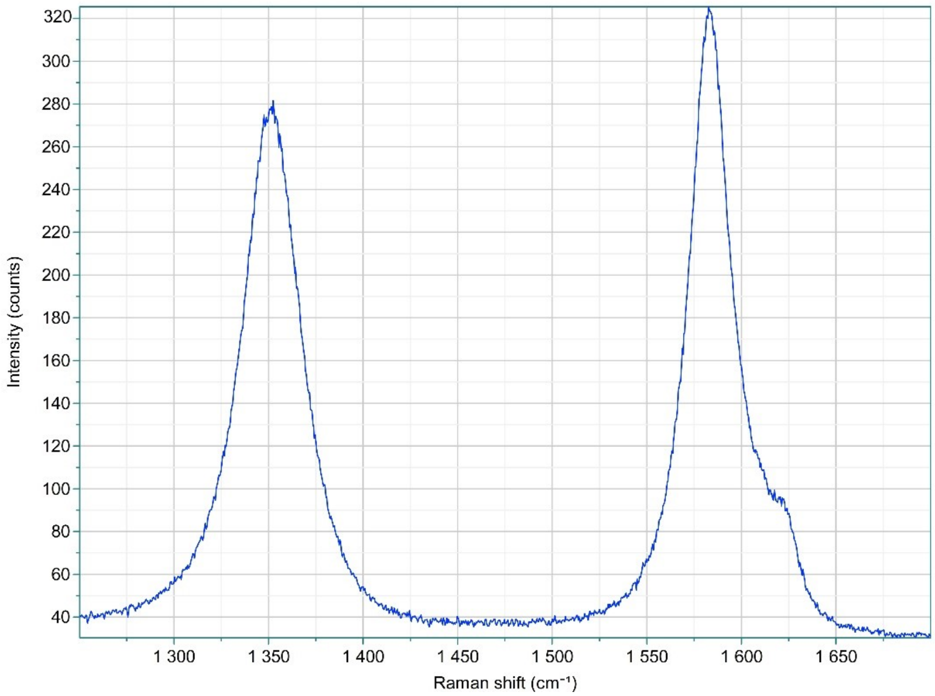

X412776-26

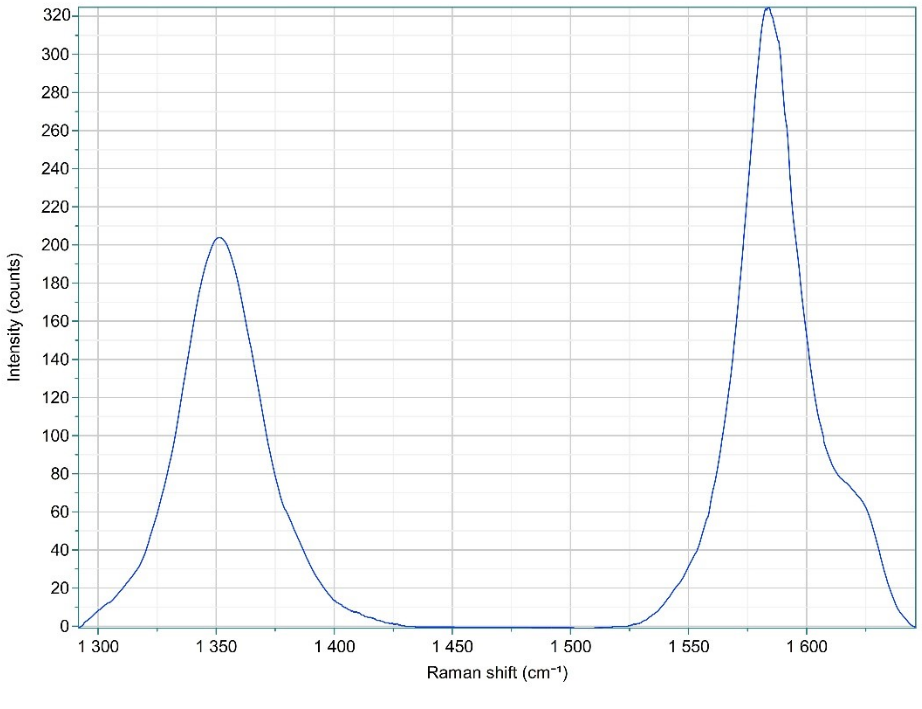

X412776-27

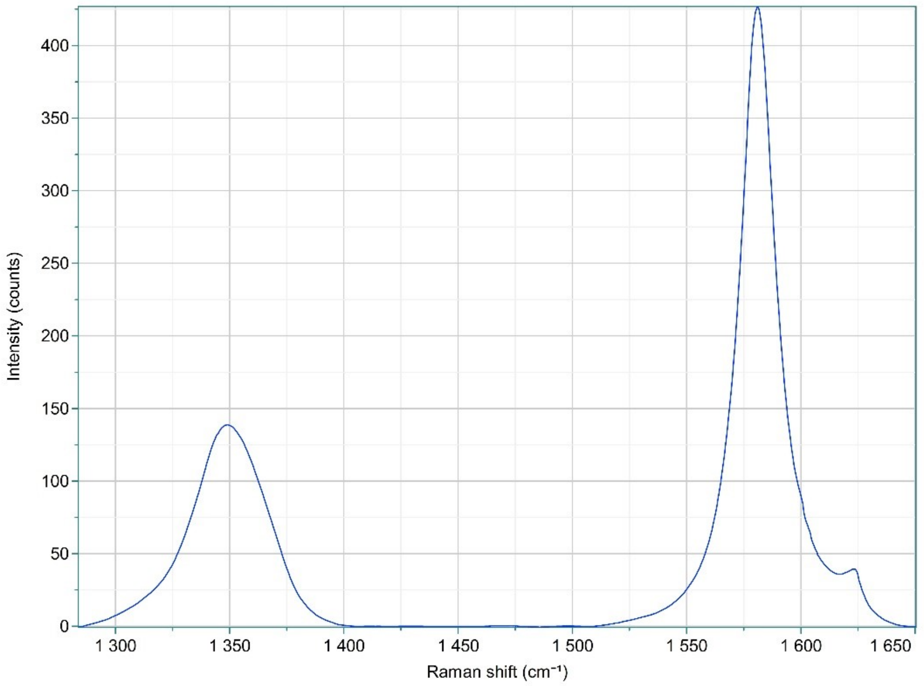

X412753-1

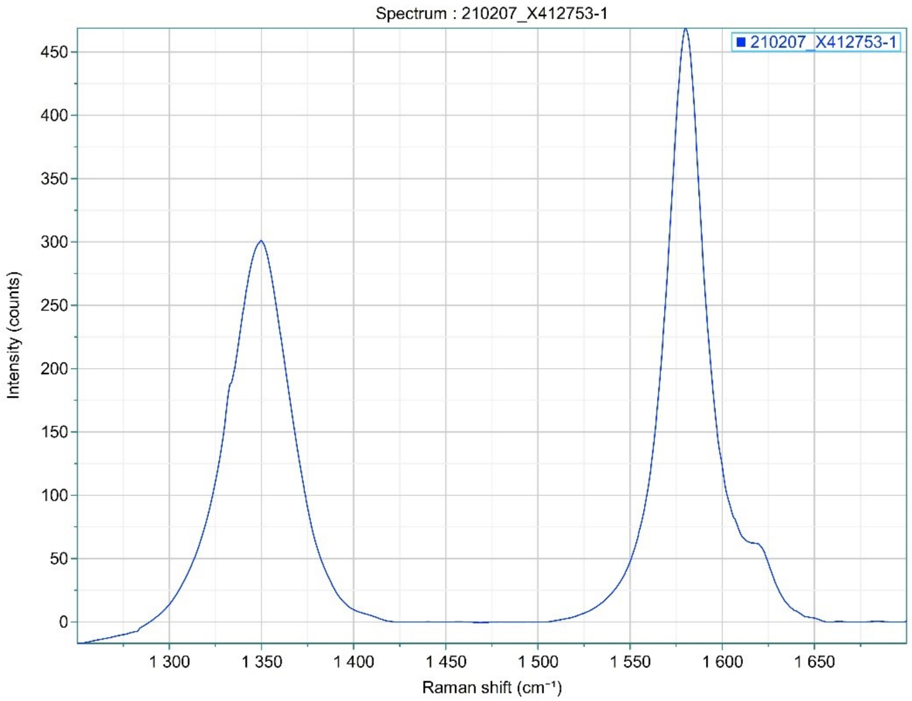

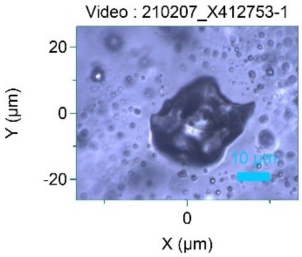

NOTES:

X412753-2

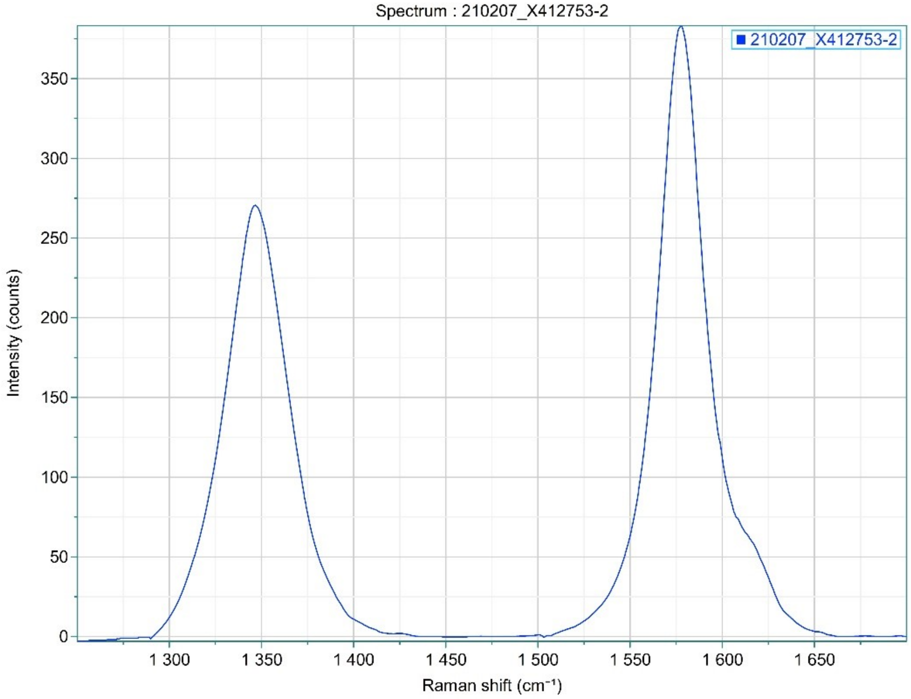

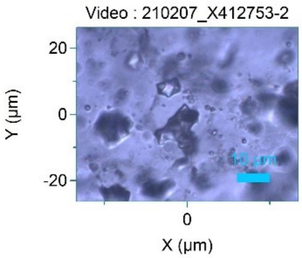

NOTES:

X412753-3

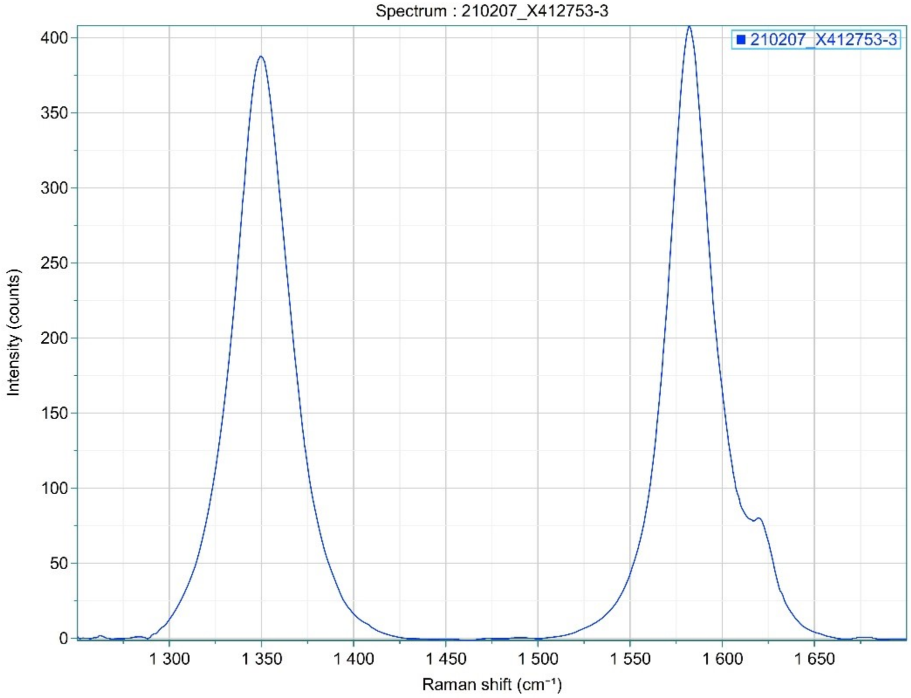

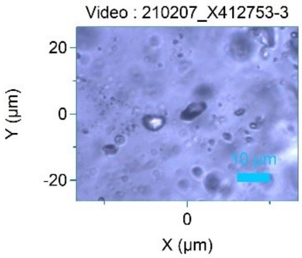

NOTES:

X412753-4

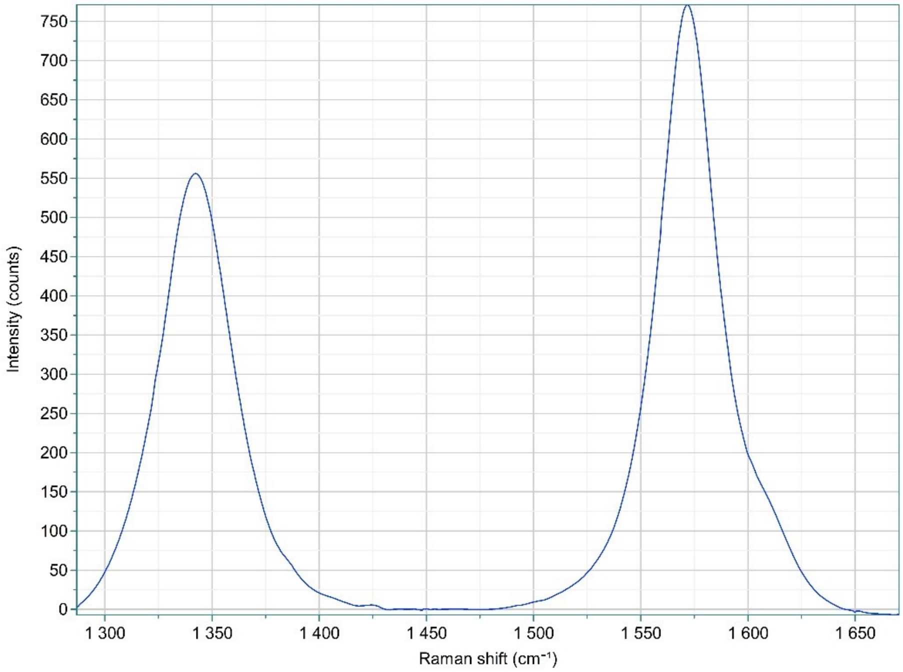

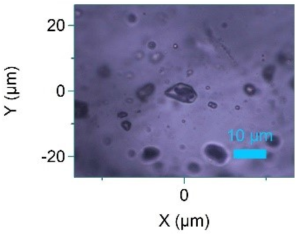

X412775-2

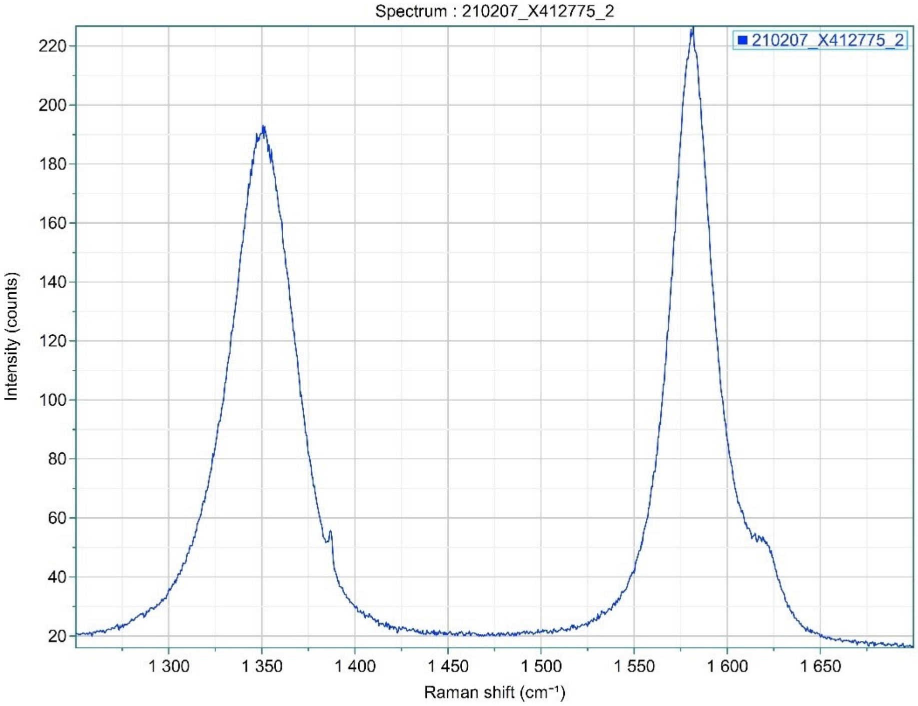

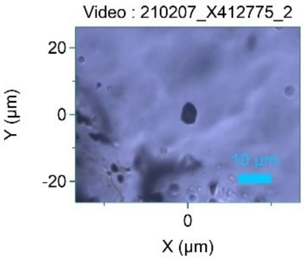

NOTES:

X412775-3

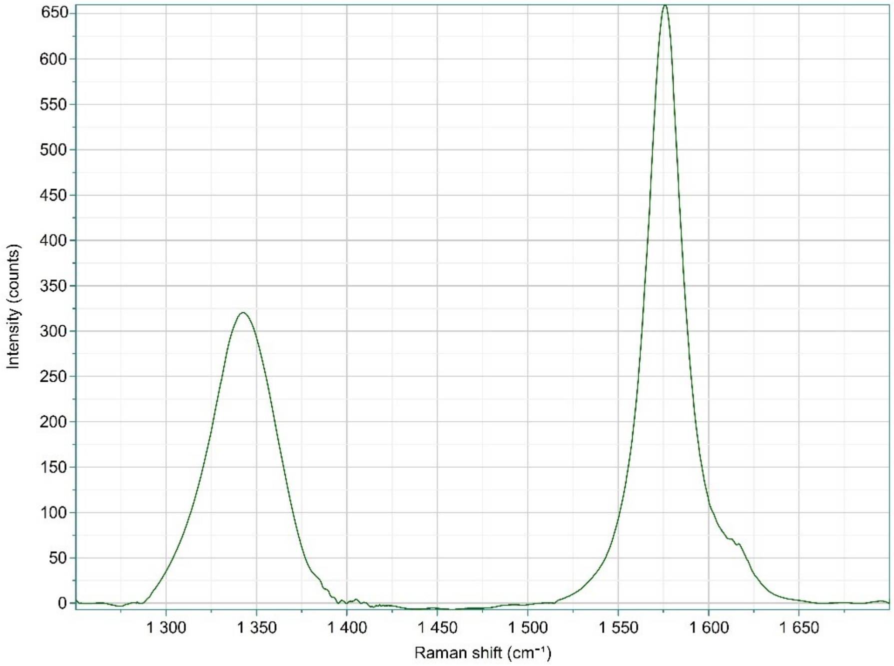

X412777-1

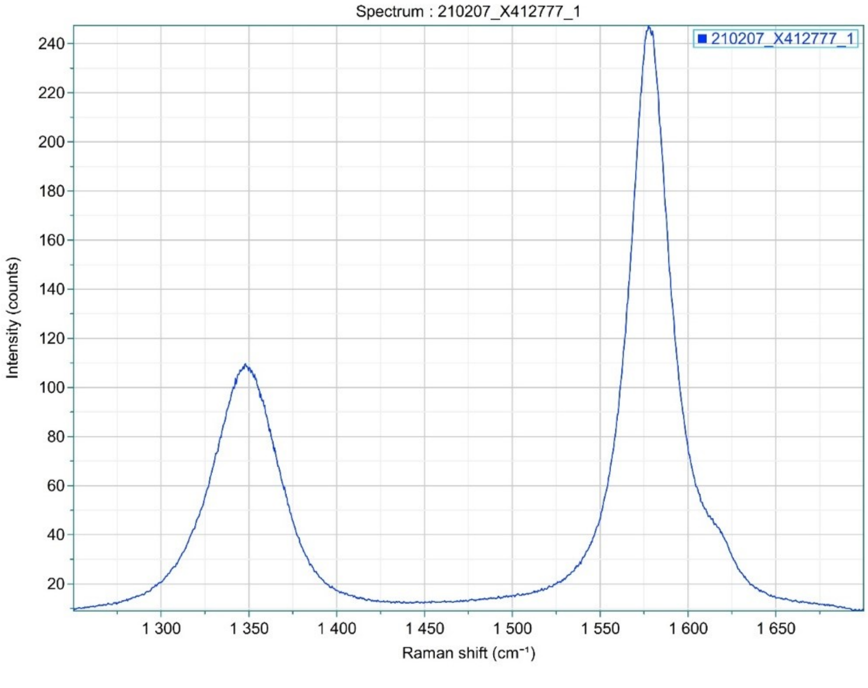

X412777-2

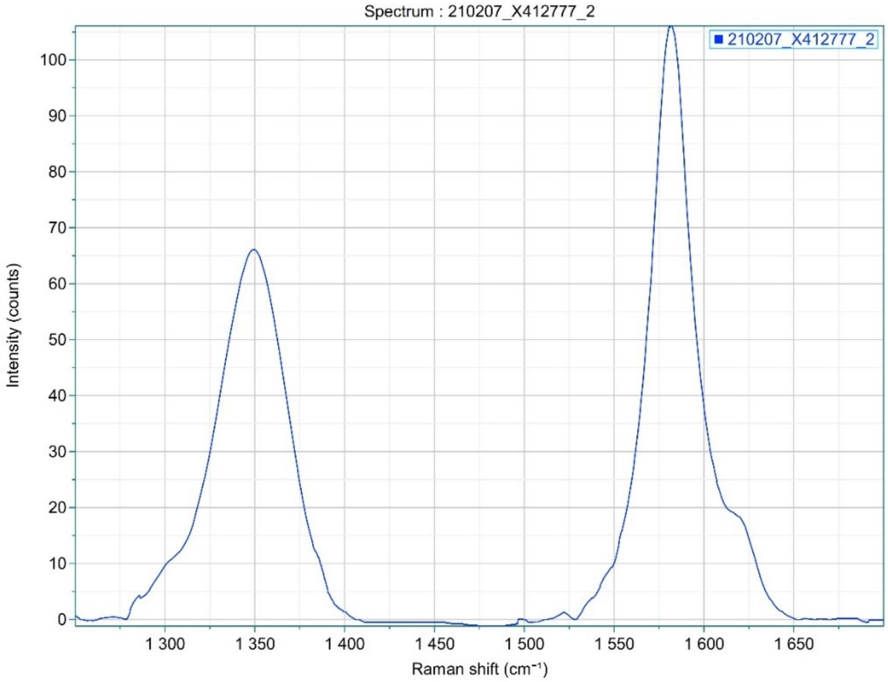

X412776-3

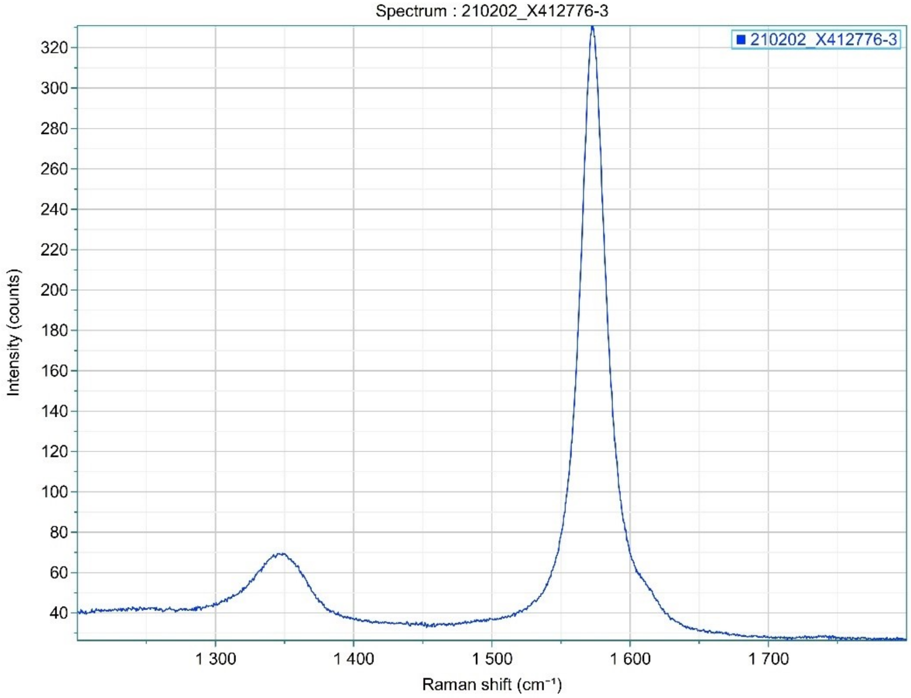

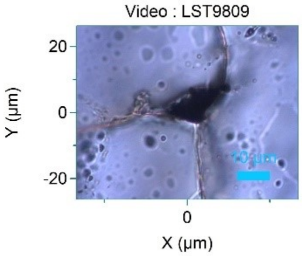

NOTES:

X412776-4

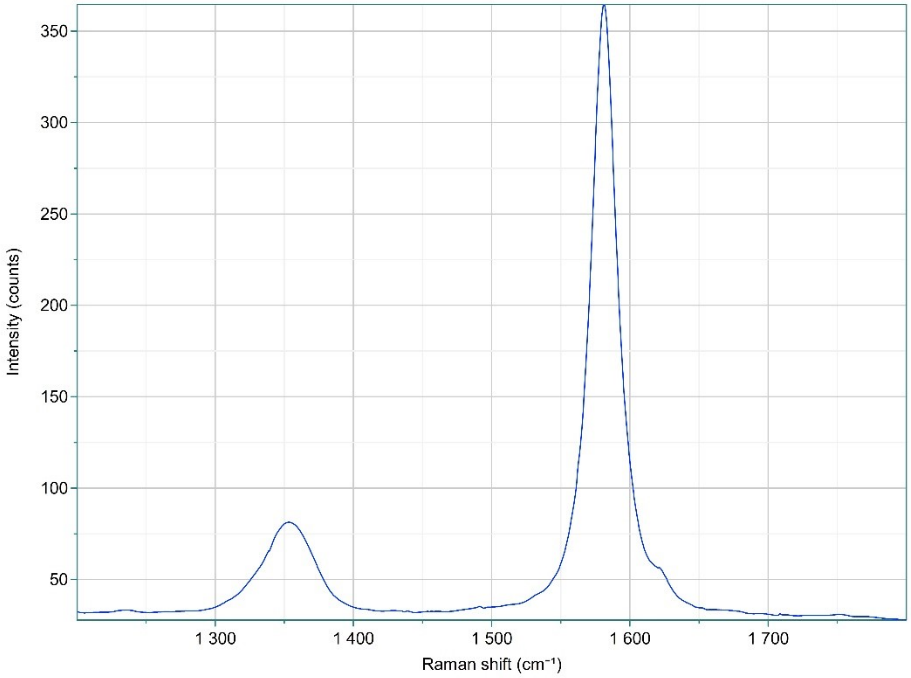

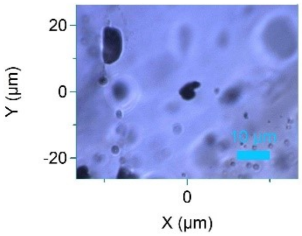

X412776-6

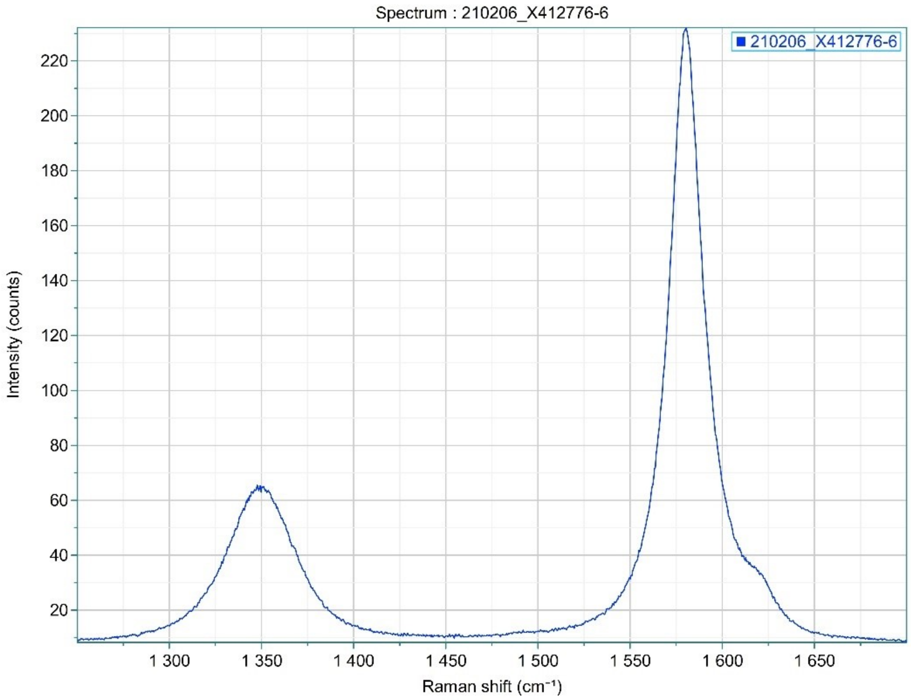

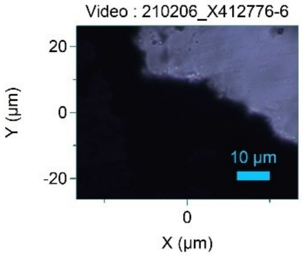

NOTES:

X412776-14

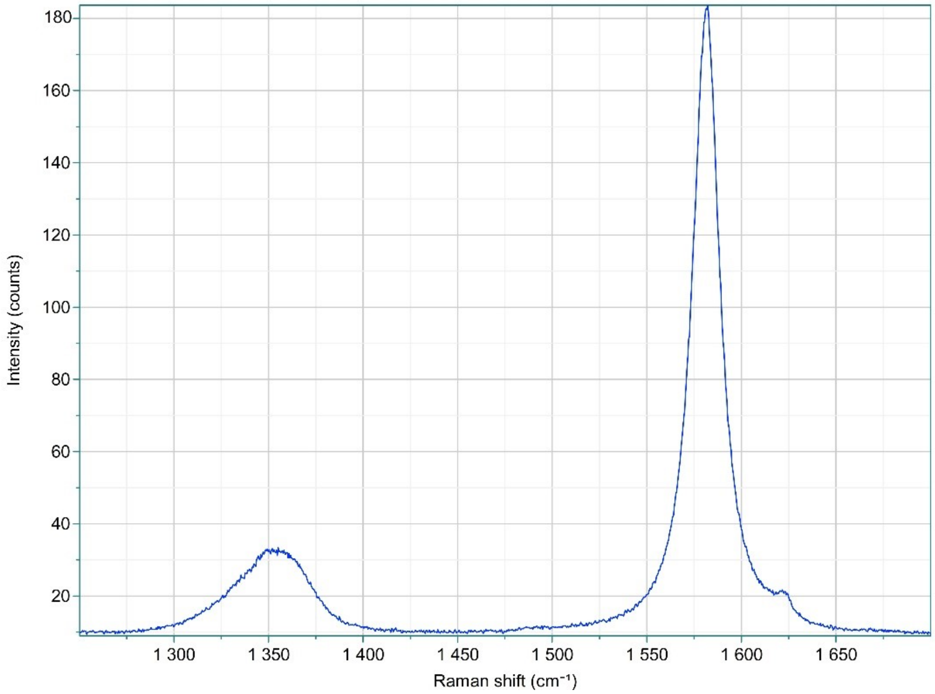

X412776-15

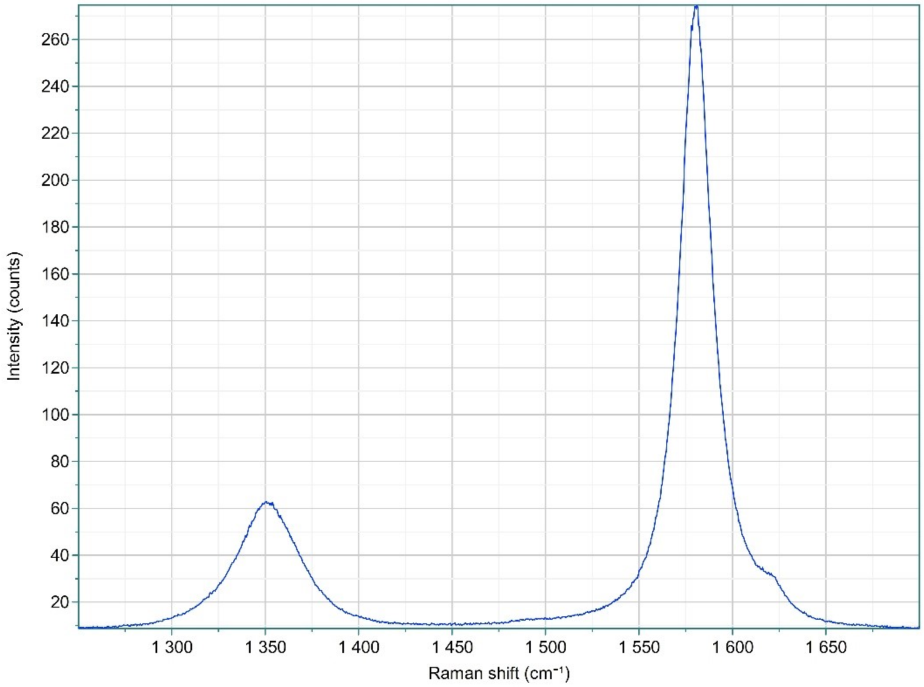

X412776-11

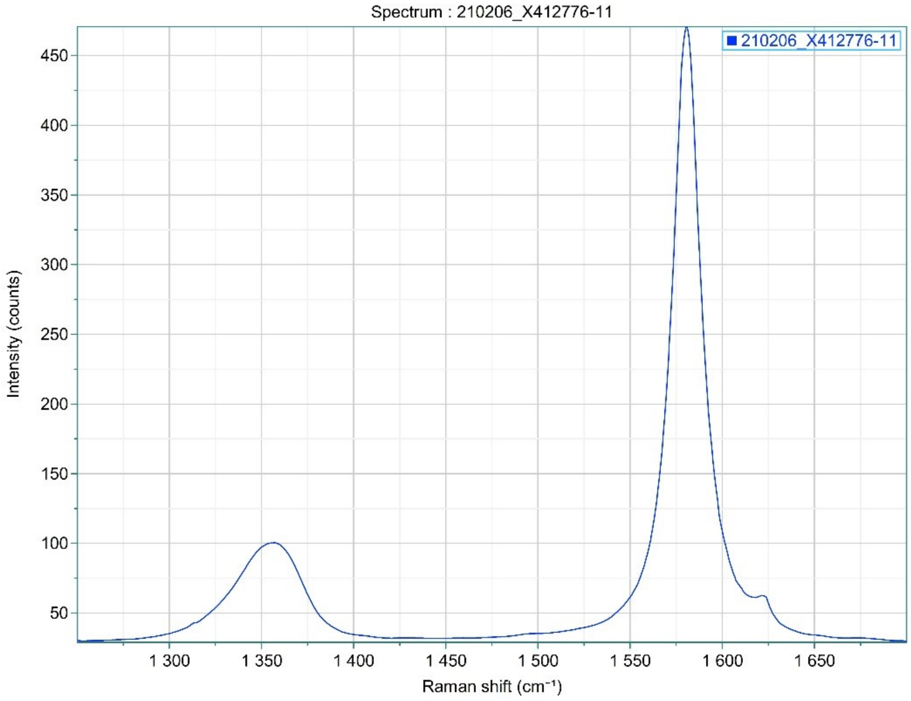

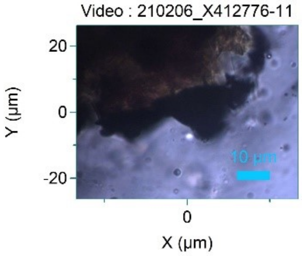

NOTES:

X412776-12

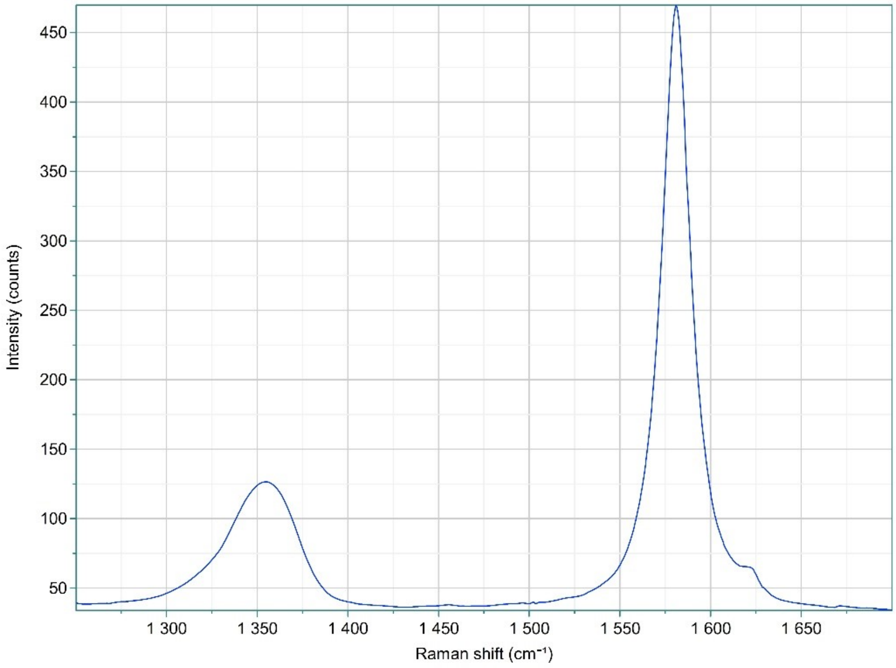

X412776-22

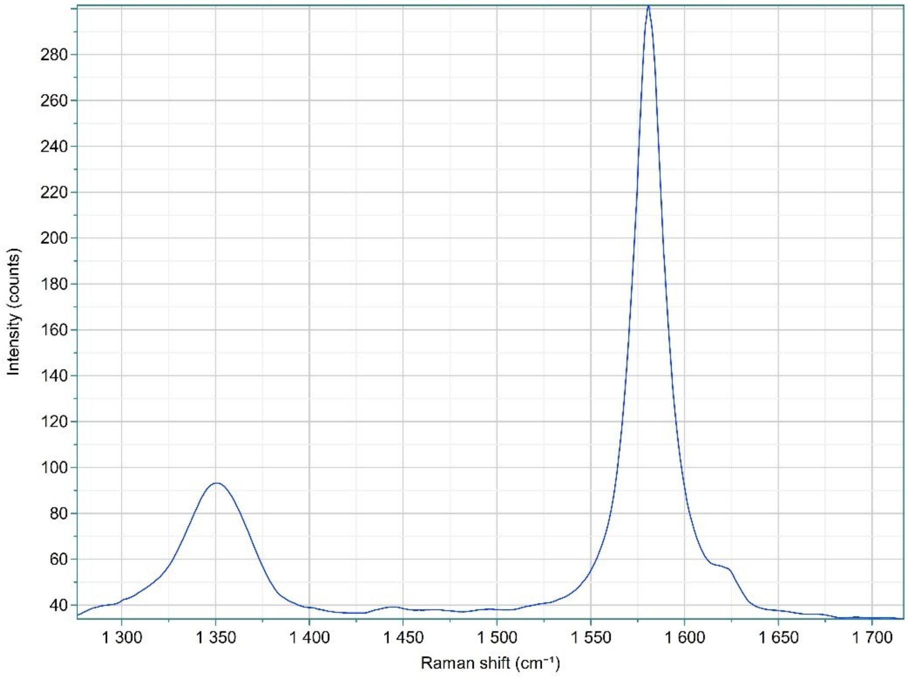

X412776-23

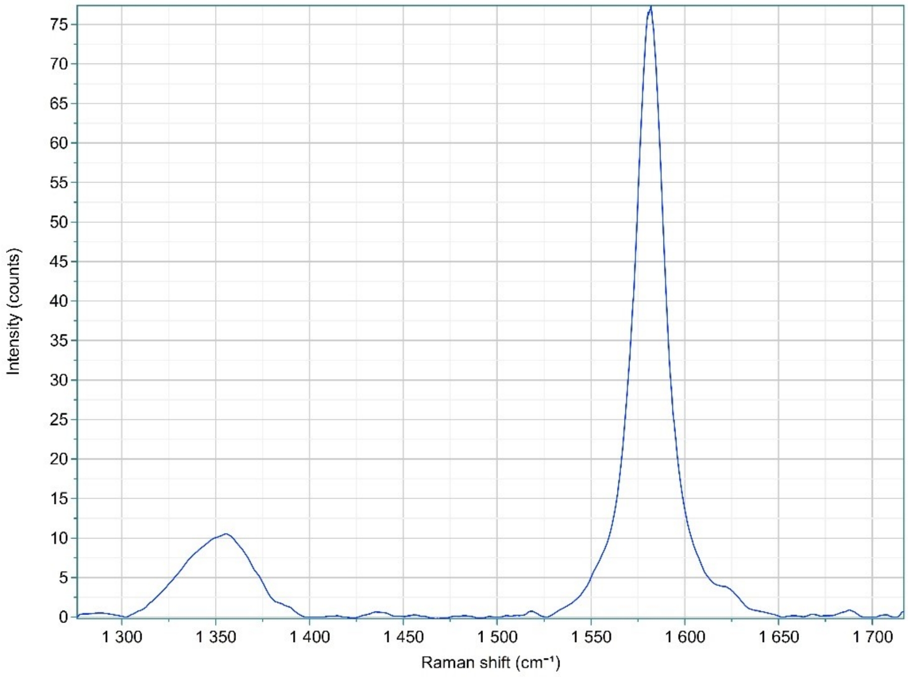

X412776-31

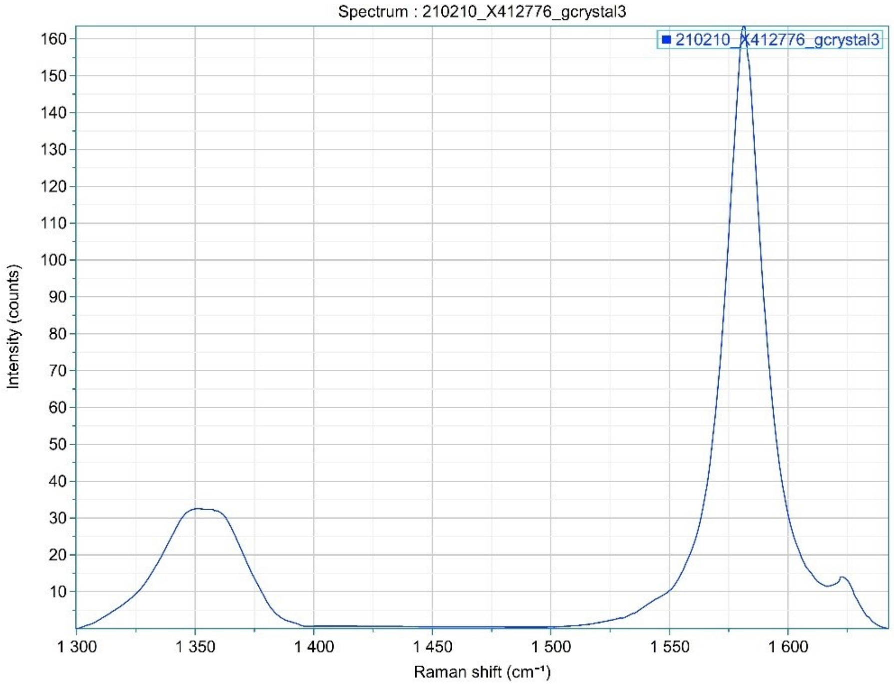

X412776-33

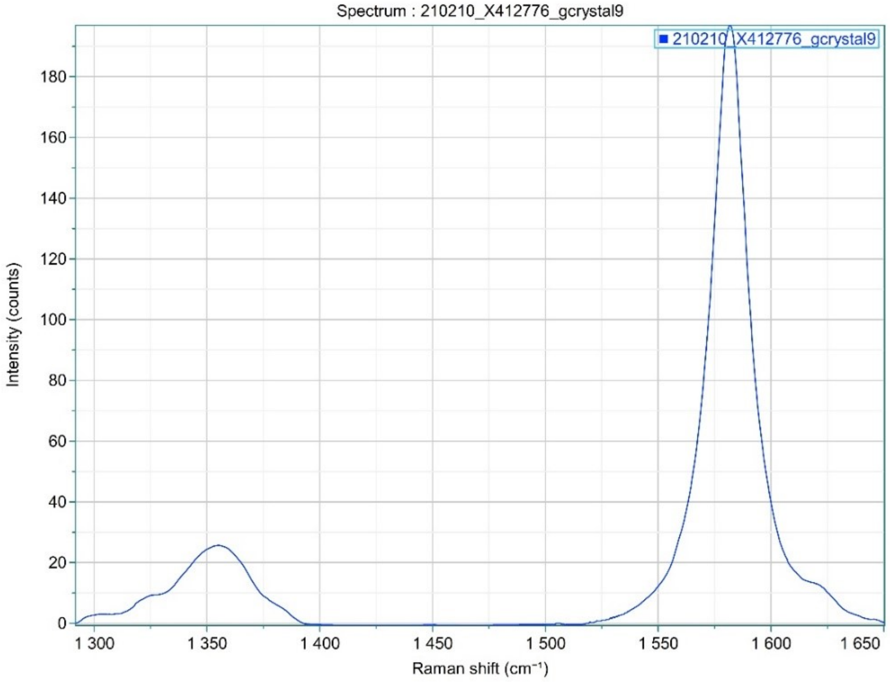

X412776-34

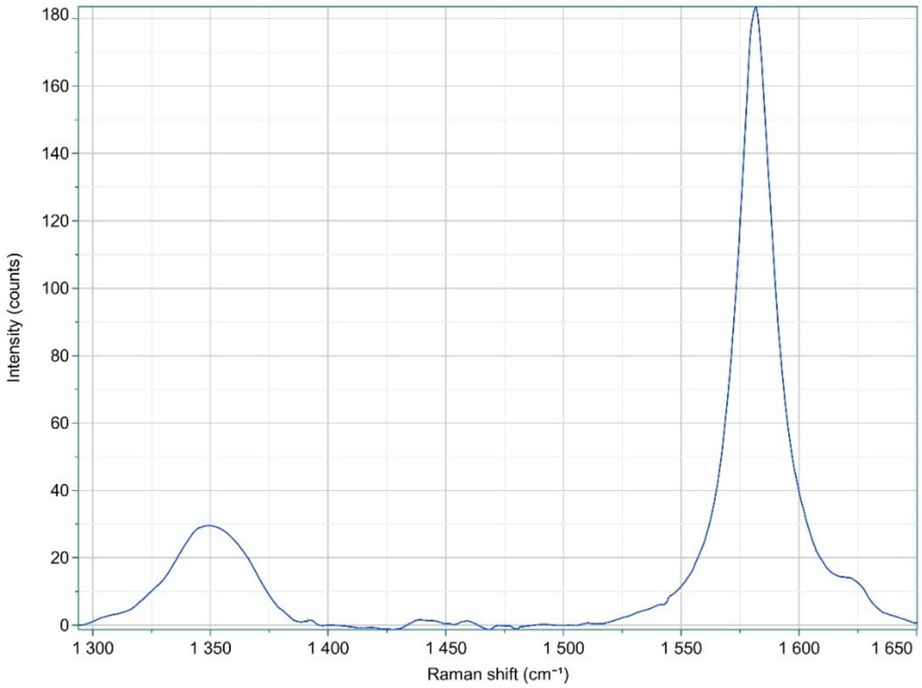

X412776-35

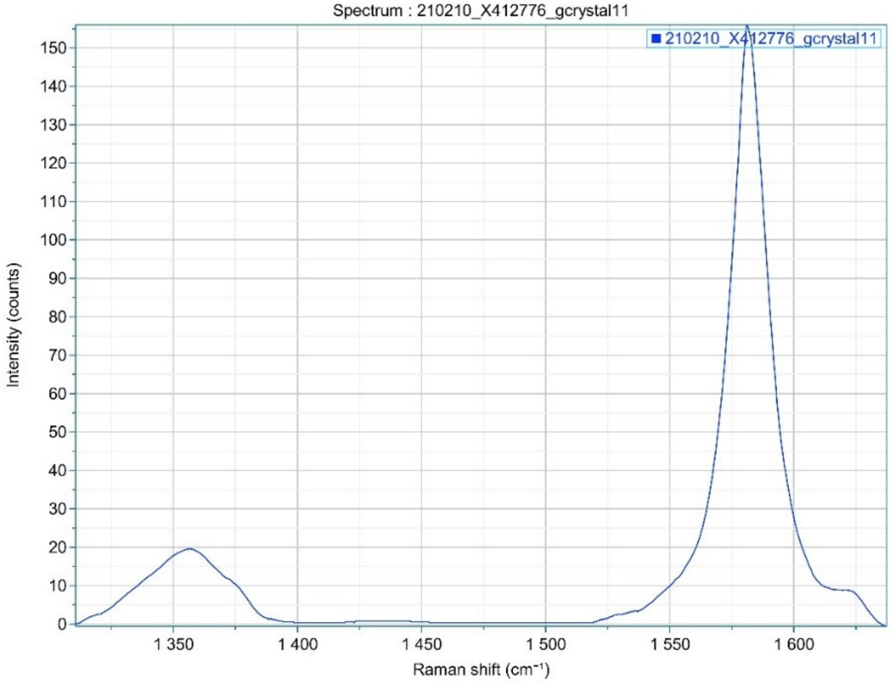

X412776-10

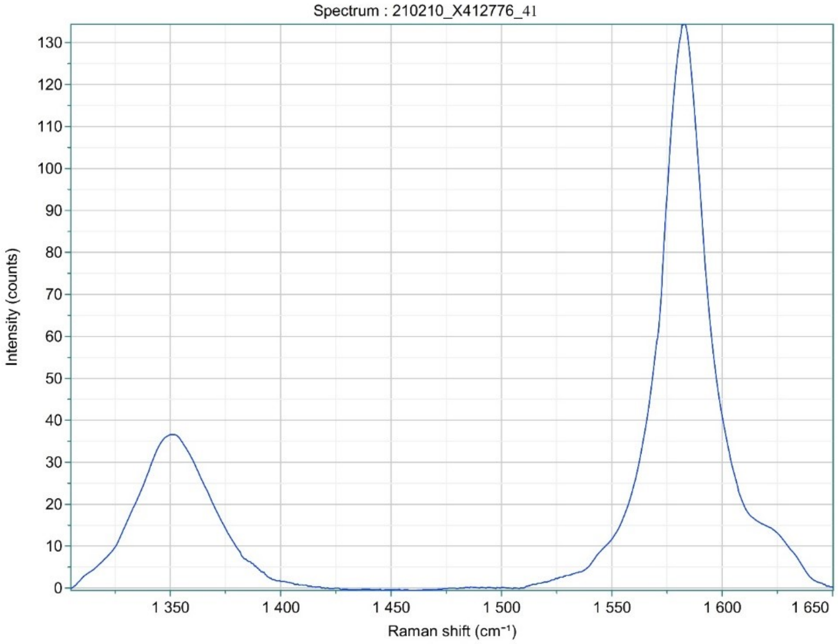

X412776-17

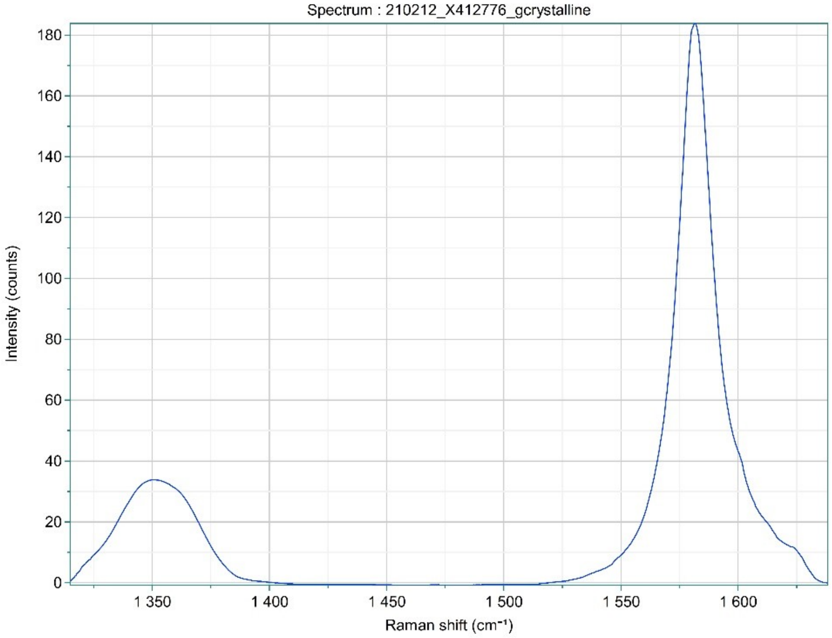

X412776-13

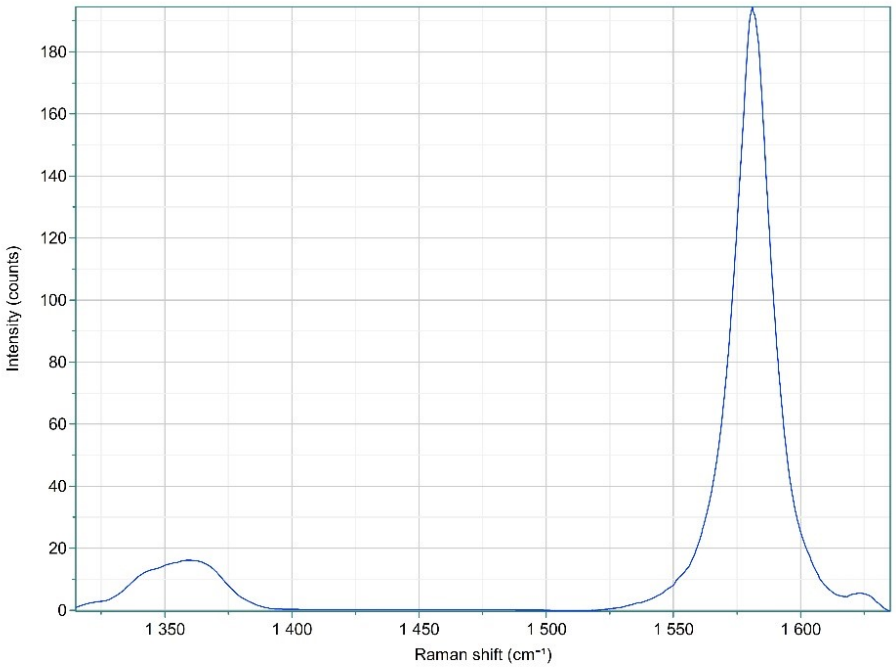

X412775-1

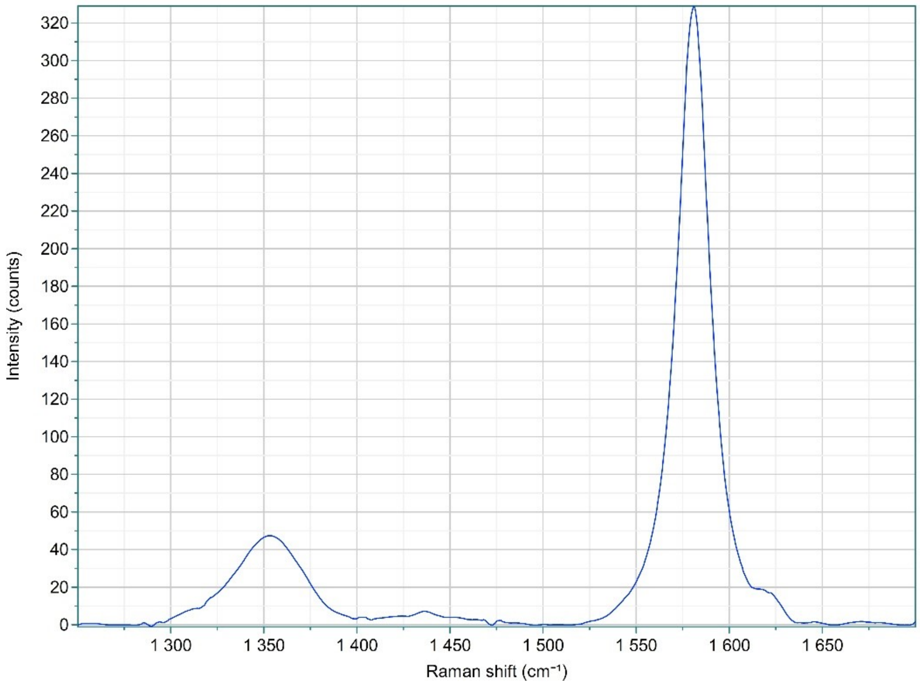

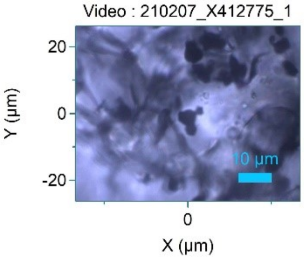

X412769-1

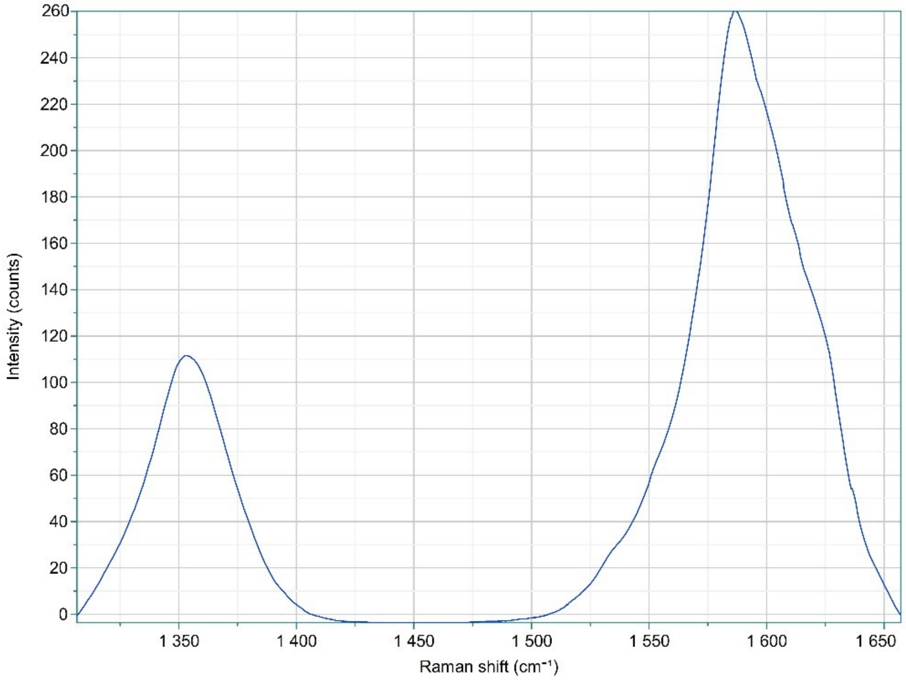

X412776-2

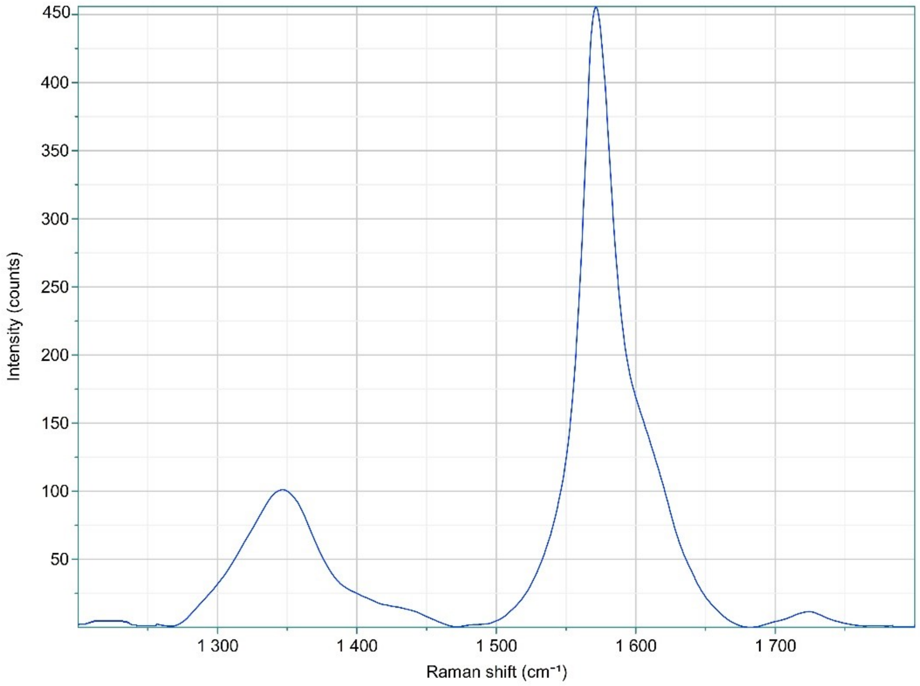

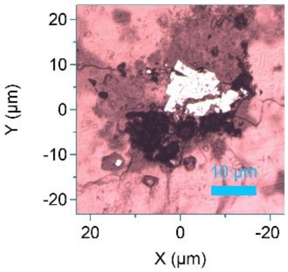

X412776-38

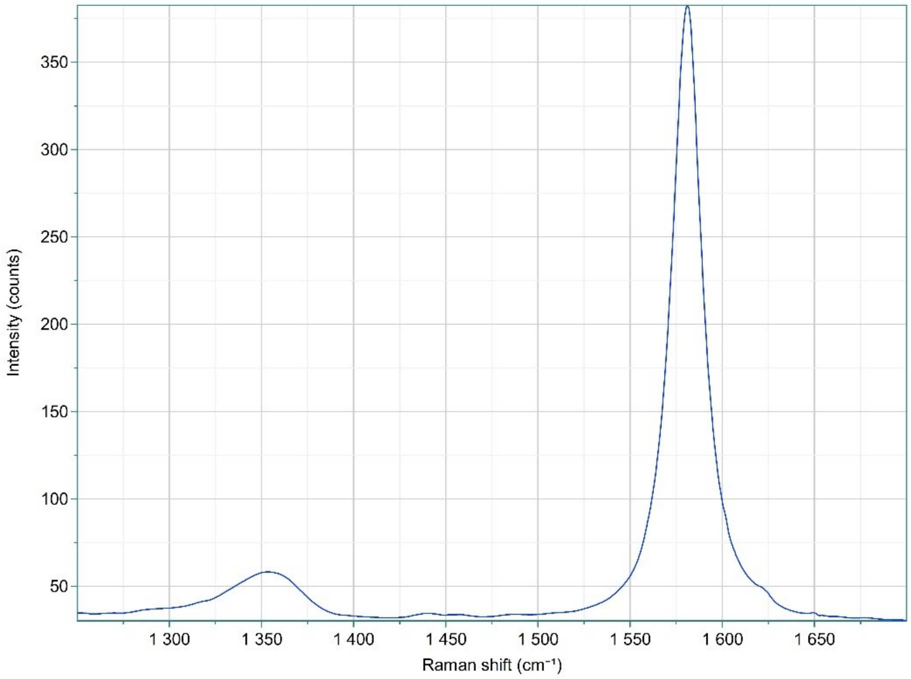

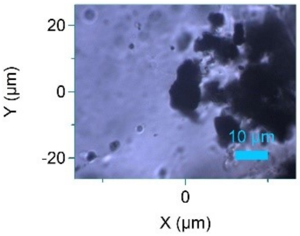

X412776-39

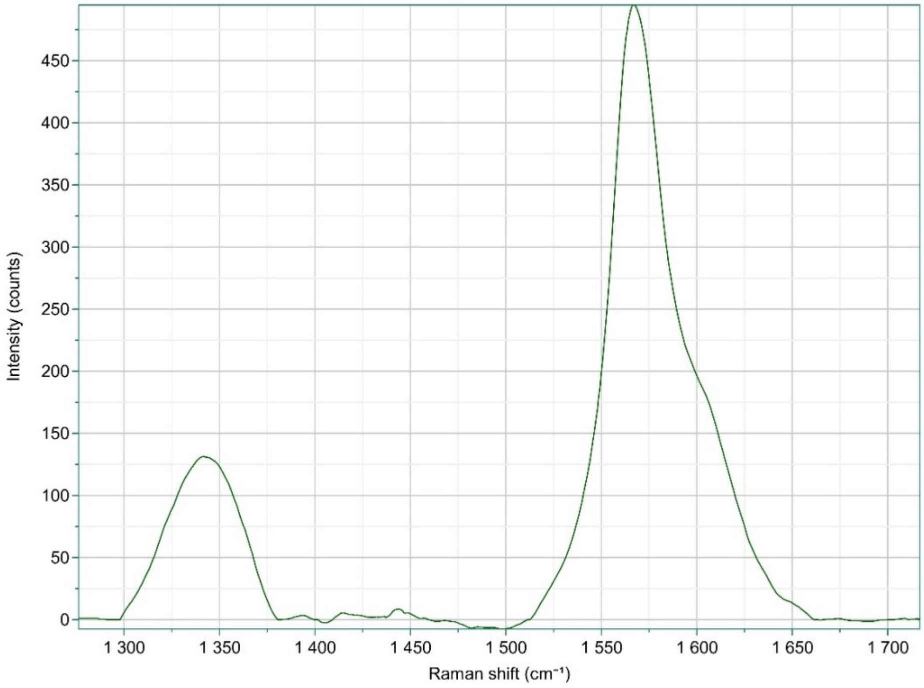

X412776-40

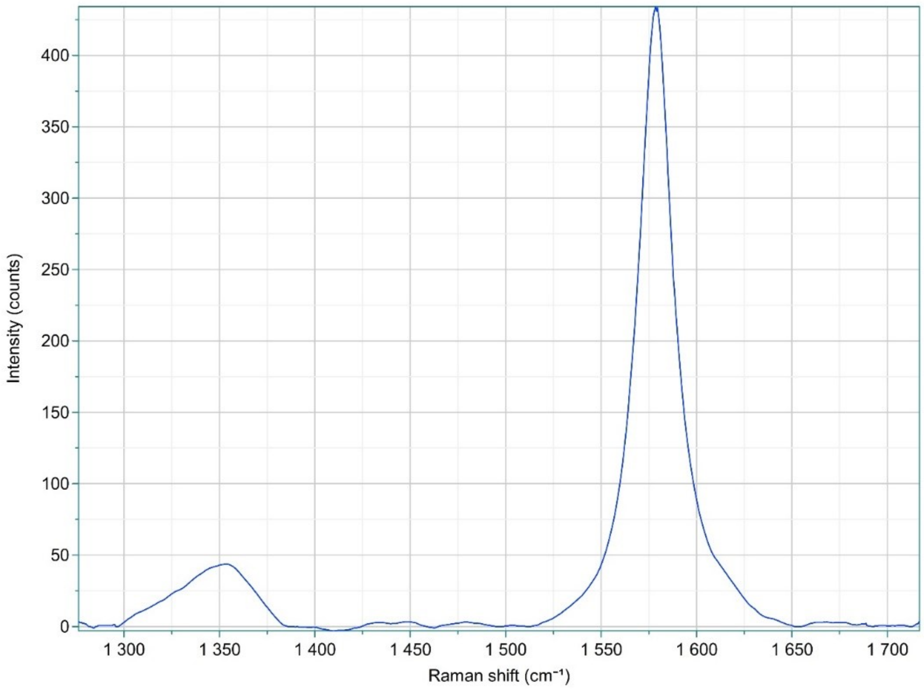

X412776-41

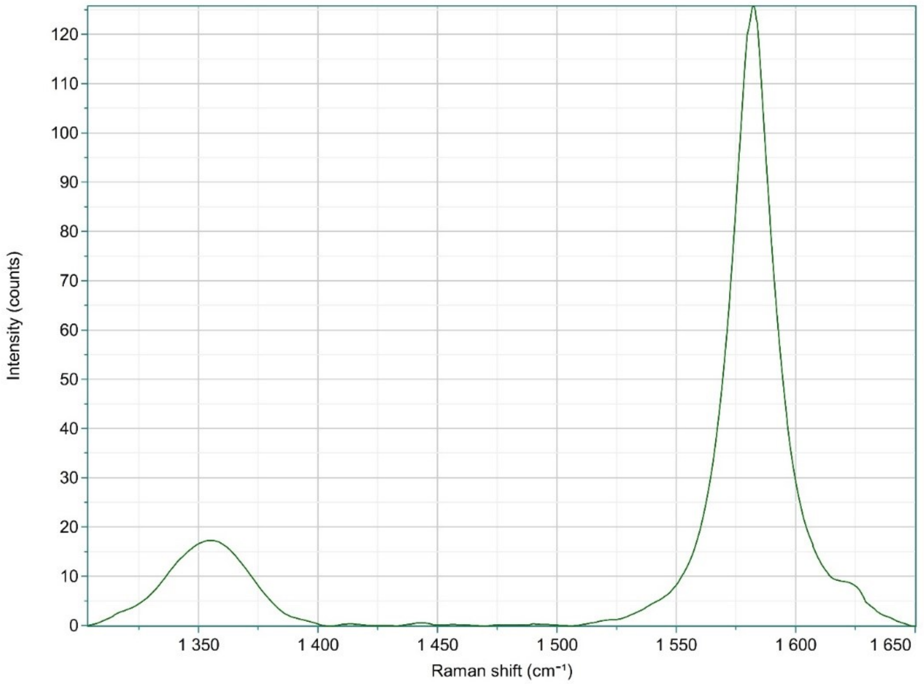

X412776-42

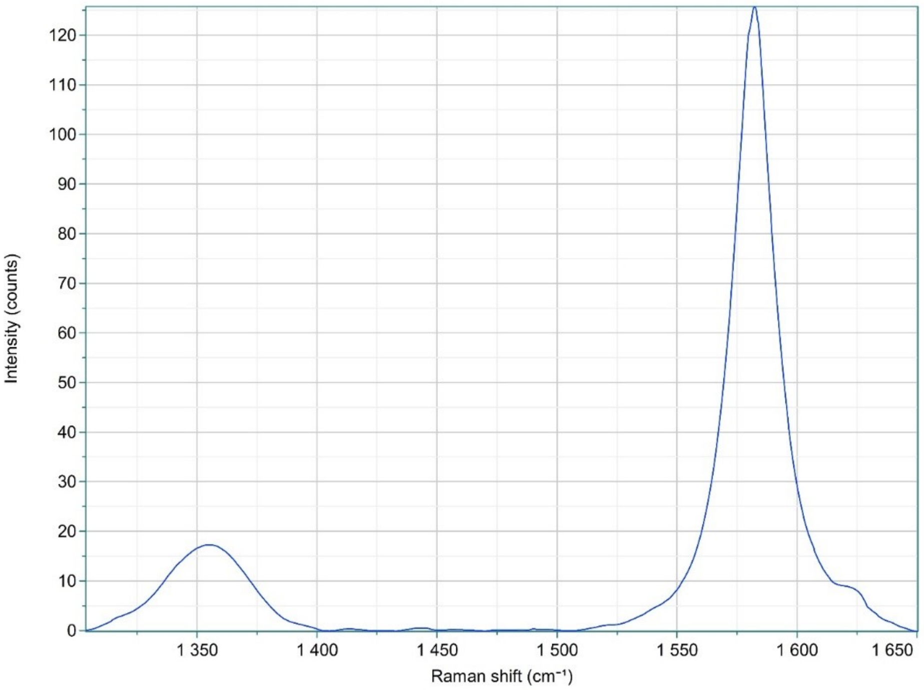

X412758-1

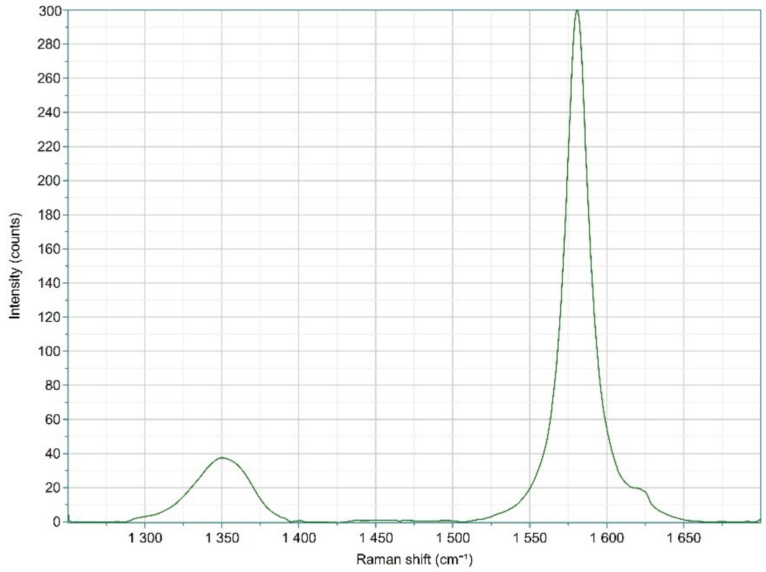

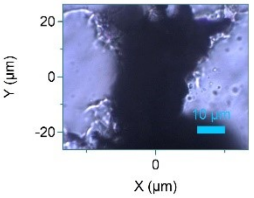

X412758-2

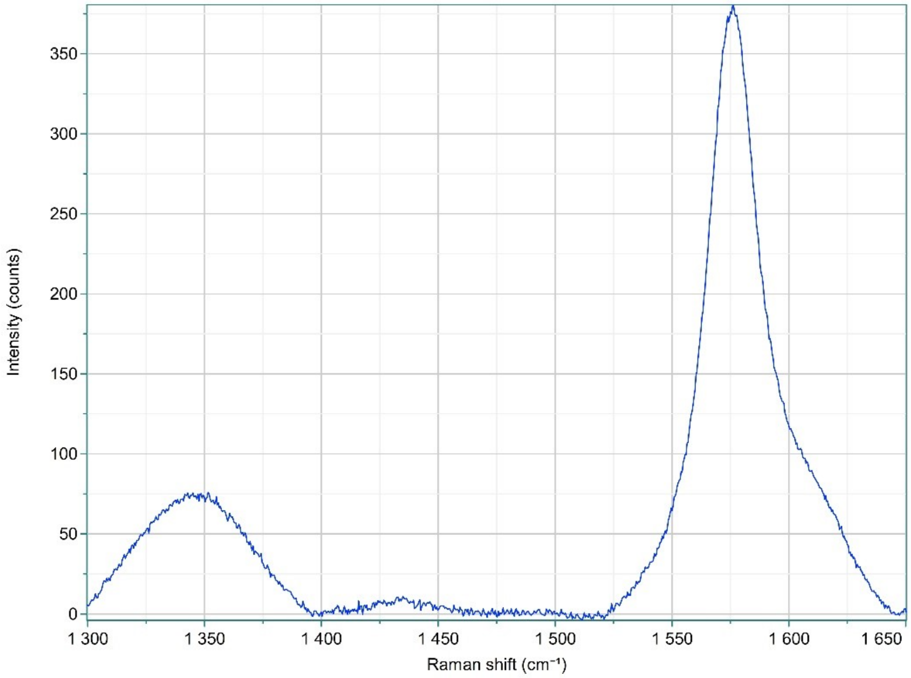

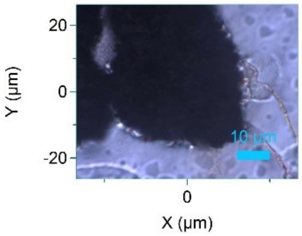

X412758-3

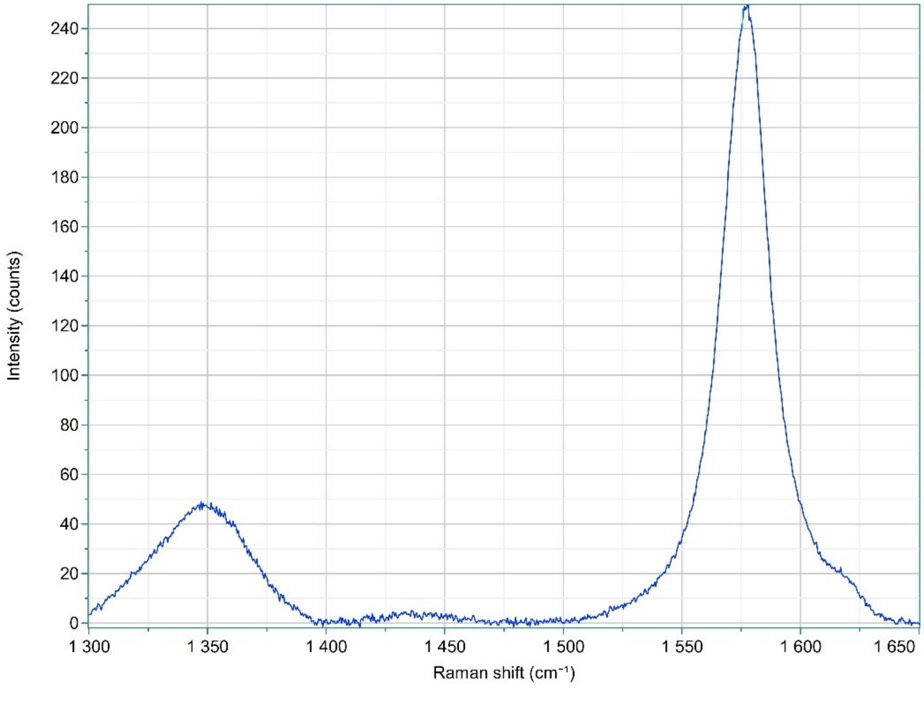

X412772-1

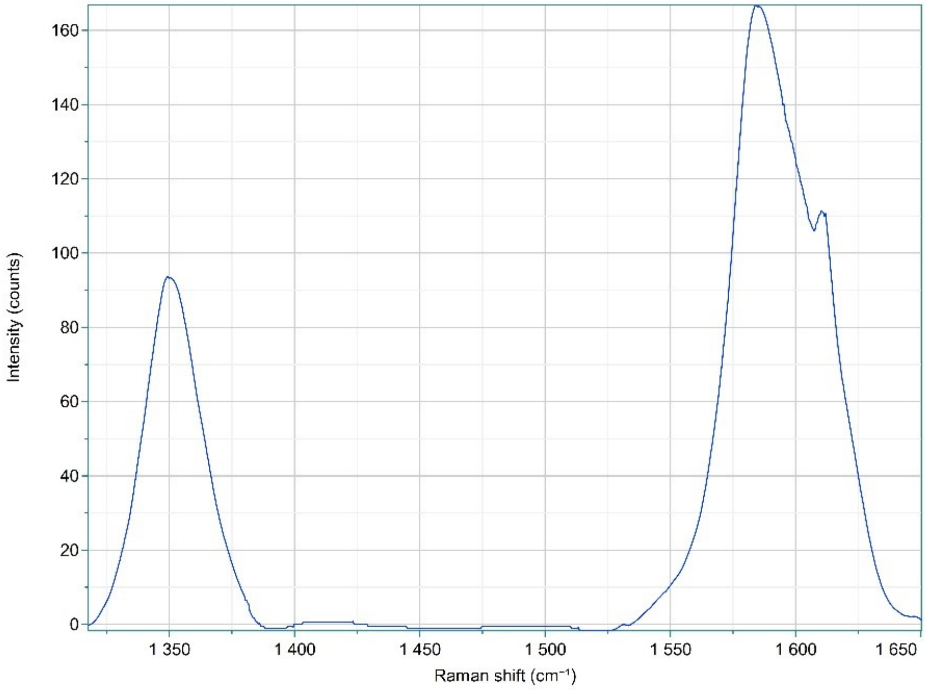

X412772-2